TERAHERTZ CONDUCTIVITY MEASUREMENTS ON CHROMIUM-VANADIUM ALLOYS AND PHOTOEXCITED INSULATING CUPRATES

by

Amir Darmanaki Farahani

B.Sc., University of Tehran, 2002

M.Sc., Institute for Advanced Studies in Basic Science (IASBS), 2005

A THESIS SUBMITTED IN PARTIAL FULFILLMENT
OF THE REQUIREMENTS FOR THE DEGREE OF
DOCTOR OF PHILOSOPHY
in the Department of
of
Physics

SIMON FRASER UNIVERSITY

Summer 2011

APPROVAL

Name: Amir Darmanaki Farahani

Degree: Doctor of Philosophy

Title of Thesis: Terahertz conductivity measurements on chromium-vanadium alloys and photoexcited insulating cuprates

Examining Committee:

Dr. Patricia Mooney, Simon Fraser University
Chair

Dr. J. Steven Dodge, Associate Professor, Physics,
Simon Fraser University; Senior Supervisor

Dr. David Broun, Associate Professor, Physics,
Simon Fraser University; Supervisor

Dr. Malcolm Kennett, Assistant Professor, Physics,
Simon Fraser University; Supervisor

Dr. Jeffrey McGuirk, Assistant Professor, Physics,
Simon Fraser University; Internal Examiner

Dr. Frank Hegmann, Professor, Physics,
University of Alberta; External Examiner

Date Approved: July 11, 2011

Partial Copyright Licence

Abstract

This thesis describes the application of terahertz (THz) spectroscopy to two physical systems, metallic $Cr_{1-x}V_x$ alloys and insulating cuprates. In the first system, we use time-domain THz spectroscopy (THz-TDS) to measure the low-frequency dynamical conductivity of $Cr_{1-x}V_x$ thin films. From the Drude model, we determine the plasma frequency of samples with x=0-0.08, as the system undergoes a quantum phase transition at $x \sim 0.035$ from a spin-density-wave state to a paramagnetic state. We compare these plasma frequency estimates to those inferred from the Hall resistance R_H on the same samples. We find that while both techniques reveal the opening of the spin-density-wave gap, quantitative differences appear at low temperatures that we attribute to anisotropic scattering.

In the second system, we use THz pulses to probe the conductivity of photoexcited carriers in insulating cuprates $Sr_2CuO_2Cl_2$, $YBa_2Cu_3O_6$, and La_2CuO_4. In all these compounds, photoconductivity appears promptly and decays non-exponentially in picoseconds. In the first few picoseconds after photoexcitation, the decay is characterized by fast dynamics that is weakly dependent on material, temperature, and concentration in the range of 0.2 to 1.5% holes per unit cell. Assuming a quantum efficiency of unity, the estimated peak mobility for all three compounds falls in the range 0.1-0.5 $cm^2/V \cdot s$. This is lower than the Hall mobility in chemically doped systems with similar carrier concentrations, but orders of magnitude larger than earlier static photoconductivity results, leading us to identify it as the intrinsic mobility of photoexcited carriers in insulating cuprates. At about 100 ps after photoexcitation, the conductivity develops a relatively strong temperature dependence that indicates hopping transport.

To my parents

"Research is what I'm doing when I don't know what I'm doing."

— Wernher Von Braun

Acknowledgments

There are many people who contributed to this work. In particular, I would like to express my gratitude to:

• **Steve Dodge** for supporting and giving me the opportunity to work in his lab. Besides his vast knowledge in physics, I admire his attitude toward science.

• **Jesse Petersen** for teaching me how to use the pump-probe spectrometer. I learned a lot from numerous discussions we had.

• **Saeid Kamal** for showing me how to use the THz-TDS system. He was the one who taught me the basic rules of working in the lab.

• **David Broun** for answering my myriad questions. This work would not have been accomplished without his help.

• **Malcolm Kennett** for helping me with the CrV project, especially the transport calculations in Appendix C.

• **Ruixing Liang** for providing single crystals of $Sr_2CuO_2Cl_2$ and $YBa_2Cu_3O_6$, **Eric Fullerton** for providing CrV thin film samples and performing Hall measurements, **Ivan Bozovic** for providing thin film samples of La_2CuO_4, and **Graeme Luke** for providing a single crystal of La_2CuO_4.

• **Payam Mousavi** and **Derek Sahota** for reading and editing this thesis.

• **Bill Woods** for helping me in the cleanroom while I was fabricating the THz antennas.

• **Payam Mousavi, Laleh Mohtashemi, Derek Sahota, Graham Lea, Jesse Petersen, Ian Bushfield, and Stéphane Savard** for all the interesting and often scientific conversations. You all made our office a friendly place.

And last but not least, I am grateful to have the love and support of Shima Alagha. It was fantastic to be with her in the final months of this degree.

Contents

List of Tables

List of Figures

Chapter 1

Introduction

The terahertz (THz) regime is loosely defined to span the frequencies between 100 GHz and 10 THz. In equivalent units,

$$1 \text{ THz} \Leftrightarrow 300\ \mu\text{m} \Leftrightarrow 33\ \text{cm}^{-1} \Leftrightarrow 4.2\ \text{meV} \Leftrightarrow 48\ \text{K}.$$

THz frequencies occupy a gap between conventional microwave and infrared spectroscopies, and cannot be accessed effectively by standard techniques from either neighbouring frequency range.

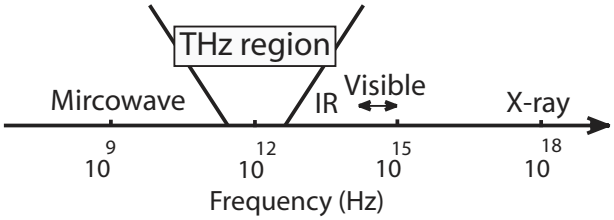

Figure 1.1: THz region in the electromagnetic spectrum.

Advances in femtosecond mode-locked lasers in the 1980s were a major breakthrough in the field. The next decade was followed by the development of various THz sources, including photoconductive switches [1] and electro-optic crystals [2], that have led to higher THz radiation intensity and detection sensitivity. Unlike conventional optical spectroscopy, THz spectroscopy detects the coherent field of THz radiation with sub-picosecond resolution.

In THz time-domain spectroscopy (THz-TDS), ultrafast optical pulses are used to generate THz radiation either by inducing photocurrents in a photoconductive antenna or via optical rectification in a nonlinear crystal. When combined with appropriate detectors, e.g., another photoconductive antenna or an electro-optic material, these sources can be utilized for THz time-domain spectroscopy.

1.1 THz time-domain spectroscopy of $Cr_{1-x}V_x$ alloys

THz-TDS is capable of studying the material properties in a part of the electromagnetic spectrum that is of particular interest in material science. Interestingly, scattering rates of many metals, doped semiconductors [3], and high temperature superconductors [4] fall in the THz region. The technique is also capable of measuring the complex electromagnetic field amplitude, enabling simultaneous extraction of the real and imaginary parts of the conductivity without requiring Kramers-Kronig transformations. Using THz-TDS, we can simultaneously estimate the DC conductivity and scattering life time in metals. From their product, we determine the plasma frequency, a fundamental ground-state property of the Fermi surface. We applied this idea for studying the complex conductivity in $Cr_{1-x}V_x$ over concentrations with x=0-0.08. We probed the changes in the plasma frequency as the system undergoes a quantum phase transition from a spin wave density (SDW) state to a paramagnetic state at $x \sim 0.035$.

1.2 Visible-pump, THz-probe spectroscopy of insulating cuprates

The time resolution of THz-TDS makes it ideal for visible-pump, THz-probe spectroscopy. The basic idea is to optically create photocarriers in a sample and probe the non-equilibrium state using THz pulses. In our visible-pump, THz-probe spectrometer, the THz generation is based on optical rectification and detection is based on free-space electro-optic sampling. A regenerative amplifier is employed to amplify ultrafast optical pulses to provide a high density of photoexcitations in samples. The technique is a natural choice for investigating the decay dynamics and underlying processes in insulating and semi-insulating materials. In this thesis, we applied the technique to study the time evolution of photoconductivity in the insulating cuprates $Sr_2CuO_2Cl_2$, $YBa_2Cu_3O_6$, and La_2CuO_4. At early times after photoexcitation, we find that the mobility of the photocarriers is limited by non-equilibrium bosons, presumably consisting of both phonons and spin fluctuations. Approximately 100 ps after photoexcitation, these bosons have decayed, resulting in a reduction in mobility that suggests polaronic hopping transport.

1.3 Structure of the thesis

This thesis is organized as follows. Chapter 2 is devoted to instrumentation and methods in time-domain THz spectroscopy. I begin by explaining THz generation and detection using dipole antennas. After a brief discussion of how the photoconductive antennas are fabricated at the SFU clean room facility, I discuss the process for measuring the conductivity of a thin metal film on a substrate and the models we use for analyzing the transmission amplitude data.

Chapter 3 is devoted to the study of itinerant carriers in $Cr_{1-x}V_x$ thin films. We determine the evolution of the plasma frequency as the system undergoes a quantum phase transition from a spin-density-wave state to a paramagnetic state. We compare these to the plasma frequency inferred from Hall measurements on the same samples. The project was started by Saeid Kamal, a former member of our group, who performed the initial measurements on the first batch of samples. Eric Fullerton's group at the University of California at San Diego made the samples and performed the Hall measurements. I completed the initial THz-TDS measurements and performed new measurements on a second batch of samples, after identifying and reducing the limiting systematic uncertainties of the measurement.

In Chapter 4, the theoretical and experimental principles of the visible-pump, THz-probe technique are highlighted. I explain THz generation and detection using optical rectification and electro-optic sampling in nonlinear crystals. I discuss the layout of the apparatus and measurement process, then demonstrate its application with a GaAs sample.

In Chapter 5, we report the transient photoconductivity of insulating cuprates as a function of time, frequency, and temperature in the initial state after photoexcitation. The picosecond resolution of the visible-pump, THz probe technique allows us to study the intrinsic properties of the photoinduced carriers. This project was initiated by Jesse Petersen, a former member of our group, who performed the initial measurements on $Sr_2CuO_2Cl_2$. After performing a full optimization of the spectrometer and laser system, I improved the data quality and extended the work to $YBa_2Cu_3O_6$ and La_2CuO_4.

In Chapter 6, I outline the future directions and possible ways to improve the quality of measurements.

Chapter 2

THz time-domain spectroscopy

The work in this thesis relies on two distinct THz spectrometers that employ common principles of operation with somewhat different technology. This chapter provides an overview of the general principles of THz time-domain spectroscopy (THz-TDS) and a description of the THz spectrometer, based on photoconductive antenna technology, that we used to characterize $Cr_{1-x}V_x$ alloys. I begin with an explanation of THz generation and detection using dipole antennas, and describe how we implement this technology in our laboratory THz spectrometer. I then discuss the measurement procedure and the models we use for data analysis. The basic principles described here are also used in a separate visible-pump, THz-probe spectrometer but with a different technical implementation that I describe in Ch. 4.

2.1 THz generation using a photoconductive antenna

Fig. 2.1(a) is a schematic of a typical photoconductive antenna used in our laboratory. The central element is a simple metallic dipole antenna that is coupled to a voltage bias through a parallel-wire transmission line and interrupted by a gap of a few microns at the center. The gap is filled by a photoconductive material that serves as a picosecond switch when illuminated by a femtosecond laser pulse. The bias field accelerates photocarriers to produce a transient photocurrent $J(t)$. A typical transient current and its time derivative are illustrated in Fig. 2.1(b). In the far-field approximation, the emitted THz pulse is given by [5]

$$E = \frac{\mu_0}{4\pi r^3}(\ddot{\mathbf{P}} \times \mathbf{r}) \times \mathbf{r}, \tag{2.1}$$

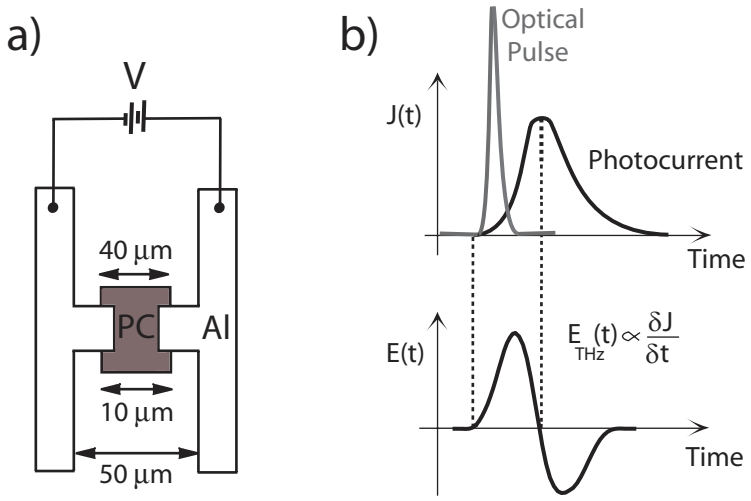

Figure 2.1: a) Schematic structure of a dipole antenna. It consists of two parallel-wire transmission lines that is interrupted by a gap of a few microns at the center. A photoconductive (PC) material bridges the gap when illuminated with ultrashort optical pulses. b) An electrical bias field accelerates the photocarriers resulting in a transient photocurrent $J(t)$. The far-field radiated field is proportional to the time derivative of the photocurrent.

where $\ddot{\mathbf{P}}$ is the second time derivative of the radiating dipole moment, $\mathbf{r}$ is the position vector measured from the dipole with magnitude r, and μ_0 is the permeability of free space. This approximation is valid when the emitted wavelength is much longer than the dipole length, which is 50 μm in our antenna design. Note that $\ddot{\mathbf{P}}$ is proportional to the time derivative of the photocurrent.

There are three time constants involved in the process of THz generation using photoconductive antennas [6]. First, the laser pulse width sets a lower bound on the photocurrent rise time. In our system, the laser pulse width (FWHM) is 30 fs, which in turn sets an upper limit of 33 THz on the emitted radiation, well above our measured bandwidth. The second and most significant time constant is the photocurrent decay time. To extend the bandwidth of the emitted field into the THz region, the recombination time can be minimized by introducing defects that act as traps. This is achieved either during the crystal growth, as with low-temperature grown GaAs, or via ion implantation after the growth, as with oxygen irradiated silicon. In radiation-damaged silicon-on-sapphire (SOS), the recombination time can be reduced to about 600 ps [7]. The third relevant time constant is the carrier collision time that determines the mobility and consequently limits the photocurrent rise time. Using the visible-pump, THz probe technique, Lui and Hegmann reported a mobility of 422 $\mathrm{cm}^2/\mathrm{V}\cdot\mathrm{s}$ in radiation-damaged SOS [8]. This results in a collision time of 48 fs using an effective mass of $m^* = 0.2m_0$. For 800 nm Ti:sapphire excitation pulses, radiation-damaged Si and GaAs

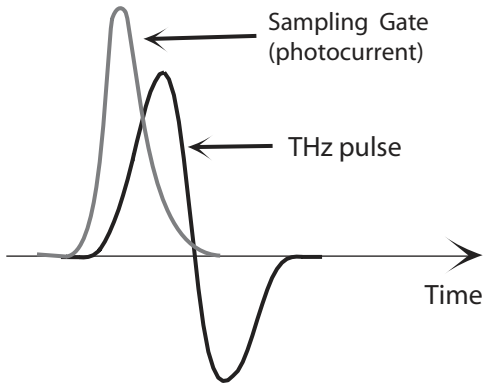

Figure 2.2: Schematic of the gated detection method. The photoconductive antenna measures a convolution of the incident field with the impulse response of the receiver antenna. The THz waveform is mapped by varying the time delay between the optical pulse and THz waveform.

are widely used as photoconductive materials. These materials have high carrier mobility, an energy gap below the excitation energy, and high dark resistivity.

2.2 THz detection using a photoconductive antenna

In our spectrometer, we use a photoconductive antenna to detect THz pulses. For coherent detection, a second laser pulse is required to be synchronized with the generation laser pulse. We use a beam splitter and an independent time delay to create what I call detection and generation pulses. The detection pulse generates photocarriers across the gap in the detector antenna and the THz pulse acts as a bias field to drive the photocurrent. When the detection pulse is incident, the detector is active and measures the voltage associated with the THz amplitude within the duration of the photocurrent. In our system, the receiver antenna is conducting for about 600 fs with a repetition rate of 100 MHz. Thus, the detector is open for 600 fs and closed for the following 10 ns. By varying the time-delay between the THz and detection gating pulses, the entire THz trace is mapped as a function of time in a process known as gated detection. The detection scheme is demonstrated in Fig. 2.2.

This detection scheme has two main advantages. First, it yields a high SNR because it minimizes the blackbody background noise. Secondly, it provides a measurement of the THz electric field as a function of time. In the frequency domain, this enables the simultaneous measurement of the full complex electromagnetic response of a sample.

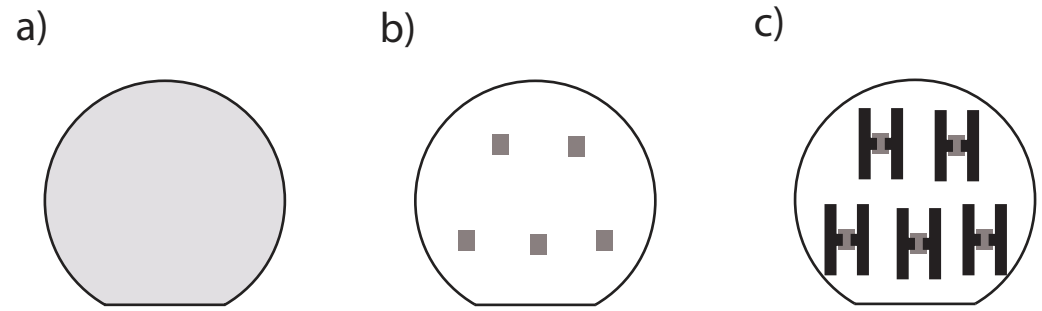

Figure 2.3: An illustration of the antenna fabrication process: a) An SOS wafer with a barrier layer of SiO_2. b) The remaining arrays of silicon rectangles on the sapphire wafer. c) The etched aluminum pattern on the wafer.

2.3 Antenna fabrication

We chose to work with silicon-on-sapphire (SOS) wafers because of the availability of wafers and the capabilities of our fabrication facility. The SOS wafer is a 0.53-mm sapphire substrate with a 0.3 μm silicon layer with a resistivity greater than 100 Ω-m. A schematic of the fabrication process is illustrated in Fig. 2.3. We begin by growing a barrier layer of SiO_2 on the SOS wafer. This step is necessary to protect the silicon layer from the tetramethylammoniumhydroxide (TMAH) etchant. A 20-minute dry oxidation at 900°C produces a 10 nm layer of SiO_2. This is followed by patterning the oxide layer using an ordinary photolithographic procedure. Immersing the wafer in 25% TMAH yields arrays of 40 μm$\times$60 μm silicon rectangles on the wafer. It is essential to perform an RCA cleaning [1] procedure prior to aluminum deposition to remove organic contaminants and ensure good contact between the silicon and aluminum layers. An electron beam evaporator is used to deposit a 1 μm aluminum layer. This deposition is then followed by a second photolithographic procedure, to define a pattern that is etched into the aluminum at 50°C with transene aluminum etchant. Finally, the wafer is annealed at 475°C for 30 minutes to improve the contact between the aluminum and silicon. The wafer is then sent for oxygen ion implantation at CORE Systems.[2] To ensure uniformity, the ion implantation is performed in two steps: one at 100 keV and the other at 200 keV, both with an areal density of 10^{15} cm^2. This process reduces the carrier lifetime to $\sim$0.6 ps [7].

[1] RCA cleaning is a standard procedure for removing organic and ionic contaminants. This procedure also strips the natural oxide layer. Werner Kern developed the basic procedure in 1965 while working for RCA, the Radio Corporation of America.

[2] http://www.coresystems.com

2.4 Spectrometer layout

The optical layout of the THZ-TDS setup is shown in Fig. 2.4. The spectrometer is driven by ultrashort optical pulses from a mode-locked Ti:sapphire oscillator. The laser provides pulses of 30 fs duration, centered at 800 nm with a 100 MHz repetition rate and an average power of 550 mW. We are limited to using 50% of the total power, as the other half is used to seed a regenerative amplifier. A 50-50 beam-splitter (BS) divides the remaining beam into two arms: one is used to generate THz pulses and the other to detect them. Both laser beams are tightly focused onto the antenna gaps by microscope objectives (MO). When the laser pulse strikes a biased emitter antenna, photocarriers are induced and a THz pulse is generated. To allow lock-in detection, we apply a sinusoidal bias voltage of 45 V with a modulation frequency of 5 KHz to the emitter antenna. By modulating the bias voltage and using a lock-in amplifier on the detection side, we reduce the $1/f$ noise contribution. A pair of 90° parabolic mirrors (Janos Tech, 4" diameter) collimate and focus the THz beam onto a sample mounted on a sample holder in a continuous flow liquid helium cryostat (Janis Research Company). Up to three samples can be mounted on the sample holder which has three fixed apertures. The samples are positioned in the path of the focused THz pulses by vertical adjustments of the sample stick. Heaters and thermometers are mounted on the sample holder to control and measure the sample temperature over a range of 5-300 K. After traveling through the cryostat, the THz pulses are collimated and focused on a gated detector antenna by a second pair of 90° parabolic mirrors. By varying the path length of the emitter arm with a delay stage (Newport, ESP-25cc controlled by an XPS motion controller), the THz pulses are mapped in the time domain. The THz detector is followed by two amplification stages: an ultra-low noise transimpedance amplifier (Femto, DLPCA-200) with a gain of 5×10^7 V/A, and a lock-in amplifier (Signal Recovery, 7265) that is phase-locked to the bias of the emitter antenna. We typically set the lock-in time constant (integration time) to 100 ms with a waiting time of 500 ms between each measurement. The transimpedance amplifier is located in close proximity to the antenna to minimize the effects of cable capacitance and electrical pickup.

A high-resistivity hyperhemispherical silicon lens with a radius of 5 mm is mounted against the sapphire substrate of each antenna. These lenses provide efficient coupling between the THz pulses and free space while improving collimation of the generated THz pulses. For the sapphire antenna substrates, silicon lenses are ideal because of the low absorption and frequency-independent refractive index (n$\sim$3.42) in the THz region [9]. A pair of linear polarizers (lithographically patterned on mylar) is placed in the collimated THz paths to ensure the vertical polarization of THz pulses. The polarizers are crucial for studying birefringent samples. The THz optics are placed in an enclosure

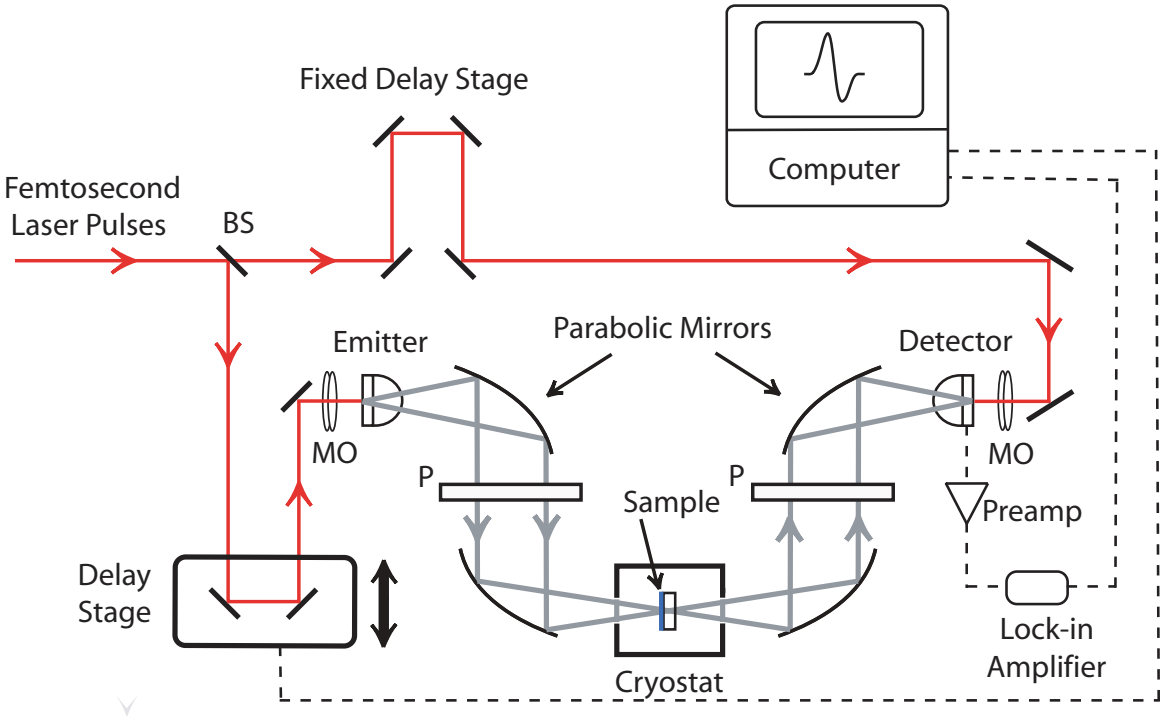

Figure 2.4: Optical layout of the THz-TDS setup. An ultrafast laser beam is split into two arms at the beamsplitter (BS). One arm goes to a motorized delay line before illuminating the emitter antenna, and the other beam goes to a fixed delay before illuminating the detector antenna. Two microscope objectives (MO) are employed to focus the laser spot onto the antenna gaps. Emitted THz radiation is collected, collimated, transmitted through a sample, and focused onto a gated detector antenna by the set of four parabolic mirrors. A pair of linear polarizers (P) are mounted in the collimated THz paths to ensure that the polarization state remains vertical, along the antenna orientation. THz pulses are mapped by varying the path length to the emitter. The detector photocurrent is sent through a low-noise current preamplifier before it is measured by a lock-in amplifier.

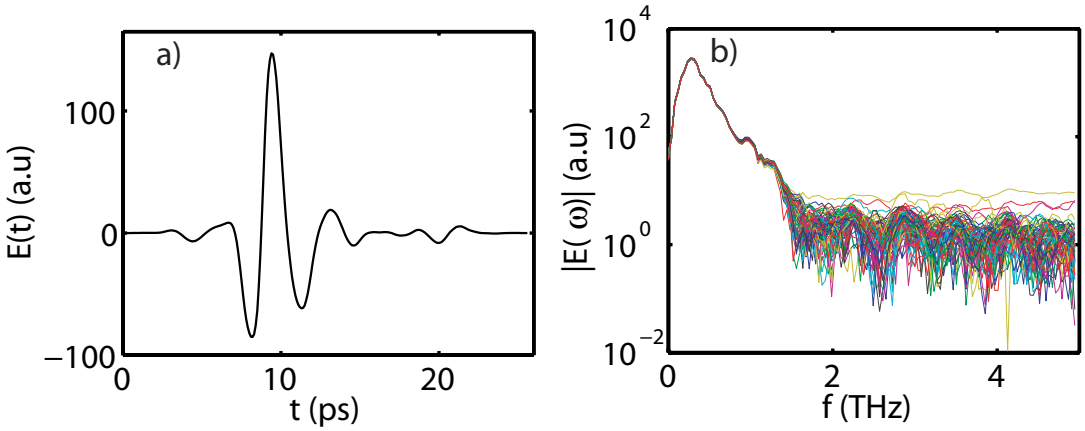

Figure 2.5: a) A typical time-domain THz pulse through nitrogen-flushed air b) Spectra of 100 pulses measured consecutively.

to reduce air fluctuations that can produce variations in THz path length. The enclosure is purged with dry nitrogen to eliminate water rotational-vibrational absorption lines [10].

2.5 THz pulses

We sample THz pulses by varying the delay between the THz and optical pulses using a computer-controlled delay stage. The mechanical precision of the stage is ~ 0.1 μm, which corresponds to a time jitter of 0.67 fs. However, the actual time resolution is limited by the thermal drift in the overall optical alignment and is expected to be up to a few femtoseconds. This point is discussed in detail in section 2.8. In our experiment, we typically sample the THz waveform with 256 points spaced by 0.1 ps. A typical THz time-trace in a nitrogen purged environment is shown in Fig. 2.5(a).

After subtracting the DC value and applying the tapered cosine window (Tukey function in Matlab with taper ratio $r = 0.5$), we use a discrete Fourier transform (dFT) to determine the complex field amplitudes in frequency domain. Fig. 2.5(b) shows the Fourier transform of 100 scans measured sequentially. The sampling time of 0.1 ps corresponds to a Nyquist frequency of 5 THz, well beyond the measurement bandwidth of 0.1-1 THz. The frequency range of 3.1-5 THz is used to determine the noise floor. The ratio of the maximum amplitude at 0.5 THz and the averaged noise floor gives an SNR of about 1000. This is considerably smaller than the SNR obtained from the

time-domain THz pulse by comparing the peak amplitude to the noise over the region where the signal is close to zero. This shows that the noise in our system is not simply additive white noise. We set the lock-in time constant to 100 ms as there is a trade-off between the noise reduction and the thermal drift in the optical alignment. The longer integration time corresponds to a narrower noise bandwidth and results in higher SNR. The waiting time is chosen to be several times longer than the integration time to avoid smoothing the signal waveform that would filter out higher frequencies of its spectrum.

A careful determination of the THz beam waist is crucial for spectroscopy of smaller samples ($< 10 \times 10$ mm^2). This measurement is performed by inserting a variable diameter iris at the THz focal point and taking a series of scans at different iris diameters. The details of the measurement process are described in Carl-Philippe Kübler's thesis [11], and I only quote the current results. The beam waist radius is 4.4 mm at 133 GHz and 2.6 mm at 187 GHz. These values are both within a factor of two of the diffraction limited radii of 2.55 mm at 133 GHz and 1.8 mm at 187 GHz for a numerical aperture of 0.28 for the system [12].

2.6 Measurement process

To determine the transfer function of an unknown sample, we require two separate measurements: a reference pulse $E_1(t)$ and a sample pulse $E_2(t)$. In all of the measurements described in this thesis, the reference pulse corresponds to a pulse transmitted through an insulating substrate and the sample pulse refers to a pulse transmitted through a thin conducting film on a matched insulating substrate. For spectral analysis, a discrete Fourier transform yields the complex transmission amplitudes, $\tilde{E}_1(\omega)$ and $\tilde{E}_2(\omega)$. Their ratio in the frequency domain is the complex transmittance $\tilde{T}_{2,1}(\omega) = \tilde{E}_2(\omega)/\tilde{E}_1(\omega)$, which is directly related to the conductivity of the thin film via the Tinkham formula [13]:

$$\tilde{\sigma}(\omega) = \frac{n_s + 1}{Z_0 d_f}\left[\frac{1}{\tilde{T}_{2,1}(\omega)} - 1\right]. \tag{2.2}$$

Here, n_s is the refractive index of the substrate in the THz region, Z_0 is the impedance of free space, and d_f is the film thickness. A detailed derivation of the Tinkham formula is provided in Appendix A. The formula is valid when the two substrates have identical optical thicknesses. If not, we should follow a procedure to account for the difference in the optical thicknesses. This point is explained in section 2.7.1.

2.7 Transfer function fits

The most common analysis method is to consider the quotient $\tilde{E}_2(\omega)/\tilde{E}_1(\omega)$ as the transfer function and extract the complex conductivity from the Tinkham formula. A parameterized conductivity model can then be determined from a least-squares fit. However, since both the reference and sample pulses contain noise, their ratio will have noise that is not Gaussian, which can lead to biased least-squares parameter estimates. Consequently, we employ a maximum-likelihood (ML) method to estimate the model parameters [14]. We define the transfer function by the ratio of two polynomials of orders n_b and n_a:

$$\tilde{T}_{2,1}(s) = \frac{b_0 + b_1 s + b_2 s^2 + ... + b_n s^{n_b}}{a_0 + a_1 s + a_2 s^2 + ... + a_n s^{n_a}} \exp(-s\eta), \tag{2.3}$$

where $s = i\omega$ and η accounts for the possibility of mismatch in optical thicknesses between the sample and reference substrates. The transfer functions are classified by the order of the polynomials in the numerator and denominator, e.g., a (1,1) transfer function has $n_a = 1$ and $n_b = 1$. We use the (1,1) model to determine Drude parameters as discussed in section 2.7.2. In this model, we must fix one of the parameters to an arbitrary constant, e.g., $a_0 = 1$, to fix the overall parameter scale.

We assume that the raw spectra $\tilde{E}_2(\omega_i)$ and $\tilde{E}_1(\omega_i)$ are the sum of true spectra $\tilde{\phi}_2(\omega_i)$ and $\tilde{\phi}_1(\omega_i)$ together with uncorrelated noise spectra $\tilde{\varepsilon}_2(\omega_i)$ and $\tilde{\varepsilon}_1(\omega_i)$, respectively.

$$\tilde{E}_2(\omega_i) = \tilde{T}_{21}(\theta, \omega_\mathbf{i})\tilde{\phi}_\mathbf{1}(\omega_\mathbf{i}) + \tilde{\varepsilon}_\mathbf{2}(\omega_\mathbf{i}) \tag{2.4}$$

$$\tilde{E}_1(\omega_i) = \tilde{\phi}_1(\omega_i) + \tilde{\varepsilon}_1(\omega_i) \tag{2.5}$$

Here, the transfer function $\tilde{T}_{21}$ is parameterized by $\theta = [a_0, ..., a_{n_a}, b_0, ..., b_{n_b}, \eta]$. The parameter vector θ is determined by minimizing the cost function which has the following form [15]:

$$C(\theta) = \frac{|\tilde{E}_2(\omega_i) - T_{2,1}(\omega_i, \theta)\tilde{E}_1(\omega_i)|^2}{\sigma_2^2 + |\tilde{T}_{2,1}(\omega_i, \theta)|^2 \sigma_1^2}, \tag{2.6}$$

where σ_2^2 and σ_1^2 are noise variances that are estimated from $\tilde{E}_2(\omega)$ and $\tilde{E}_1(\omega)$ outside the signal bandwidth (3.1-5 THz). In the absence of systematic uncertainties, we can use this method to determine the goodness of the fits since the $C(\theta)$ should satisfy an F distribution [16]. When the fit is good, the statistical uncertainty in the parameter θ is determined from the covariance matrix $\mathbf{U} = (\mathbf{J}^T\mathbf{J})^{-1}$, where $\mathbf{J}$ is the Jacobian matrix of $C(\theta)$. Our systematic uncertainties are discussed in section 2.8.

2.7.1 Substrate characterization

In general, the substrate mismatch η can be determined by minimizing the cost function. However, there is a strong correlation between the scattering lifetime (τ) and substrate mismatch (η). We characterized the substrates used in this thesis prior to film deposition. This type of characterization requires two substrates from the same batch; one is reserved for the film deposition and one is kept as the reference substrate. At each temperature, we measure η associated with the difference in the optical thickness $D = n_s d_s$ between the two substrates. Here n_s and d_s denote the refractive index in the THz region and the substrate thickness respectively. In an actual experiment, we measure the transmission through the two substrates and form the complex transmittance $\tilde{T}_{2,1}(\omega)$ from their ratio in the frequency domain. Assuming $n_s(\omega) = n_s$, the complex transmittance will have the following form,

$$\tilde{T}_{2,1}(\omega) = \frac{\tilde{E}_s(\omega)}{\tilde{E}_r(\omega)} = \frac{b_0}{a_0} e^{\eta s}, \tag{2.7}$$

where we fix $a_0 = 1$. This is referred to as a (0,0) model since $n_a = n_b = 0$. In a typical experiment, we determine the substrate mismatch η within 2 fs uncertainty, which corresponds to a thickness mismatch (Δd_s) of $\sim$0.3 μm for a substrate with a refractive index of 3.

2.7.2 Drude model

The Drude model is the simplest classical treatment for transport properties of charge carriers in metals. The model is based on some crude assumptions, e.g. the frequency of electron-ion collisions is described by a mean free path λ and a mean collision time τ that are independent of position and momentum. Within these assumptions, an applied electric field $\tilde{E}(t) = E_0\, e^{-i\omega t}$ induces an average electron drift with the following frequency-dependent conductivity [17]:

$$\tilde{\sigma} = \frac{\sigma_0}{1 - i\omega\tau}, \tag{2.8}$$

where $\sigma_0 = n_c e^2 \tau / m^*$ is the DC conductivity, n_c is the carrier density, m^* is the effective carrier mass, e is the electric charge, and τ is the relaxation time. Despite its simplicity, over the THz bandwidth the model provides a reasonable description of DC and AC conductivity in many metals, including the chromium vanadium alloys studied in this thesis. For a Drude metal, the transfer function will have the following form, with $n_a = n_b = 1$:

$$\tilde{T}_{2,1}(s) = \frac{b_0 + b_1 s}{a_0 + a_1 s} e^{-s\eta} = \frac{-\frac{1}{\tau} + s}{-\frac{(1+\gamma)}{\tau} + s}, \tag{2.9}$$

where $\gamma = \sigma_0 Z_0 d_f/(n_s+1)$ and $b_1 = a_1 = 1$. This leaves b_0 and a_0 as free parameters to be determined from the maximum likelihood method described in section 2.7. This procedure enables us to extract the DC resistivity (ρ_0) and relaxation time (τ) from the (1,1) model:

$$\begin{aligned} \tau &= -\frac{1}{b_0}, \\ \rho_0 &= \frac{1}{\sigma_0} = \frac{Z_0 d_f}{n_s+1}\left(\frac{a_0}{b_0}-1\right)^{-1}. \end{aligned} \tag{2.10}$$

2.8 Measurement uncertainties

Multiple sources of statistical and systematic uncertainty exist in our measurement process. These uncertainties affect the quality of extracted parameter estimates and thus it is crucial to identify them in the optimization process. The three major sources of uncertainty are as follows: time-base drift, scattered THz radiation from sample apertures, and laser power fluctuations.

Time-domain fluctuations (time-base drift) mainly affect the measurement of the relaxation time. To characterize the drift, it is advantageous to focus on zero-crossing events in the signal. These are points at which the signal amplitude crosses zero with a large slope, so that any temporal drift produces large amplitude fluctuations. We measure the drift by fixing the delay stage at the zero-crossing and reading the lock-in voltage once per second with a lock-in time constant of 100 ms. We then convert the lock-in voltage to a time delay using the slope of the THz pulse at the zero-crossing point. Fig. 2.6 shows the correlation between the drift and laboratory temperature fluctuations over a 12-15 minute period. We suspected that the dominant contribution to the drift came from the thermal deflection of the 6-inch long, 1-inch diameter posts that supported the parabolic THz mirrors. It is not possible to reduce the height of the posts as we are restricted by the 6-inch height of cryostat windows. However, we recently replaced the parabolic mirror posts with 4-inch-diameter aluminum posts. This reduced the drift amplitude by a factor of 3.

Another source of uncertainty arises from THz radiation that is scattered from the sample edges and mixes coherently with the main signal. We consider a sample pulse transmitted through a thin film sample and a reference pulse transmitted through a phase-matched substrate in the time domain. Using the transfer function associated with the Drude model, we estimate the optimum parameters from the fit. With these parameters, the residuals are given by the difference between the predicted pulse and the measured pulse. In our measurements, the residuals exhibit structure and therefore are not statistically limited. Fig. 2.7(a) shows the time-domain residuals and the corresponding sample pulse transmitted through a Cr thin film sample at 290 K.

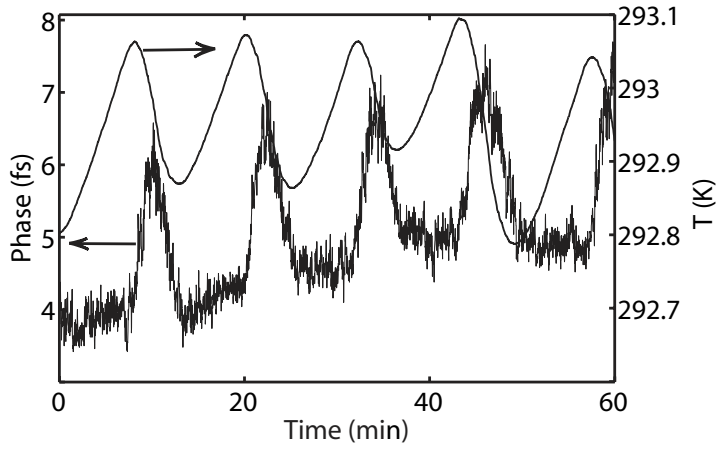

Figure 2.6: Simultaneous measurement of the time-base drift and laboratory temperature. The correlation between the drift and laboratory temperature fluctuations is clearly observed.

At temperatures above 100 K, the thermal expansion coefficient of the sample stick increases, producing a systematic uncertainty in the relative positions of the sample and the reference. The thermal expansion coefficient of the sample stick is small below the Debye temperature but increases linearly with increasing temperature. In our measurements, we account for the expansion of sample stick with increasing temperature, but the measurements are still prone to the scattered THz radiation from the apertures at high temperatures. Without accounting for the thermal expansion, the THz pulses scatter off the edges of the apertures, as can be seen for example at $t = 16$ ps in the time-domain residuals of Fig. B.2. This effect results in a systematic error in the relaxation time, of order 10 fs for every 100 K change in temperature.

We can use the maximum likelihood estimator $C(\theta)$ described in Chapter 2 to determine the goodness of the fits. Monte Carlo simulations show that the distribution for $C(\theta)$ is approximated well by an F-distribution [18]. In the $Cr_{1-x}V_x$ alloys studied in this thesis, most of the low-temperature $C(\theta)$ values indicate good fits, in that they are within the 95% confidence interval for the F distribution. As shown in Fig. 2.7(b), the residuals in the frequency-domain are heavily weighted towards low frequencies. In our data analysis, we typically avoid the low frequency regions below 500 GHz.

Another source of systematic uncertainty is associated with fluctuations in the mode-locked laser power. As shown in Fig. 2.8, the THz peak amplitude increases with increasing laser power with no sign of saturation. This means that fluctuations in the laser power appear directly as fluctuations

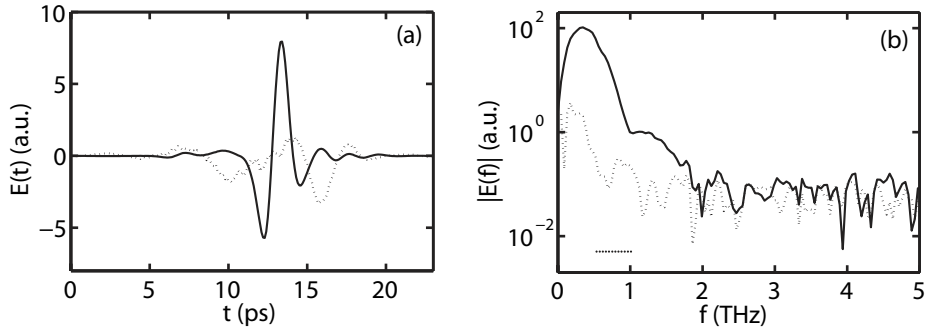

Figure 2.7: a) Sample pulse transmitted through Cr (solid lines) at 290 K and residuals (dashed lines) in the time domain. The time-domain residuals are scaled up by a factor of 20. b) Sample pulse (solid lines) and residuals (dotted lines) in the frequency domain.

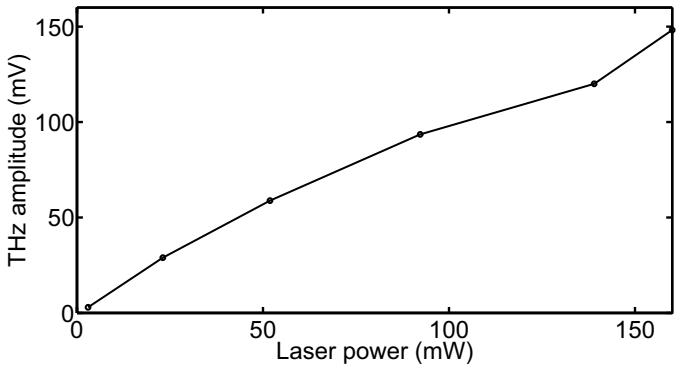

Figure 2.8: Measurement of laser power and THz peak amplitude. THz peak amplitude increases with increasing laser power without a sign of saturation.

in the THz amplitude. Ideally, THz antennas are operated in the saturated mode, where small laser fluctuations do not result in THz amplitude fluctuations. However, we do not have sufficient laser power to operate our antennas in the saturated mode. Currently, we observe about 1% variation in both the THz peak amplitude and laser power. This contributes excess noise at large signal amplitudes, well above the electronic noise in the detection system.

Chapter 3

THz time-domain spectroscopy of $Cr_{1-x}V_x$ films

3.1 Purpose of this study

Chromium alloys are of particular interest because of the variety of magnetic phases that they exhibit over a wide range of compositions, temperatures, pressures, and magnetic fields. In pure chromium, the Fermi surface geometry supports a spin-density-wave (SDW) ordered ground state that can be rapidly suppressed by tuning an external parameter such as alloy composition. From a fundamental point of view, chromium alloys are simple systems that are ideal for testing theoretical models concerning Fermi surface nesting [19]. The possibility of accessing a quantum phase transition (QPT) in a simple alloy motivated a large amount of theoretical and experimental work on these systems [19]. For example, the relationship between superconductivity and SDW order remains a key issue in strongly correlated systems. The discovery of iron-based superconductors provides a recent example. Both undoped LaFeAsO and $BaFe_2As_2$ exhibit a SDW ground state below 140 K [20, 21] and superconductivity emerges upon doping with 5% – 8% electrons per unit cell [22].

In the $Cr_{1-x}V_x$ system, Yeh *et al.* [23] performed Hall measurements and reported a sharp jump in the Hall coefficient as a function of vanadium concentration. They interpreted the sharp jump as an instability of the entire Fermi surface between the SDW phase and the paramagnetic state at the QPT. From Hall coefficient measurements, they speculated that the density of free carriers dropped discontinuously by a factor of two in the SDW state. Subsequent experiments that suppressed the SDW ground state with hydrostatic pressure instead of alloy composition showed that the jump in

the Hall effect was actually continuous across the transition, and was qualitatively explained by the formation of the SDW gap over the large flat regions of Fermi surface [24, 25].

We have applied the Hall technique and THz-TDS to $Cr_{1-x}V_x$ thin film samples and tracked the loss of free carriers across the QPT. Both techniques reveal a factor of two change in the carrier density as the material evolves from an SDW ground state to a paramagnetic ground state. However, the thin film samples exhibited significantly higher disorder than in single crystals, broadening the quantum phase transition so that neither technique revealed the sharp zero-temperature change in carrier density observed in Hall effect measurements of single crystals. We compared the temperature dependence of the plasma frequency inferred from the two techniques and found quantitative differences at low temperatures that we tentatively attribute to anisotropic scattering.

THz-TDS measurements were performed in transmission mode, and therefore we are restricted to use thin films instead of bulk single crystals. We worked with [100] $Cr_{1-x}V_x$ epitaxial films on $15 \times 15 \times 1$ mm MgO [100] substrates. Film thicknesses ranged from 30 to 40 nm and vanadium concentration varied from 0 to 8%. The residual resistivity ratio of $\rho(300K)/\rho(15K) \sim 4$ for a typical film compares well with other epitaxial $Cr_{1-x}V_x$ films [26] but is two orders of magnitude smaller than the best values reported in bulk $Cr_{1-x}V_x$ [23], indicating a relatively high degree of disorder.

3.2 Background

The earliest speculation on the antiferromagnetic ordering in chromium was made by Louis Néel in 1936. Microscopic evidence was provided by Shull *et al.* through a neutron diffraction experiment on powdered chromium in 1953 [27]. They found a magnetic (0,0,1) peak that is forbidden from atomic cores in body-centered cubic chromium. The magnetic reflection peak disappeared at temperatures above 475 K.[1] In 1959, Bykov *et al.* and Corliss *et al.* independently reported magnetic satellites at (0,0,1$\pm\delta$) in addition to the antiferromagnetic peak of (0,0,1) [29, 30]. The satellite peaks correspond to wave vectors $\mathbf{Q}_{\pm} = \frac{2\pi}{a}(0,0,1\pm\delta)$ with a deviation of $\delta \sim 0.035$ just below the Néel temperature (T_N), where a denotes the lattice constant. In 1962, Shirane *et al.* proposed an antiferromagnetic ordering with a sinusoidal modulation of magnetic moments [31]. They reported a continuous increase in the modulation period from $\sim$21 unit cells at 78 K to $\sim$28 just below T_N.

[1] This temperature is higher than the Néel temperature of 311 K in single crystals. It is currently known that internal strain affects the transition temperature [28].

From these experimental observations, the magnetic structure in chromium can be expressed as:

$$\mu_{\pm} = \mu_{\mathbf{0}} \sin(\mathbf{Q}_{\pm}\mathbf{r}), \tag{3.1}$$

with $\mu_0 \sim 0.5\ \mu_B$ at 4.2 K. This magnetic structure is called the spin density wave (SDW). As shown

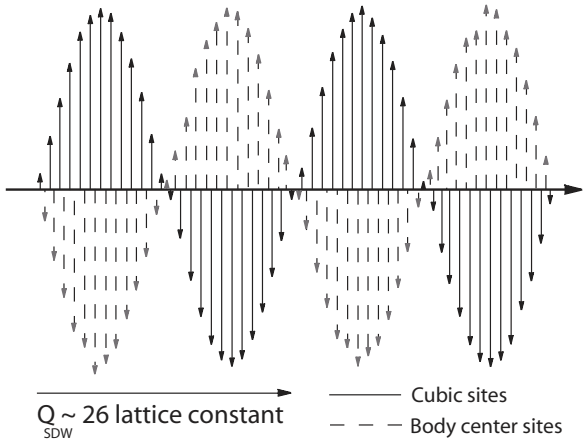

Figure 3.1: Magnetic structure in chromium with a modulation period of ~ 26 lattice constants. The solid lines show the magnitude of magnetic moments on the corner atoms, and the dashed lines show the magnitude of magnetic moments on the body center atoms.

in Fig. 3.1 for $\delta = 0$, the magnetic moments on the cubic lattice points corresponds to $\mu = +\mu_0$ and the magnetic moments on the body-centered basis atoms at **r**=(1/2,1/2,1/2) corresponds to $\mu = -\mu_0$. The magnetic state in chromium is an incommensurate SDW ($\delta \neq 0$) since the modulation wavelength is not an integer multiple of the lattice constant. Lomer was the first to relate the shape of the Fermi surface in chromium to its magnetic state [32]. He realized that the chromium Fermi surface consists of parallel electron and hole surfaces that can be mapped into one another by the wave vectors $\mathbf{Q}_{\pm}$, as shown in Fig. 3.2. This attribute is referred to as nesting. Electrons in these regions of the Fermi surface are excited at the nesting wavevectors with a very low energy cost. This leads to a large contribution in the magnetic susceptibility as described in Section 4.2.1. The Fermi surface consists of an electron octahedron centered at Γ, slightly larger octahedra centered on the H-points ($\frac{\pi}{a}$,0,0), hole ellipsoids centered at the N-points ($\frac{\pi}{2a}$,$\frac{\pi}{2a}$,0), and small electron lenses along the Γ-H lines, all shown in the (001) cross section of Fig. 3.2.

Overhauser argued that a three-dimensional free electron gas has a generic instability toward SDW formation [34]. He calculated that the formation of electron-hole pairs lowers the energy of the system and leads to an energy gap in the single-particle spectrum. The energy gap was observed experimentally as a dip in the reflectivity spectrum at an energy of $\sim$0.13 eV in the magnetic

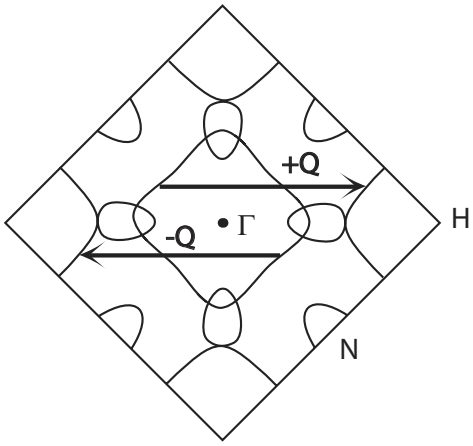

Figure 3.2: A sketch of the (001) cross-section of the Fermi surface in paramagnetic chromium over the first Brillouin zone. The electron octahedron centered at Γ and slightly larger hole octahedra centered on the H-points have approximately parallel surfaces that are connected by the wavevectors $\pm\mathbf{Q}$. The electron lenses intersect the electron octahedron and touch the hole octahedron at high-symmetry points where band degeneracies occur. Adapted from Ref. [33].

state [35], consistent with the Overhauser prediction [35, 34]. Soon afterwards, the gap was detected in de Haas-van Alphen (dHvA) measurements of Graebner and Marcus [33]. More recently, angle-resolved photoemission spectroscopy (ARPES) confirmed the location of the energy gaps on the nested regions of the Fermi surface [36].

3.2.1 Density wave instability

The origin of the SDW can be understood by analogy with the density-wave instability that generically occurs in one dimension. The ability of itinerant electrons to screen a perturbation is reflected in the response function $\chi(Q,\omega)$. The density response of the electron gas to a perturbing potential of arbitrary wavelength is defined as [37]

$$\delta\rho(Q,\omega) = \chi(Q,\omega)V(Q,\omega), \tag{3.2}$$

where the Q-dependent dynamical susceptibility $\chi(Q,\omega)$ is

$$\chi(Q,\omega) = \frac{2}{V}\int \frac{n_k - n_{k+Q}}{\varepsilon_{k+Q} - \varepsilon_k - \hbar(\omega)}dk, \tag{3.3}$$

with n_k the occupation number of the k-state and ε_k the dispersion relation. Equation 3.3 is derived from second order perturbation theory [37]. To illustrate the mechanism, we calculate the DC

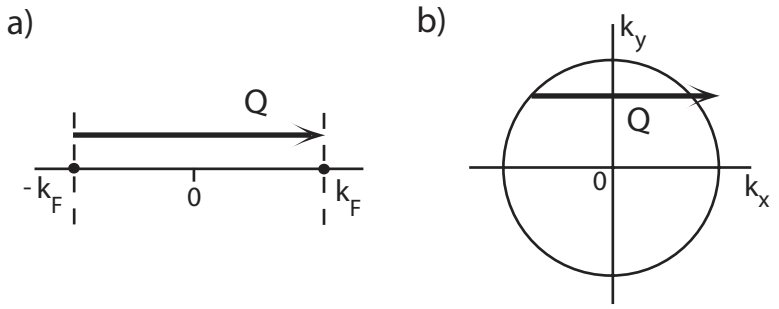

Figure 3.3: a) Perfect mapping of Fermi surface points with a single wavevector Q in one dimension. b) A circular Fermi surface in two dimensions, for which a single wavevector Q does not span the Fermi surface at all locations.

susceptibility for a one-dimensional metal at zero temperature. As shown in Fig. 3.3(a), the Fermi surface in one dimension consists of two isolated points at $\pm k_F$. At zero temperature, the integrand of Eqn. 3.3 is non-zero if only one of the states $|k\rangle$ or $|k+Q\rangle$ is occupied; that is, when $n_k = 1$ and $n_{k+Q} = 0$ or $n_k = 0$ and $n_{k+q} = 1$. In one dimension, the DC susceptibility is then reduced to:

$$\chi(Q,0) = \frac{m}{\pi\hbar Q} \ln \left| \frac{Q+2k_F}{Q-2k_F} \right|. \tag{3.4}$$

The response function (susceptibility) exhibits a logarithmic divergence at $Q = 2k_F$. This implies a divergent change in the density response for a weak perturbing potential that implies a density wave instability. In a real system, electron-electron interactions provide the potential.

This instability is associated with the perfect mapping of all points of the Fermi surface by a single wavevector **Q**, and is thereby limited to one dimension. A circular Fermi surface in two dimensions is shown in Fig. 3.3(b). With no dominant spanning wavevector in two dimensions and higher, the response function integral does not diverge, but exhibits discontinuous derivatives at $2k_F$.

3.2.2 SDW ground state in chromium

Density wave instabilities can occur in higher dimensions under favorable circumstances, for example if a sufficiently large portion of the Fermi surface has a one-dimensional character. This readily happens when the Fermi surface has large parallel portions that can be related by translations through a single wavevector. As illustrated in Fig. 3.4(a), the electron and hole octahedra in chromium have almost identical shapes. This leads to a divergence in the magnetic response at wavevectors that connect the two surfaces, resulting in an SDW instability. The potential at wavevector **Q** connects states on one side of the electron octahedron with the corresponding side of the hole octahedron. For

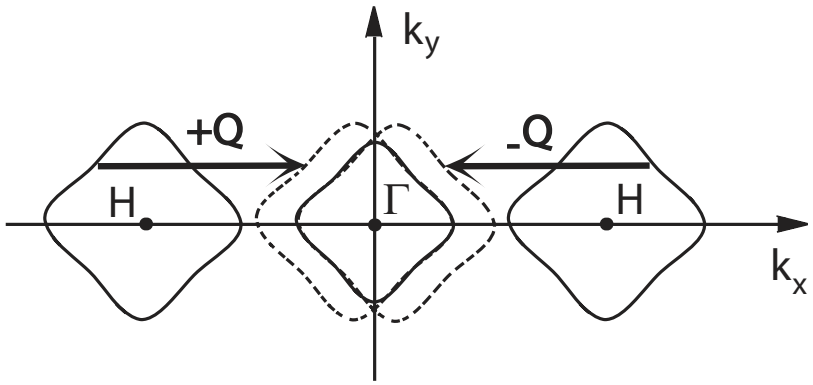

Figure 3.4: Solid lines show the electron sheet centered at Γ and two hole sheets centered at H. Dashed lines show the hole sheets after translation through nesting wavevectors $\pm\mathbf{Q}$.

a sufficiently strong potential, an energy gap can appear in the energy spectrum at the Fermi level wherever $\varepsilon(k) = \varepsilon(k \pm Q)$. Angle resolved photoemission spectroscopy (ARPES) of chromium thin films reveals a complete gapping of the nested regions of Fermi surface at low temperatures [36]. Chromium exhibits both bulk and surface magnetic transitions [36], and ARPES primarily probes the surface properties. The ARPES energy gap of $\sim$200 meV covers the entire flat portions of the electron and hole octahedra. Above the near-surface transition at 440 K, the gap disappears and the paramagnetic Fermi surface is restored. The loss of conduction electrons also has a dramatic effect on the Hall coefficient [38]. This is explained in detail in Section 3.3.

3.2.3 Binary Chromium alloys

In pure chromium, the electron Fermi volume is slightly smaller than the hole Fermi volume, resulting in nesting wavevectors $\mathbf{Q}_\pm$ that are slightly incommensurate with the lattice. The incommensurate state can be transformed into a commensurate state by introducing small amounts of transition metals impurities such as Mn, Re, or Ru. These elements have higher electron concentration per unit cell and bring the electron and hole Fermi surfaces closer in size. Increasing the electron Fermi volume eventually leads to a triple point on the concentration-temperature phase diagram where the SDW, incommensurate SDW (ISDW) and paramagnetic (P) phases coexist [19]. In contrast, vanadium doping increases the hole concentration and makes the magnetic structure more incommensurate, while also reducing the transition temperature. Compared to chromium, vanadium has a similar atomic mass, so doping with vanadium is not expected to significantly disturb the phonon-dispersion relations [19].

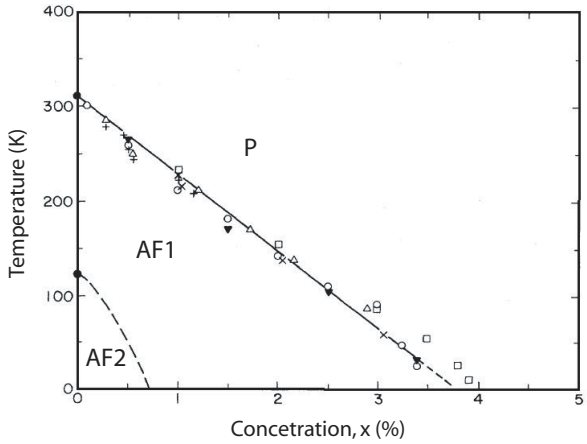

Figure 3.5: Magnetic phase diagram of $Cr_{1-x}V_x$ showing the suppression of Néel temperature as a function of vanadium concentration. The dashed line shows the transition from a longitudinal spin direction (AF2) to a transverse spin direction (AF1). Adapted from Fawcett *et al.* [19]; used with permission.

The magnetic phase diagram of $Cr_{1-x}V_x$ is shown in Fig. 3.5. At zero temperature, adding a small amount of vanadium rapidly suppresses the ordered state at a critical concentration of about 3.45%. The dashed line in the phase diagram shows the spin-flip transition (SF), where the spin polarization changes from the longitudinal direction below T_{SF} to a transverse direction above T_{SF}.

3.3 Hall effect in $Cr_{1-x}V_x$

Yeh *et al.* [23] performed Hall measurements on $Cr_{1-x}V_x$ alloys with concentrations that spanned the quantum phase transition at $x = 0.035$. As shown in Fig. 3.6(c), they reported that the Hall coefficient jumped sharply by a factor of two upon entering the ordered state. Norman *et al.* [25] explained the sharpness of the transition by considering a realistic model of how the Fermi surface changes with magnetic ordering. Within the relaxation time approximation, the Hall coefficient is defined as $R_H = \sigma_{xyz}/\sigma_{xx}^2$, where

$$\sigma_{xyz} = \frac{e^3\tau^2}{\hbar\Omega c}\sum_{\vec{k}} v_x(\vec{v}\times\vec{\nabla}_k)_z v_y\left(-\frac{\delta f}{\delta\varepsilon_k}\right), \tag{3.5}$$

$$\sigma_{xx} = \frac{e^2\tau}{\Omega}\sum_{\vec{k}} v_x^2\left(-\frac{\delta f}{\delta\varepsilon_k}\right). \tag{3.6}$$

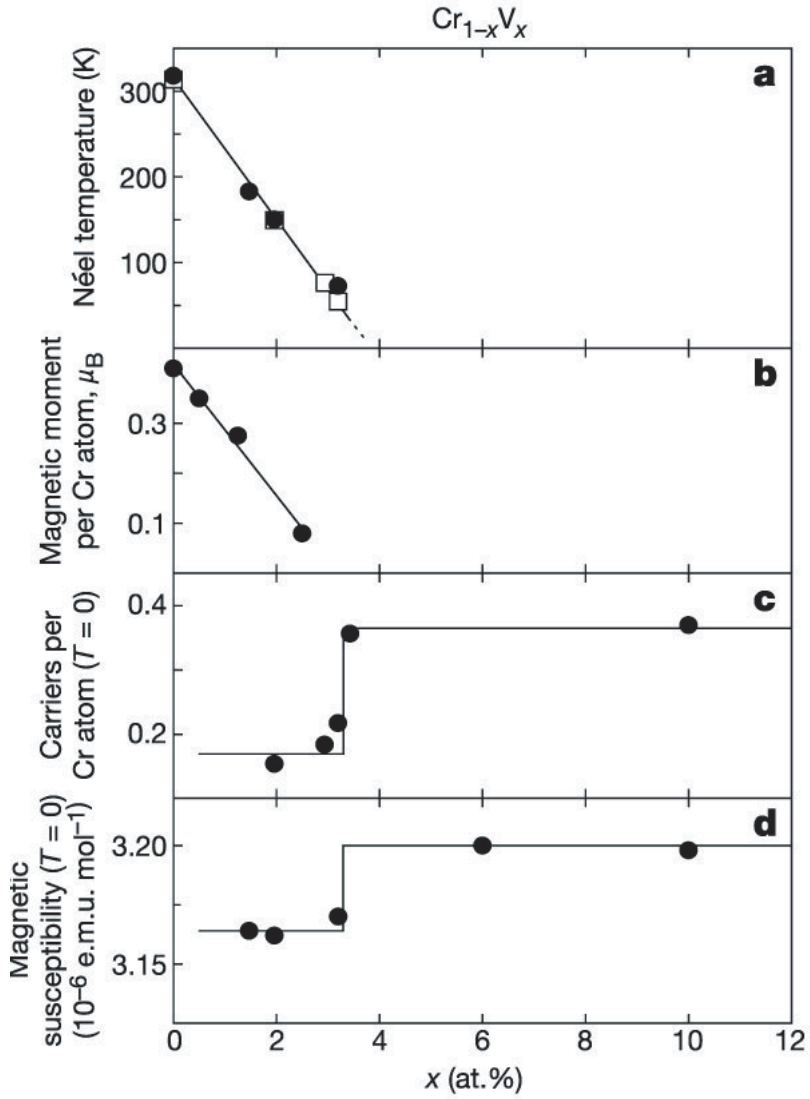

Figure 3.6: a) Suppression of the Néel temperature with increasing vanadium concentration. b) Magnetic moment measured by magnetic neutron diffraction [39] at 4.2 K. c) Carrier density obtained from the inverse Hall coefficient (T $<$ 5 K). d) Magnetic susceptibility (T $<$ 5 K). From Yeh et al [23]; used with permission.

Here, τ is the scattering lifetime, Ω is the volume, and f is the Fermi distribution function. Norman *et al.* suggested that the sharp jump in the zero-temperature Hall coefficient arises from the geometry of the Fermi surface. They pointed out that σ_{xyz} depends on the curvature of Fermi surface and contains negligible contribution from the flat Fermi surface portions in the paramagnetic state. As a result, σ_{xyz} is not expected to change significantly at the QPT. On the other hand, σ_{xx} contains only the velocity components and is affected strongly by the removal of the flat regions of the Fermi surface in the magnetic state. The effect is amplified because the square of σ_{xx} appears in the Hall coefficient denominator.

While the Norman *et al.* [25] argument provides a quantitative description of the sharp zero-temperature change in carrier density observed in Hall effect measurements, their argument also emphasizes the importance of the Fermi surface shape when inferring the carrier density from Hall data. In contrast, the plasma frequency measured in optics is relatively insensitive to the shape of Fermi surface, as can be seen from Eq. 3.6 and $\sigma_{xx} = \varepsilon_0 \omega_p^2 \tau$. In this work, we use THz-TDS to estimate the plasma frequency, as a complementary probe of carrier density.

3.4 THz-TDS on $Cr_{1-x}V_x$

3.4.1 Conductivity spectra

We use time domain THz spectroscopy (THz-TDS) to determine the complex conductivity of $Cr_{1-x}V_x$ for various values of x. The complex conductivity of pure Cr and $Cr_{0.973}V_{0.027}$ at selected temperatures is shown in Fig. 3.7. The dashed curves represent the Drude fits. The data points are calculated from direct quotients of the $\tilde{T}_{2,1}(\omega) = \tilde{E}_2(\omega)/\tilde{E}_1(\omega)$ and the Tinkham formula. The fits are calculated by minimizing $|\tilde{E}_2(\omega) - \tilde{T}_{2,1}(\omega)\tilde{E}_1(\omega)|^2$ with the maximum likelihood denominator explained in Ch. 2. To calculate the fits, we limit the THz bandwidth to the range 500-1000 GHz where the systematic uncertainties are minimized, as described in Ch. 2. For ease of interpretation, we limit the conductivity spectra to frequencies in the range 250-800 GHz. Below 250 GHz, the systematic uncertainty associated with positioning error increases, due to the large size of the THz beam. The large beam diameter makes the measurements more sensitive to scattered THz radiation from the sample apertures. Above 800 GHz, the noise power density becomes comparable to that of the signal. A more detailed discussion of the systematic uncertainties is provided in Ch. 2. The optical conductivity within the limited bandwidth is adequately described by the Drude model.

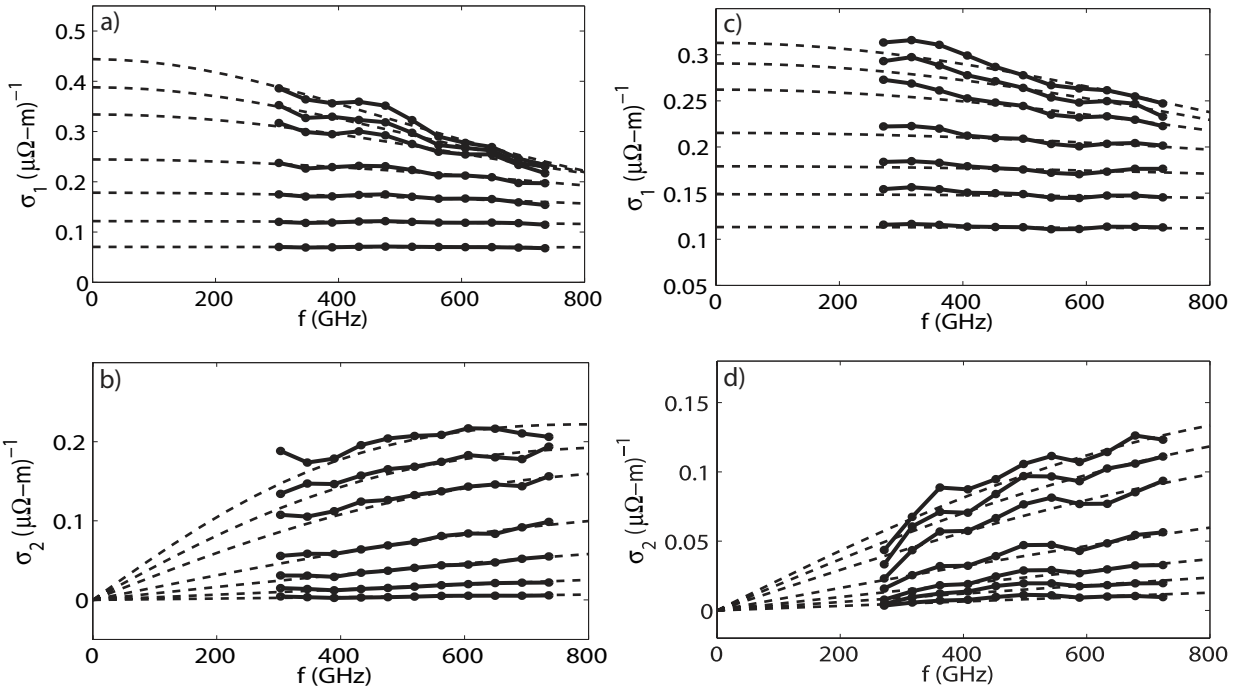

Figure 3.7: a) Real and b) Imaginary parts of the optical conductivity of Cr at T=30, 60, 75, 100, 125, 150, and 200 K. c) Real and d) Imaginary parts of the optical conductivity of $Cr_{0.973}V_{0.027}$ at T=30, 60, 75, 100, 125, 150, and 200 K. Dashed curves show Drude fits at the selected temperatures.

3.4.2 Resistivity

Zero-frequency extrapolations $\rho(T) = 1/\sigma(\omega \to 0, T)$ yield the resistivity as a function of temperature. The results for samples with vanadium concentrations of 0, 2.7, 3.1, and 4.3% are shown in Fig. 3.8. Standard four-point measurements are made on the same samples and the agreement between the two techniques is shown. A discussion on the agreement between the two techniques is provided in Appendix B. The measured resistivity as a function of temperature and vanadium

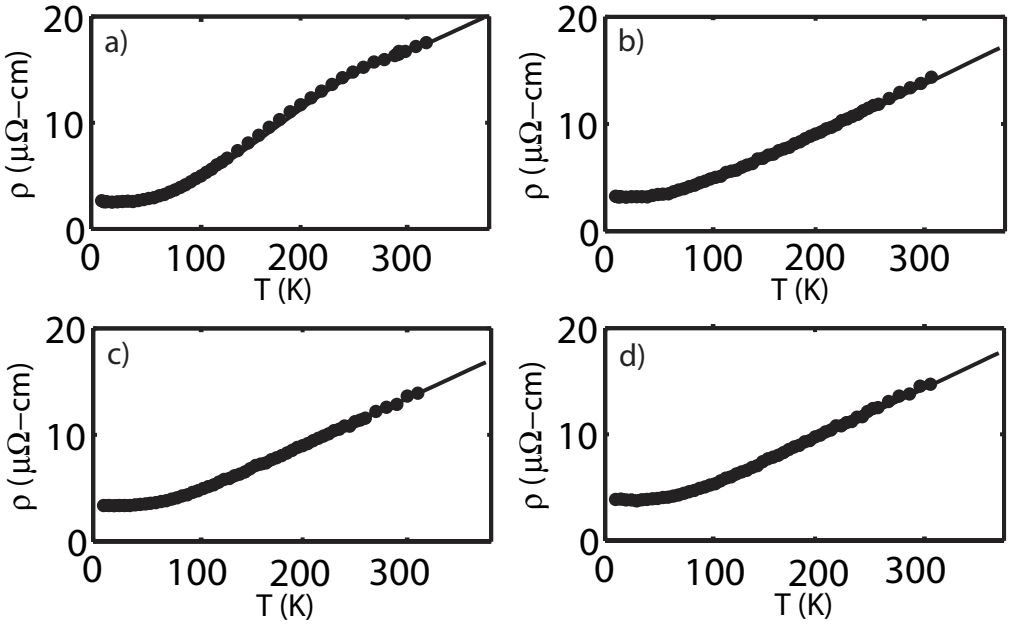

Figure 3.8: Resistivity as a function of temperature for samples with a) 0, b) 2.7%, c) 4.15% and d) 4.3% vanadium concentration. Filled circles and solid curves denote the THz-TDS and standard four-point measurements, respectively.

concentration is consistent with earlier resistivity measurements on single crystals, but with a larger elastic impurity scattering contribution. As shown in Fig. 3.10(a), the low-temperature resistivity varies as T^3 below 100 K, in accordance with Yeh *et al.* [23]. Moreover, the residual resistivity increases weakly with doping in the magnetic phase, in accordance with Takeuchi *et al.* [40], and it changes smoothly through the QPT, as observed by Yeh *et al.* [23]. This agreement suggests that Matthiessen's rule is obeyed and that the resistivity of $Cr_{1-x}V_x$ alloys has the form [41]:

$$\rho = \rho_r(x) + \rho_L(x, T), \tag{3.7}$$

where $\rho_r(x)$, the residual resistivity, is a function of concentration x, while $\rho_L(x,T)$ depends on both x and T and represents the contribution to the resistivity from temperature-dependent scattering processes.

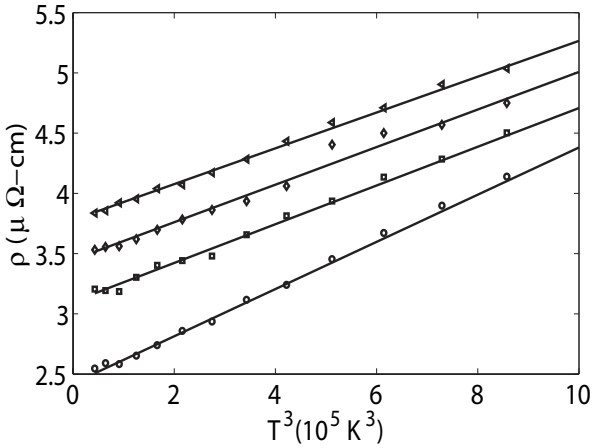

Figure 3.9: Low temperature resistivity as a function of T^3 for 4.3%, 3.1%, 2.7%, and 0% vanadium doped samples, respectively from the top.

The first derivative of resistivity with respect to temperature shows a local minimum that is related to the SDW transition, as indicated in Fig. 3.9. This minimum becomes broader and shifts to lower temperatures with increasing vanadium concentration. By tracking these minima from the data in Fig 3.8, we observe a rapid suppression of the SDW phase at the QPT. As shown in Fig. 3.10(b), the Néel temperatures obtained from the resistivity anomaly in CrV thin films are consistent with earlier work. For pure chromium, $T_N \sim 300$ K is slightly lower than the value observed in single crystals ($T_N = 311$ K). A lower Néel temperature for films has been previously reported [42] and could be related to the constraint imposed by the MgO substrate [28].

3.4.3 Relaxation time

The relaxation times as a function of temperature in samples with vanadium concentrations of 0, 2.7, 3.1, 4.15, and 4.3% are shown in Fig. 3.11. An increase in the vanadium concentration monotonically lowers the low-temperature relaxation time from $\sim$200 fs in pure chromium to $\sim$85 fs near the QPT. In the paramagnetic phase, doping further lowers the low temperature relaxation time to $\sim$40 fs at $\sim$8% doping. Within $\pm$5 fs, the room-temperature relaxation time is independent of vanadium concentration on both sides of QPT.

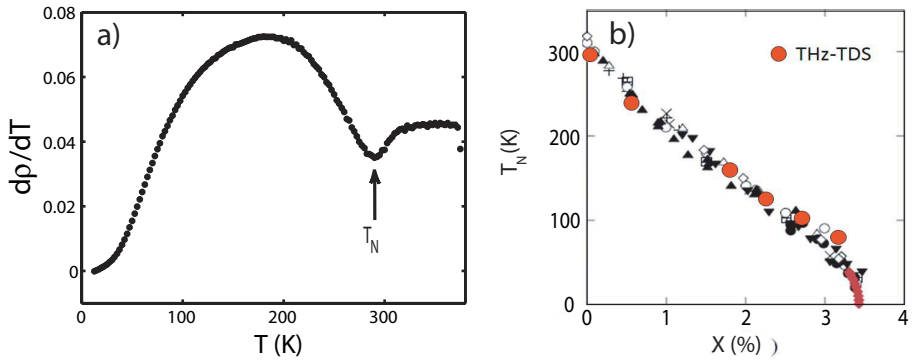

Figure 3.10: a) First derivative of resistivity with respect to temperature in pure Cr. The arrow indicates the local minimum that occurs at the Néel temperature. b) Magnetic phase diagram of $Cr_{1-x}V_x$ showing the suppression of Néel temperature as a function of vanadium concentration. The large circles indicates the Néel temperature derived from the THz-TDS resistivity anomaly. From Lee *et al.* [24]; used with permission.

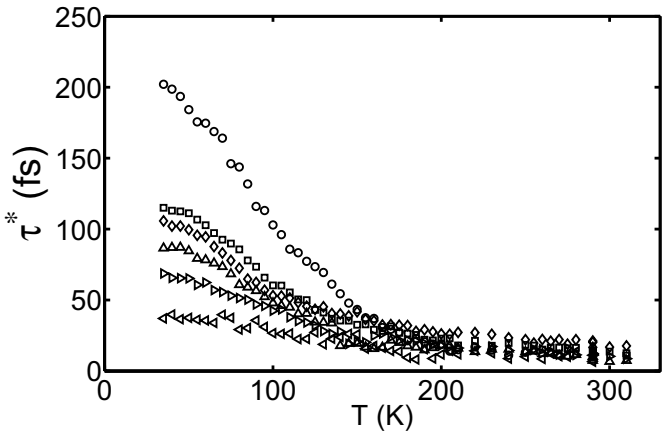

Figure 3.11: Relaxation time as a function of temperature for samples with 0 (○), 2.7 (□), 3.1 (◇), 3.45 (△), 4.15(▷), and 8% (◁) vanadium concentration. The low-temperature relaxation time decreases monotonically with increasing vanadium concentration.

3.4.4 Plasma frequency

From measurements of the relaxation time and resistivity we can determine the plasma frequency (ω_p), a fundamental ground-state property of the Fermi surface that is given by

$$\omega_p^{-2} = \varepsilon_0 \rho \tau. \tag{3.8}$$

For a spherical Fermi surface, the plasma frequency is related to the density of carriers through $\omega_p = (n_c e^2/m^* \varepsilon_0)^{1/2}$, where n_c is the carrier density, e is the electric charge, ε_0 is the permittivity of free space, and m^* is the effective mass. Ditusa *et al.* performed de Haas-van Alphen (dHvA) measurements on $Cr_{1-x}V_x$ and obtained $m^* = 0.5\ m_0$, independent of vanadium concentration over a doping range of 0–5% [43]. However, the dHvA technique is sensitive primarily to the hole ellipsoids and is relatively insensitive to the large nested region of the Fermi surface, while both Fermi surface sheets will contribute equally to the plasma frequency [43].

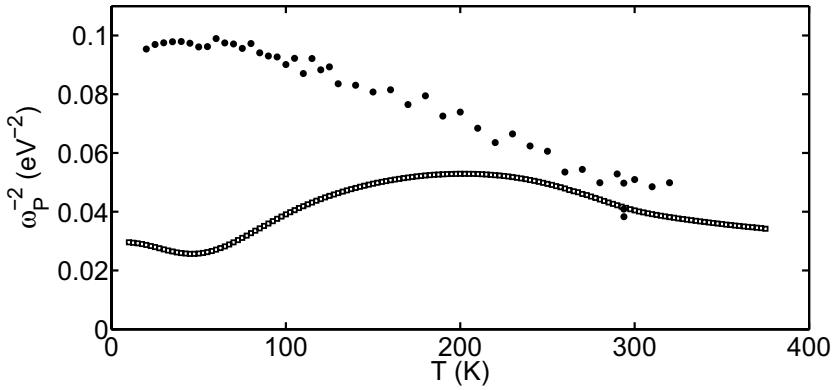

Figure 3.12: Temperature dependance of ω_p^{-2} in pure Cr. Filled circles and empty squares correspond to the THz-TDS and Hall measurements, respectively.

For comparison, we performed Hall measurements on a number of samples under a magnetic field of 5 kG. In each sample, we measure the Hall resistance, R_H, in the range of 10-375 K. The temperature dependence of ω_p^{-2} inferred from the Hall and THz-TDS measurements for pure chromium are compared in Fig 3.12. The Hall coefficient shows a rapid drop at about 50 K that has been attributed to the anisotropy of Umklapp scattering processes at low temperatures [38]. This feature appears in the low-temperature Hall coefficient of many metals, including ones with nearly spherical Fermi surfaces like Li, Ag, Au, and Mo [38]. In chromium, it has been shown that the minimum occurs between 30 and 50 K, depending on the magnetic field strength [38]. As the magnetic field

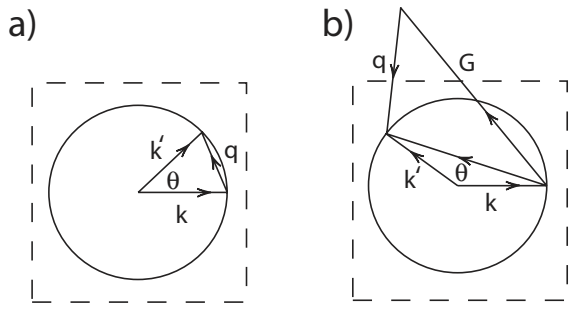

Figure 3.13: a) Normal scattering process on a spherical Fermi surface. b) Umklapp scattering process on a spherical Fermi surface. Dashed lines denote the boundary of first Brillouin zone.

is increased from 1 kG to 25 kG, the minimum becomes more pronounced and shifts to higher temperatures.

3.4.5 Anisotropic scattering

The minimum in the Hall effect is most pronounced in pure chromium and gradually disappears with vanadium substitution. At about 2% vanadium concentration the Hall effect becomes monotonically decreasing with increasing temperature, signalling a crossover to a different transport regime. Here I provide a qualitative explanation of the low-temperature disagreement in ω_p^{-2} between the THz-TDS and Hall measurements in the range of 0–2% vanadium concentration, based on anisotropic scattering.

Examples of normal and Umklapp scattering processes are shown in Fig. 3.13. Umklapp scattering processes involve a phonon with a momentum $\mathbf{q} = \mathbf{k}' - \mathbf{k} - \mathbf{G}$ outside the first Brillouin zone, where $\mathbf{G}$ is a reciprocal lattice vector [41]. As the temperature is lowered, this scattering channel becomes less effective as the phonon population decreases. At low temperatures, the average number of phonons with an energy $\varepsilon_{\mathbf{q}}$ is given approximately by the Boltzmann distribution:

$$< n_q > \sim \exp\left(-\frac{\varepsilon_{\mathbf{q}}}{k_B T}\right). \tag{3.9}$$

Umklapp processes are known to be highly anisotropic at low temperatures even for a spherical Fermi surface [41]. The anisotropy is stronger when the Fermi surface touches the boundary of the first Brillouin zone, as shown in Fig. 3.14. For a given initial state $\mathbf{k}$, the phonon momentum $\mathbf{q}$ with the smallest amplitude $q_{\min}$ will connect $\mathbf{k}$ to the neck point, resulting in a final state $\mathbf{k}'$ at a neck point on the opposite side of the Brillouin zone. This shows that the Umklapp scattering can play an important role even at the lowest temperatures. In general, the value of q_{min} determines the minimum

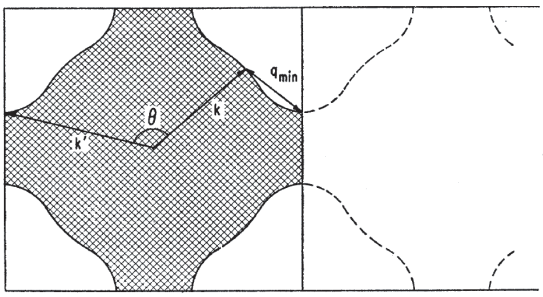

Figure 3.14: Umklapp process for copper in the repeated Brillouin zone. From Ziman *et al.* [44]; used by permission.

temperature at which the Umklapp process occurs. In contrast, the belly point on the Fermi surface is far away from the zone boundaries and further from the points in the repeated zone. The Umklapp scattering from these points are frozen out at low temperatures. From the Fermi surface shown in Fig. 3.14, Ziman *et al.* estimated a scattering anisotropy of $\tau_{\text{belly}}/\tau_{\text{neck}} \sim 2.2$ at $T = 0.2\ T_D$, where T_D is the Debye temperature [44].

For a spherical Fermi surface, Trofimenkoff estimated the Umklapp scattering anisotropy by considering the partial resistivities over the Fermi surface [45]. Using the Debye spectrum model, they reproduced the low-temperature resistivity of potassium and showed that the temperature dependence of the anisotropy ratio $<\tau(k,T)>^2 / <\tau(k,T)^2>$ closely follows the temperature dependence of the Hall coefficient. The estimated scattering anisotropy is shown in Fig. 3.15. As shown in Appendix C, this anisotropy ratio is proportional to the effective electron density n^*, as estimated from Hall measurements:

$$\frac{n^*}{n} = \frac{<\tau>^2}{<\tau^2>}, \tag{3.10}$$

where n is the mean electron density obtained by assuming a constant scattering rate over the entire Fermi surface. We claim that THz-TDS produces a more reliable estimate of carrier density at low temperatures because it is insensitive to this anisotropy in the scattering processes.

In $Cr_{1-x}V_x$ with $x \geq 0.02$, the rapid drop in the Hall coefficient disappears. Moreover, we observe a weak increase in the residual resistivity with increasing vanadium concentration in the magnetic phase. This suggests that elastic scattering increases with increasing vanadium concentration and may become the dominant scattering mechanism for vanadium concentrations of 2% and higher. We expect this elastic scattering to be more isotropic, resulting in better agreement between the Hall effect and the THz-TDS measurements.

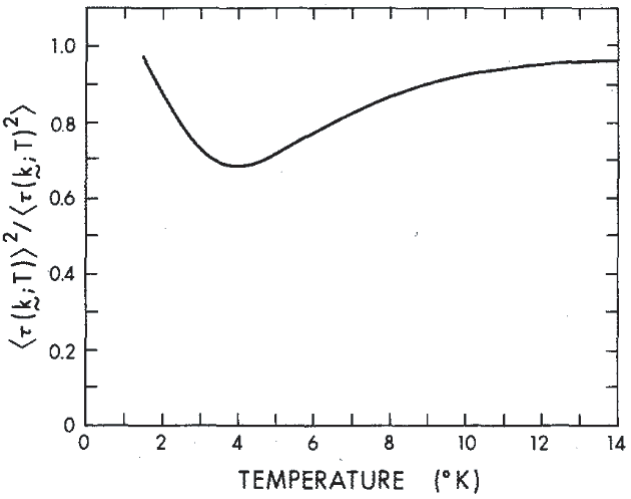

Figure 3.15: Temperature dependence of $< \tau(k,T) >^2 / < \tau(k,T)^2 >$ obtained from the partial resistivities over a spherical Fermi surface [45]. From P. N. Trofimenkoff [45]; used with permission

3.4.6 Quantum phase transition

Fig. 3.16 shows the low-temperature values of ω_p^{-2} as a function of vanadium concentration, as inferred from both Hall and THz-TDS measurements, assuming an effective mass $m^* = m_e$ and including only Hall measurements for $x > 0.02$. Neither THz-TDS nor Hall measurements reveal a sharp jump in the density of states at the QPT [23]. Instead, we observe a smooth loss of free carriers upon entering the SDW state. We believe that the sharp jump in the density of states is smeared by disorder in the thin-film samples. Nonetheless, the data clearly indicate an increase in the carrier density as the SDW transition is suppressed.

The temperature dependence of ω_p^{-2} inferred from Hall effect and THz-TDS measurements in $Cr_{1-x}V_x$ for x=2.7, 4.15 and 4.3% are compared in Fig 3.17. In samples that exhibit an SDW ground state, both measurements reveal a temperature dependence to ω_p^{-2} that clearly reflects the density of states reduction as the SDW gap removes parts of the Fermi surface. Above the critical vanadium concentration, the temperature dependence is weaker but still persists, suggesting that the carrier density is depleted by magnetic fluctuations above the QPT.

Although both Hall and THz-TDS measurements reveal a depletion in the density of states as the temperature is lowered, below $T \sim 75$ K they exhibit quantitative differences. For $35 \leq T \leq 75$ K, THz-TDS measurements indicate a carrier density that is 15% higher than that measured with the Hall effect. We observe this low-temperature disagreement in the doping range between 2 to 4.3%,

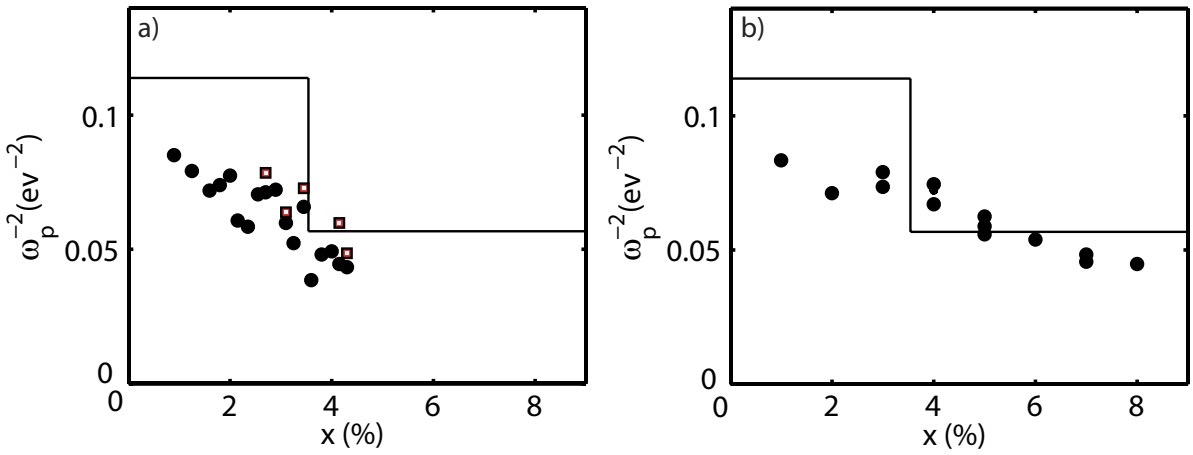

Figure 3.16: a) Concentration dependence of low temperature ω_p^{-2}. Filled circles and empty squares correspond to ω_p^{-2}, inferred from the THz-TDS and Hall measurement respectively. The values are averaged over the temperature range of 35-75 K. Solid lines are the fits to the earlier Hall measurements on $Cr_{1-x}V_x$ single crystals [23]. b) THz-TDS results on a new set of samples with vanadium concentration extended to 8%.

which includes both sides of the QPT. Assuming the disagreement is related to the Fermi surface nesting in the magnetic state, it is not surprising to see this behavior even above the QPT. Inelastic neutron scattering experiments reveal strong magnetic fluctuations even at 5% vanadium doped chromium [46], and the strong temperature dependence of Hall coefficient has led to speculations about a pseudogap region near the QPT [23].

For the chosen effective mass of $m^* = m_e$, this low-temperature disagreement cannot be explained by the anisotropic scattering. In contrast to the doping range below 2%, the low-temperature values of ω_p^{-2} inferred from the Hall measurements are higher than those of THz-TDS. If we use $m^* = 0.5m_e$, as measured by dHvA technique [43], the low-temperature values of ω_p^{-2} inferred from the Hall measurements are reduced by a factor of 2 and falls under those of THz-TDS. In this case, the low-temperature disagreement might be explained by the anisotropic scattering but it creates a puzzling high-temperature disagreement. These considerations suggest that we are either using an incorrect value for the effective mass or the nature of anisotropy below and above 2% vanadium doping is different. At the moment the origin of this difference in temperature variation remains unexplained and warrants further study.

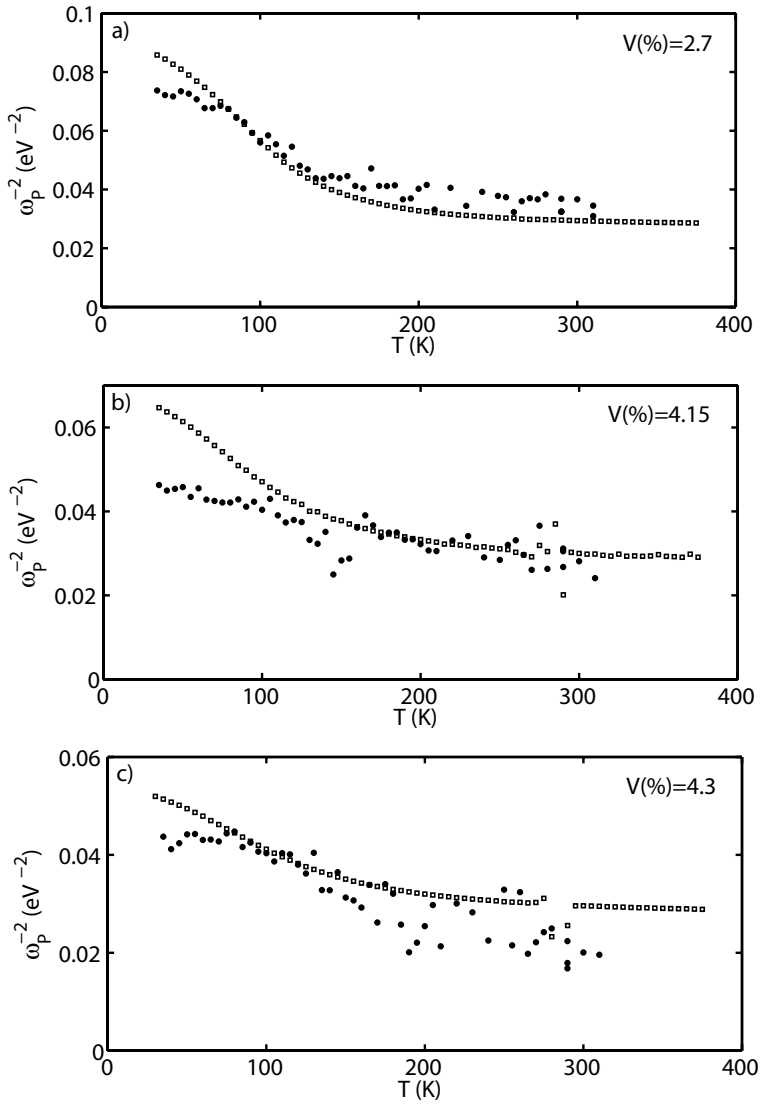

Figure 3.17: a-c) Temperature dependence of ω_p^{-2} in $Cr_{1-x}V_x$ for x=2.7, 4.15 and 4.3%, respectively. Filled circles and empty squares correspond to the THZ-TDS and Hall measurement, respectively.

.

3.5 Conclusion

THz-TDS and Hall measurements are commonly used to infer the conduction carrier density. It is known that each technique uses different averaging techniques over the Fermi surface. We applied the Hall technique and THz-TDS to $Cr_{1-x}V_x$ thin film samples and tracked the loss of free carriers across the QPT by estimating the plasma frequency. For $x > 0.02$, both techniques reveal the opening of the SDW gap and a factor of two change in the carrier density as the material undergoes the magnetic transition at QPT. However, neither of the techniques reveal the zero-temperature jump in carrier density at the QPT. We compared the temperature dependence of the plasma frequency inferred from the two techniques and found quantitative differences at low temperatures.

In $Cr_{1-x}V_x$ with $0 \leq x \leq 0.02$, Hall measurements reveal a minimum in ω_p^{-2} at about 50 K that had been attributed to the anisotropy in the scattering time. We qualitatively explained the low-temperature disagreement between the two techniques by considering a spherical Fermi surface and calculating the ratio of carrier densities estimated from each technique. In this simplified scenario, we determined that our THz-TDS technique is insensitive to the scattering time anisotropy and yields a more reliable estimate of carrier density. In $Cr_{1-x}V_x$ with $0.025 \leq x \leq 0.043$, THz-TDS indicates a higher number of carriers by 15% than the Hall effect at low temperatures. We could not explain this low-temperature disagreement by considering a simple model and suspect that it could be related to the way the real $Cr_{1-x}V_x$ Fermi surface is treated in each technique. To address this issue, a realistic Fermi surface should be considered. The results should be further supplemented by considering disorder.

Chapter 4

Visible-pump, THz-probe spectroscopy

In this chapter, I discuss the theoretical and experimental aspects of the visible-pump, THz-probe spectrometer in our laboratory. The spectrometer was originally designed to study the intrinsic photoconductivity of insulating cuprates. In order to create a high density of photoexcitations (10^{19} cm^{-3}), we employ an amplified laser system that provides 850 mW of average power with a repetition rate of 1 kHz. We use 90% of the total laser power to photoexcite the samples and the remaining power to probe with THz-TDS, using optical rectification and electro-optic sampling.

4.1 Amplified Ti:sapphire laser

We use a commercial Ti:sapphire regenerative amplifier [47] (SP Spitfire 50 fs) to drive the visible-pump, THz-probe spectrometer. A schematic of the main units in the amplifier system is shown in Fig. 4.1. There are four main units:

1) A mode-locked Ti:sapphire oscillator (KML) delivers 30 fs pulses, centered at 800 nm with a 100 MHz repetition rate and an average power of 550 mW. We use 50% of the total power, while the other half is used for the linear THz-TDS setup. The Ti:sapphire oscillator is CW pumped with 4.1 W at $\lambda = 532$ nm, using a commercial CW Nd:YLF laser (SP Millennia V).

2) A grating-based pulse stretcher introduces strong group velocity dispersion to stretch the 30 fs pulses by as much as a factor of 10^4. The diffraction gratings are arranged so that the high-frequency components lag behind the low-frequency components (positive chirp). This procedure is used to reduce the peak intensity of the laser pulse before seeding it into the amplifier. A high intensity

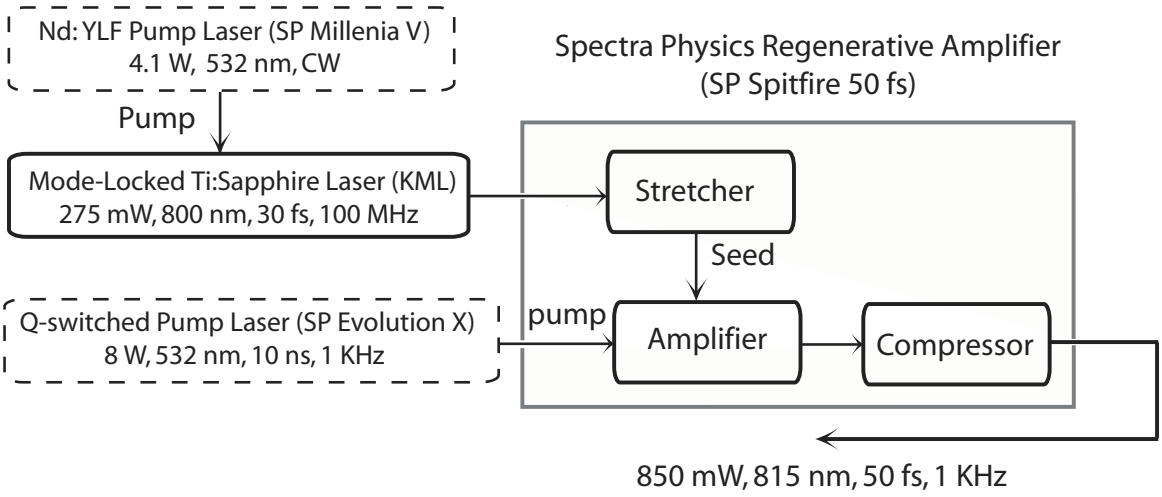

Figure 4.1: Schematic of the Ti:sapphire regenerative amplifier. The Spitfire amplifier is pumped with 10 ns pulses at $\lambda = 532$ nm, and seeded by 30 fs pulses with $\lambda = 800$ nm from a mode-locked laser. Ultrafast pulses are stretched prior to amplification. Once they are amplified, the stretched pulses are recompressed to 50 fs pulsewidth.

pulse with short duration can damage the amplifier gain-medium.

3) A Ti:sapphire regenerative amplifier is designed to amplify pulses from the mode-locked Ti:sapphire laser (seed). The amplifier is pumped with a commercial Q-switched pump laser (SP Evolution X) that produces 10 ns pulses centered at 532 nm with a 1 kHz repetition rate and an average power of 8 W. The pump laser excites the Ti:sapphire crystal of the regenerative amplifier and turns it into a gain medium for approximately 70 ns. A Pockels cell allows a single stretched pulse to enter the amplifier cavity and gain energy from the excited crystal. Once it is amplified, a second Pockels cell lets the amplified pulse out of the cavity resonator.

4) A grating-based pulse compressor compensates for the group velocity dispersion of the stretcher and the multiple passes through the amplifier cavity, to recompress the amplified pulse to 50 fs pulsewidth.

The technique of using the dispersive delays to stretch a pulse prior to amplificaion and recompress it afterward is known as chirped pulse amplification (CPA). A schematic of the CPA technique is shown in Fig. 4.2.

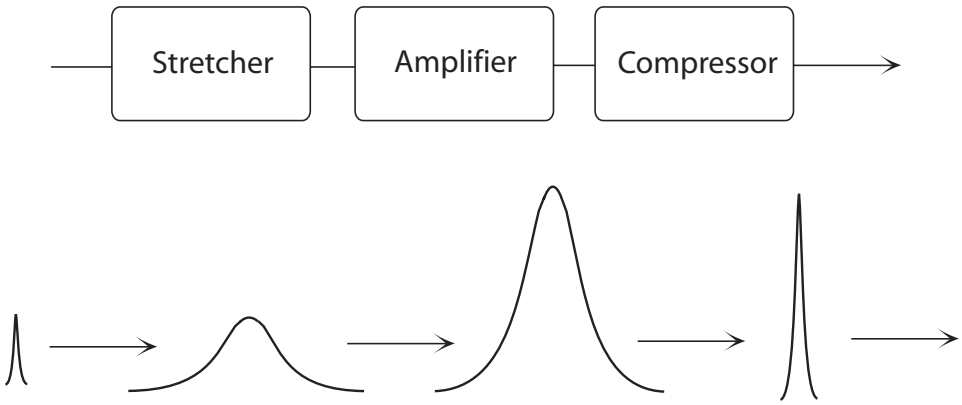

Figure 4.2: Schematic of the chirped pulse amplification technique. An ultrashort laser pulse is stretched in time prior to amplification. Once it is amplified, the high-energy stretched pulse is recompressed.

4.2 Optical rectification

The electric polarization $P(t)$ can be expressed as a power series of the field strength [48]:

$$P(t) = P^{(1)}(t) + P^{(2)}(t) + P^{(3)}(t) + ... = \chi^{(1)}E(t) + \chi^{(2)}E^2(t) + \chi^{(3)}E^3(t) + ... \,. \tag{4.1}$$

For simplicity, we assume that the polarization $P(t)$ and electric field $E(t)$ are scalar quantities, and that the medium responds spontaneously to the electric field. In general, $P(t)$ and $E(t)$ are vectors, χ_1 is second-rank tensor, χ_2 is a third-rank tensor, etc. In reality, the medium has its own dynamics and produces a much more complicated structure to the equation that we can ignore for the purpose of this discussion.

Optical rectification is a second order nonlinear effect and occurs in crystals without inversion symmetry. Consider two optical fields $E_1(t) = A_1(t)\cos(\omega_1 t + \delta_1)$ and $E_2(t) = A_2(t)\cos(\omega_2 t + \delta_2)$, where $A_1(t)$ and $A_2(t)$ are the slowly varying envelopes of carrier waves at ω_1 and ω_2. We assume $\delta_1 = \delta_2 = 0$ to focus on the basic frequency mixing process, although in general this will not be satisfied at all locations and times in the nonlinear optical medium. The second order nonlinear polarization has the following form:

$$\begin{aligned} P^{(2)} &= \chi_2 A_1(t)\cos(\omega_1 t) A_2(t)\cos(\omega_2 t), \\ &= \frac{1}{2}\chi_2 A_1(t) A_2(t)[\cos(\omega_1 - \omega_2)t + \cos(\omega_1 + \omega_2)t], \\ &= P^{(2)}(\omega_1 - \omega_2) + P^{(2)}(\omega_1 + \omega_2). \end{aligned} \tag{4.2}$$

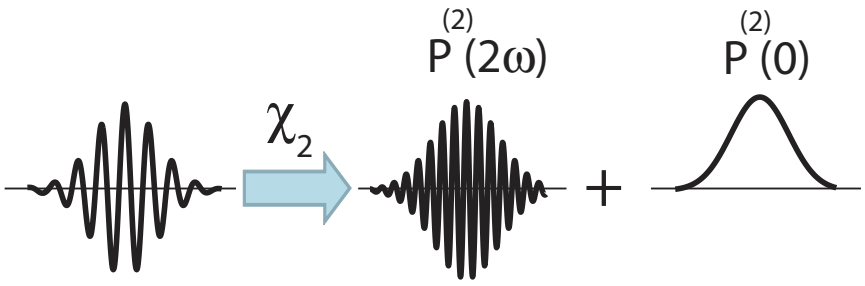

Figure 4.3: Time-domain illustration of SHG and optical rectification processes. The second order polarization oscillates at the sum (SHG) and difference (optical rectification) of the driving frequencies.

The terms $P^{(2)}(\omega_1 - \omega_2)$ and $P^{(2)}(\omega_1 + \omega_2)$ correspond to polarization oscillations at the difference and sum of the incident frequencies, respectively. For two identical incident fields, the second order nonlinear polarization is reduced to:

$$\begin{aligned} P^{(2)} &= \frac{1}{2}\chi_2 A^2(t) + \frac{1}{2}\chi_2 A^2(t)\cos(2\omega t), \\ &= P^{(2)}(0) + P^{(2)}(2\omega). \end{aligned} \tag{4.3}$$

The $P^{(2)}(2\omega)$ term contains oscillations at twice the carrier frequency and is associated with an effect known as second harmonic generation (SHG). The $P^{(2)}(0)$ term appears at DC in this treatment, but for short laser pulses with center frequency ω it is proportional to the square of the incident field envelope. The process of producing this polarization is called optical rectification and is relevant to THz generation. The time domain picture of these processes is illustrated in Fig. 4.3.

In our case, optical rectification may be considered as difference frequency generation (DFG) between the longitudinal modes of a mode-locked laser. A mode-locked laser spectrum consists of distinct, phase-locked frequency components equally spaced by the inverse of the pulse repetition rate. When such an electric field is applied to a medium with an appropriate χ_2, the nonlinear polarization oscillates at the sum and difference of each pair of frequencies within the spectrum. The difference polarization term has a spectrum centered at $\omega = 0$ but with several THz of bandwidth, depending on the χ_2 and the duration of the incident optical pulse [49, 48].

The efficiency of this processes is limited by the mismatch between the phase velocity of the THz pulse and the group velocity of the incident optical pulse [48]. The phase mismatch corresponds to the out-of-phase propagation of the THz and optical pulses and results in destructive interference

throughout the crystal. The length over which this mismatch is tolerated is given by [50]:

$$l_c = \frac{\pi c}{\omega_{\mathrm{THz}} \mid n_{\mathrm{opt}}^{(\mathrm{eff})} - n_{\mathrm{THz}} \mid}, \tag{4.4}$$

with

$$n_{\mathrm{opt}}^{(\mathrm{eff})} = n_{\mathrm{opt}} - \lambda_{\mathrm{opt}} \left(\frac{\partial n_{\mathrm{opt}}}{\partial \lambda} \right) |_{\lambda_{\mathrm{opt}}}, \tag{4.5}$$

where c is the light velocity, ω_{THz} the THz frequency, $n_{\mathrm{opt}}^{(\mathrm{eff})}$ the group velocity refractive index of the optical pulse, n_{THz} the medium refractive index in the THz region, and n_{opt} the medium refractive index at optical wavelength λ_{opt}. Efficient optical rectification occurs when the coherence length (l_c) is longer than the nonlinear crystal thickness. In ZnTe, the coherence length is 3 mm at $\omega_0 = 800$ nm and $\omega_{\mathrm{THz}} = 1$ THz [50]. In our setup, we use a 0.5 mm ZnTe crystal to generate THz pulses.

4.3 Electro-optic sampling

In electro-optic sampling, the instantaneous electric field of the THz pulse induces a small birefringence in an electro-optic crystal. An optical pulse (probe) gains a small ellipticity in the polarization when it passes through such a crystal. For small applied fields, the induced ellipticity is proportional to the instantaneous THz electric field.

The optimum orientation of the incident THz field, the optical probe field, and the ZnTe crystals is shown in Fig. 4.4. In our setup, we use a 1-mm thick $\langle 110 \rangle$-oriented ZnTe as an electro-optic crystal. ZnTe is a cubic crystal of $\bar{4}3m$ symmetry class with three non-zero electro-optic tensor elements $r_{41} = r_{52} = r_{63} = 3.9$ pm/V [49]. When the THz electric field is oriented along $\langle 1\bar{1}0 \rangle$, it induces a birefringence with natural axes that are identified as $\hat{\mathbf{x}}$ and $\hat{\mathbf{y}}$ in Fig. 4.4. When the optical probe pulse passes through the crystal, the probe beam acquires the following phase shift between the birefringent modes [49],

$$\Delta\phi \propto n_0^3 r_{41} E_{\mathrm{THz}} d, \tag{4.6}$$

where n_0 is the crystal refractive index, E_{THz} is the amplitude of the THz pulse, and d is the crystal thickness. After passing through the ZnTe crystal, the probe beam goes through a quarter-wave plate and then a Wollaston prism that separates the vertical and horizontal polarizations. Finally, a pair of photodiodes is used to read the signal. A schematic of this process is shown in Fig. 4.5. By measuring the electro-optic phase shift as a function of the delay between the THz and optical probe

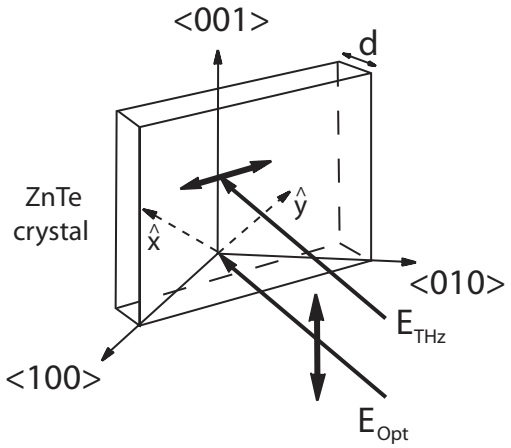

Figure 4.4: Electric field orientation together with the polarization of THz and optical pulses with respect to the ZnTe crystal. This geometry corresponds to the optimal electro-optic phase modulation.

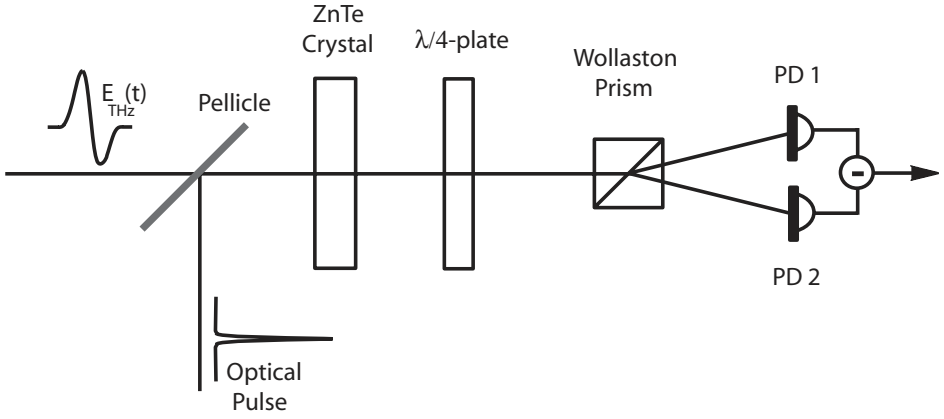

Figure 4.5: Schematic of electro-optic sampling. The sampling beam and THz pulses are directed into a ZnTe in a collinear fashion. The incident THz pulse induces a birefringence in the ZnTe crystal which is proportional to the THz electric field. This varying birefringence is measured by monitoring the change in polarization state of the optical probe pulse. The transmitted probe beam goes through a quarter-wave plate that converts the ellipticity into polarization rotation by inducing a phase delay. Finally, a Wollaston prism separates the vertical and horizontal polarizations and a pair of balanced photodiodes is used to read the signal.

pulse, the entire time profile of the THz field is mapped. According to Eq. 4.6, this detection method is sensitive to both the magnitude and sign of the THz field.

By introducing a quarter-wave plate before the Wollaston prism, the induced ellipticity is converted into polarization rotation with an angle that is proportional to the THz field. After the probe beam is transmitted through the Wollaston prism, the intensity difference between the polarizations along the *x* and *y* directions of the crystal is measured with a lock-in amplifier by chopping the probe beam at 500 Hz. In practice, small misalignments can produce an imbalance in the absence of an applied field. We compensate for this by blocking the THz beam and adjusting the quarter-wave plate orientation to null the differential signal.

4.4 Spectrometer layout

The spectrometer is driven by optical pulses from a Spectra Physics regenerative amplifier that provides pulses of 50 fs duration centered at $\lambda = 815$ nm with a 1 kHz repetition rate and an average power of 850 mW. A detailed schematic of the visible-pump, THz-probe spectrometer is shown in Fig. 4.6. The laser beam is split into two arms: one arm (10% of total power) is used for THz generation and detection, and the other (90%) is used for creating photoexcitation in samples. The less intense beam is then divided into two parts using a 8-92% pellicle: one part (92%) is used for THz generation and the other (8%) is used for THz sampling. THz pulses are generated via optical rectification in a 0.5-mm thick $\langle 110 \rangle$ ZnTe crystal. The generated THz beam is collimated and focused onto the sample using a pair of 45° off-axis parabolic mirrors. Compared to the 90° off-axis parabolic mirrors, these mirrors are more compact and produce less 3rd-order abberation. The sample is located in an Oxford cold finger cryostat that is capable of controlling temperature over a range of 5-340 K. The transmitted THz pulses are then collimated and focused onto a 1-mm thick $\langle 110 \rangle$ ZnTe crystal using another pair of 45° off-axis parabolic mirrors.

Just before the ZnTe crystal, a pellicle is placed in the THz path to direct the optical probe and THz beams collinearly through the ZnTe crystal. The incident THz pulse induces a birefringence in the ZnTe crystal that is proportional to the THz electric field. This varying birefringence is measured by monitoring the change in polarization state of the optical probe pulse. After the ZnTe crystal, the optical probe beam goes through a quarter wave-plate, then a Wollaston prism that splits the vertical and horizontal polarizations. A pair of balanced photodiodes is used to read the signal. The probe beam is chopped at 500 Hz, and the differential voltage of the photodiodes is measured with a lock-in amplifier that is referenced to the chopper.

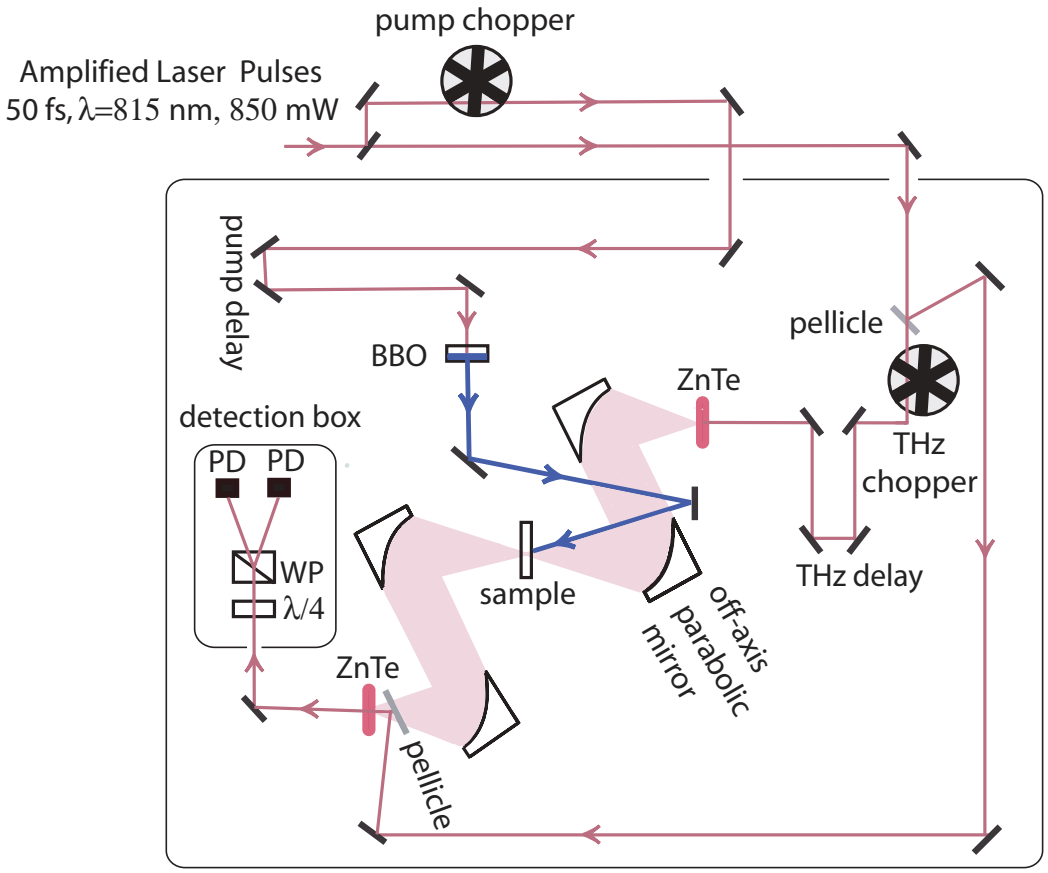

Figure 4.6: Optical layout of the visible-pump, THz-probe spectrometer. The amplified laser beam is divided into two parts: one part is used for THz generation and detection, and the other part is used for photoexciting the sample. The THz arm is then divided into two parts using a pellicle: one part is used for THz generation and the other is used for THz detection. THz pulses are generated via optical rectification in a ZnTe crystal. The generated pulses are collimated and focused onto the sample and then directed to another ZnTe crystal using 45° off-axis parabolic mirrors. Using a second pellicle, the sampling beam is also directed into the ZnTe in a collinear fashion. The sampling beam is then transmitted through a quarter-wave plate and a Wollaston prism before arriving at the balanced photodiodes. About 90% of total laser power is frequency doubled with a BBO crystal and used for creating optical excitations in the sample.

About 90% of total laser power is used for optical excitation, as described in Sec. 4.6. To create photocarriers in the sample, we use optical second-harmonic generation to double the pump photon energy from 1.52 eV to 3.04 eV, using a 1-mm crystal of β-barium borate (BBO) that has a conversion efficiency of 15%. Right after the BBO crystal, a blue-pass filter blocks the residual 815 nm light. The final pump mirror is mounted as close as possible to the edge of the second parabolic mirror to minimize the angle between their propagation directions. In our spectrometer, there is a 10° angle between the two beams. This limits the temporal resolution to about 2.9 ps because one side of the 5 mm diameter pump beam arrives before the other.

To ensure that the THz pulse probes a uniformly photoexcited area, the pump beam spot size should be larger than that of the THz probe. The parabolic mirrors focus the THz probe onto the sample to a spot radius of 1.1 mm or less above 500 GHz, and 2.9 mm at 200 GHz. We provide uniform illumination for most of the THz frequencies in the spectrum by setting the pump beam radius to be 2.2-2.5 mm at the sample. This suggests that THz probe beam do not probe a uniformly photoexcited area below 200 GHz. The knife-edge method used in measuring the pump beam radius is discussed in Appendix D.

4.5 THz pulses

To measure the THz pulse, a chopper is used to modulate the sampling beam at 500 Hz. The chopper frequency is set to half of the laser repetition rate, so that every other pulse is completely blocked. A lock-in amplifier that is phase locked to the chopper frequency is used to retrieve the measured signal. By varying the delay between the THz and sampling beams, the entire THz pulse is measured in the time domain.

With no sample in the THz beam path, a typical THz time-trace is shown in Fig. 4.7(a). Compared to the linear THz spectrometer described in Ch. 2, the measurement process of the pump-probe system must be adapted to the lower modulation frequency of the amplifier laser systems. In our experiments, we typically sample the THz waveform with 128 points spaced by 0.05 ps. The sampling time corresponds to a Nyquist frequency of 10 THz, well beyond the signal bandwidth. We set the lock-in time constant to 500 ms as there is a trade-off between the noise reduction and measurement time. The ratio of the maximum amplitude at 0.5 THz and the averaged noise floor yields an SNR of about 100. This is at least an order of magnitude lower than the antenna-based systems, for which the laser noise performance is better and the lock-in modulation frequency is higher.

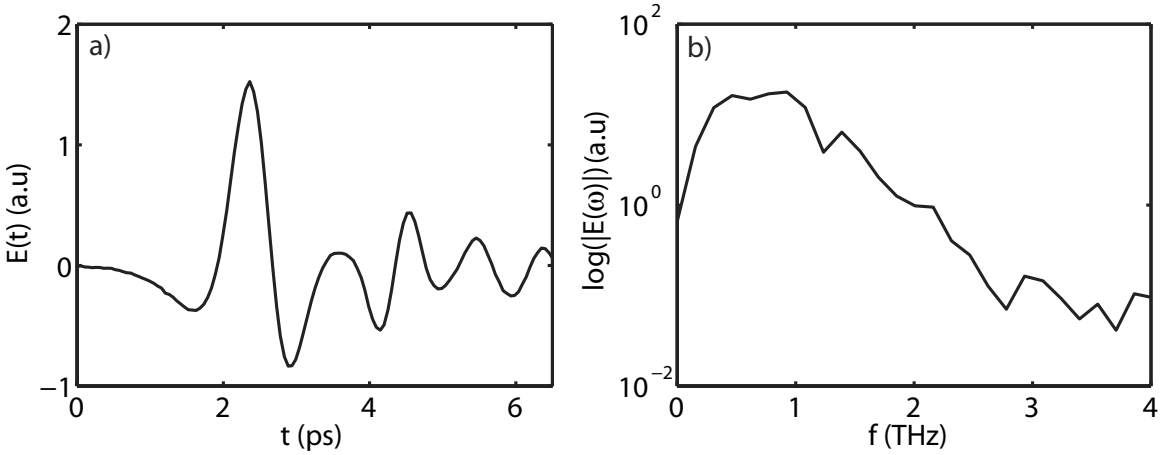

Figure 4.7: a) A typical time-domain THz pulse through air. b) Spectrum of the THz pulse.

4.6 Measurement process

In the pump-probe measurement, an ultrafast optical pulse creates photocarriers in the sample and a subsequent THz pulse probes the nonequilibrium state. The optical pulse creates a photoexcited layer that is similar to a metallic film on a substrate. We define an effective film thickness to be the optical penetration depth or $1/e$ intensity decay length, assuming a simple exponential absorption. A schematic of the visible-pump, THz-probe technique is shown in Fig. 4.8.

We modulate the pump beam and measure the pump-induced change in the THz amplitude, $\Delta E(t,\tau) = E_{\text{pump on}}(t,\Delta\tau) - E_{\text{pump off}}(t)$, where $\Delta\tau$ is the delay between pump and probe pulses and t is the THz-delay time. To determine the THz spectrum as a function of time delay requires THz difference scans (ΔE) at a series of pump-probe delays $\Delta\tau$ before and after photoexcitation. This procedure is referred to as a 2D scan [51]. To extract the conductivity, the modulation $\Delta E(t,\Delta\tau)$ is referenced to the transmitted THz field through the unexcited sample $E(t)$. The profile of the reference field $E(t)$ is measured by modulating the THz beam when the pump beam is blocked. Rearranging the Tinkham formula [13],

$$\tilde{\sigma}(\omega,\tau) = -\frac{n_s+1}{Z_0 d_f}\frac{\Delta\tilde{E}(\omega,\tau)}{\tilde{E}(\omega)}\left(1-\frac{\Delta\tilde{E}(\omega,\tau)}{\tilde{E}(\omega)}\right)^{-1} \tag{4.7}$$

where d_f denotes the penetration depth, Z_0 the impedance of free space, and n_s the refractive index of the unexcited samples in THz region.

To observe the decay dynamics with better resolution, we can fix the THz delay stage at the peak THz amplitude $t = t_{\text{p}}$ and monitor the change in the THz amplitude $E(t = t_p)$ as a function of

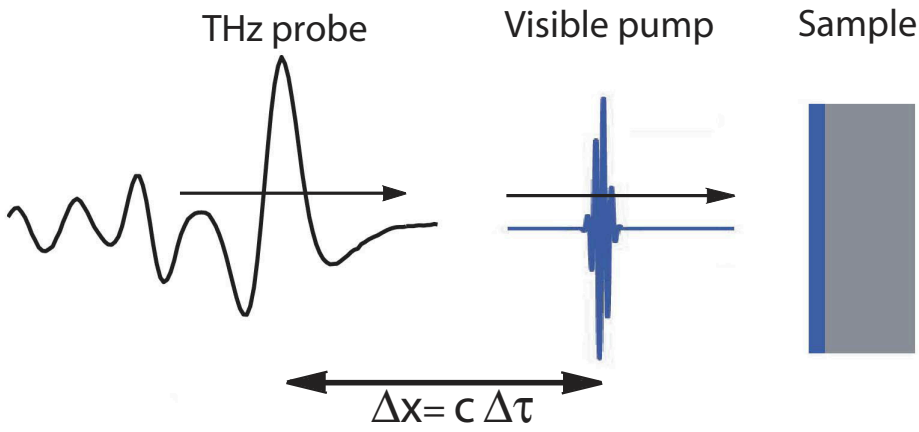

Figure 4.8: Schematic of visible-pump, THz-probe technique. We apply ultrafast optical pulses to create photocarriers in the sample and use THz pulses to probe the nonequilibrium state as a function of the pump-probe delay $\Delta\tau$.

pump-probe delay $\Delta\tau$, $\Delta E(t = t_{\rm p}, \Delta\tau)$. This procedure is referred to as a 1D pump scan [51]. We also measure the peak THz amplitude transmitted through the unexcited sample $E(t = t_p)$. From the ratio of $\Delta E(t = t_{\rm p}, \Delta\tau)/E(t = t_p)$ and assuming a frequency-independent conductivity in Eq. 4.7, we can estimate the photoconductivity as a function of pump-probe delay. We note that this estimate contains contributions from all frequencies within the experimental bandwidth, and hence it is referred to as spectrally averaged conductivity.

4.6.1 Results on GaAs

To validate the measurement procedure, I present results on a $\langle 100 \rangle$-orientated GaAs sample. The analysis allows extraction of the carrier mobility and comparison to the literature values. This point becomes critical when we compare the mobility in photoexcited and chemically doped cuprates in Chapter 5.

In this experiment, a GaAs surface is stimulated by 50 fs pulses of 815 nm light. Fig. 4.9(a) shows the THz time-traces transmitted through GaAs. The solid waveform shows the differential signal ($-\Delta E$) at 116 ps after photoexcitation and the dashed waveform shows the differential signal at 15 ps before photoexcitation. We measure the differential signal *before* photoexcitation to define a baseline for the measurement. Typically it contains a nonzero residue that is built up from previous pulses. The dotted waveform shows the transmitted THz waveform through the unexcited GaAs.

Fig. 4.9 shows the real and imaginary parts of the photoconductivity in GaAs. The solid curves

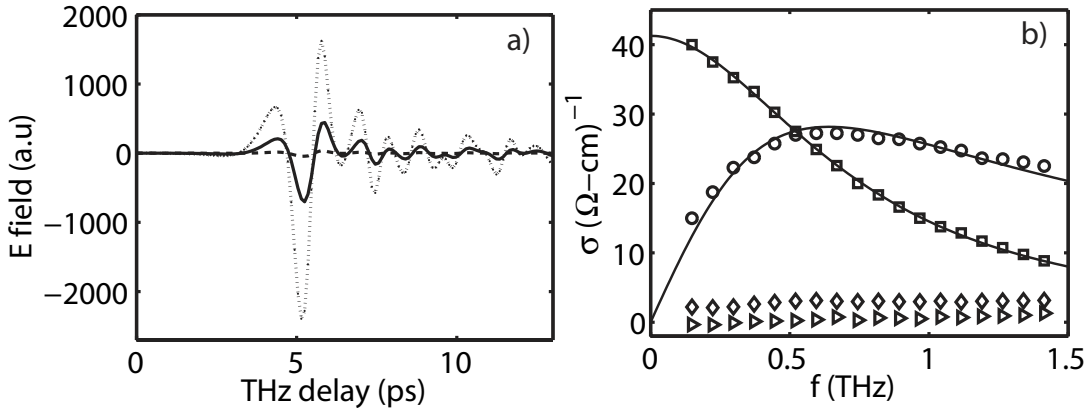

Figure 4.9: a) THz time-traces transmitted through GaAs. The solid waveform shows the differential signal ($-\Delta E$) at 116 ps after photoexcitation and the dashed waveform shows the differential signal at 15 ps before photoexcitation. The dotted waveform shows the transmitted THz waveform through the unexcited GaAs (E). b) Real (□) and imaginary (○) part of photoconductivity in GaAs at 116 ps after photoexcitation, together with the real (▷) and imaginary (◇) parts of photoconductivity at 15 ps before photoexcitation. The solid curves show the fits to the Drude model.

show the fits to the simple Drude model at 116 ps after photoexcitation. From the fits, we determine the Drude relaxation time $\tau = 250$ fs and DC resistivity $\rho_0 = 0.024\ \Omega - \text{cm}$. The square of plasma frequency (ω_p^2) is inversely proportional to the product of the relaxation time (τ) and resistivity (ρ) [17]:

$$\omega_p^2 = \frac{1}{\varepsilon_0 \rho \tau}, \tag{4.8}$$

where ε_0 is the permittivity of free space. For a spherical Fermi surface, the plasma frequency is related to the total density of carriers through

$$\omega_p = \left(\frac{n_c e^2}{m^* \varepsilon_0} \right)^{1/2}, \tag{4.9}$$

where n_c is the total carrier density, e is the electric charge, and m^* is the effective mass. We assume an equal density of electrons and holes, each with different effective mass, $m_e^* = 0.067 m_0$ for electrons and an average effective mass of $m_h^* = 0.47 m_0$ for holes [52]. Including both electron and hole contributions, we obtain

$$\omega_p^2 = \frac{n_e e^2}{m_e^* \varepsilon_0} + \frac{n_h e^2}{m_h^* \varepsilon_0} = \frac{n_{e,h} e^2}{\varepsilon_0} \left(\frac{1}{m_e^*} + \frac{1}{m_h^*} \right). \tag{4.10}$$

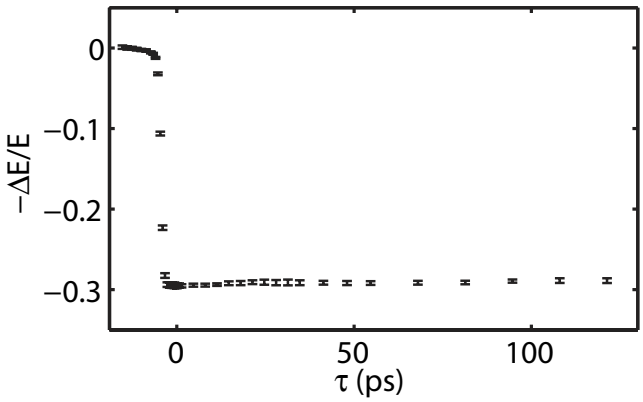

Figure 4.10: Room temperature fractional change $(-\Delta E/E)$ measured at the THz peak amplitude in photoexcited GaAs.

From Eq. 4.10, we estimate an electron-hole pair density of $n_{e,h} = 3.4 \times 10^{16}$ cm^{-3}. From the pump beam fluence (1.5 μJ/pulse) and photon energy (1.52 eV), we estimate a photoexcitation density of $n_{\text{ex}} = 6.2 \times 10^{16}$ cm^{-3}, with a penetration depth of 1 μm [53]. From the definition of the quantum efficiency:

$$\eta = \frac{\text{Number of generated electron-hole pairs}}{\text{Number of incident photons}} = \frac{n_{e,h}}{n_{\text{ph}}}, \tag{4.11}$$

we estimate a quantum efficiency of $\eta = 55\%$. Electron mobility can be determined according to $\mu_e = e\tau/m_e$. At 116 ps after photoexcitation, we estimate a room-temperature electron mobility of 6550 cm^2/V$\cdot$s. Using the same experimental technique, Beard *et al.* [51] reported a mobility of 6540 cm^2/V$\cdot$s at 100 ps after photoexcitation, with a photoexcitation density of $n_{\text{ex}} = 1.6 \times 10^{16}$ cm^{-3}. However, they used a generalized Drude model and neglected the contribution of induced holes in the plasma frequency [51]. At this doping range, the room-temperature Hall mobility of electron-doped GaAs is expected to be 5500$\pm$1500 cm^2/V$\cdot$s [54].

Figure 4.10 shows the time evolution of $(-\Delta E/E)$ at the THz peak as a function of pump-probe delay $\Delta\tau$ in GaAs, for $n_{\text{ex}} = 6.0 \times 10^{16}$ cm^{-3}. The decay of photocarriers occurs on a nanosecond timescale and is attributed to electron-hole recombination [51].

Chapter 5

Intrinsic photoconductivity of undoped cuprates

5.1 Purpose of this study

Cuprate high-temperature superconductors are often considered in terms of doping an antiferromagnetic insulator [55]. To understand them fully, then, it is important to understand the transport properties of dilute charge carriers in an antiferromagnetic insulating system. Yet even after two decades, such an understanding remains elusive. For example, the relative importance of magnetic and charge-lattice interactions in determining the DC mobility are not known, and various experimental approaches yield ambiguous results.

Photoconductivity measurements in the truly dilute limit have been restricted to the observation of the DC photoconductivity, which is sensitive primarily to long-lived impurity states [56]. In contrast, DC transport measurements on lightly doped compounds give surprisingly high carrier mobility that may be due to some form of cooperative transport [57]. Here, we create electrons and holes in undoped cuprates with a femtosecond laser pulse, and use a THz frequency probe pulse to directly measure the low-energy excitation spectrum of the photodoped material. Our picosecond time-resolved technique allows us to examine free electron-hole excitations before they relax, in order to determine the intrinsic mobility of the dilute carriers. We find that the decay dynamics of the transient photoconductivity bears a strong similarity to the spectral changes seen in visible-pump, visible-probe spectroscopy [58]. From this relationship, together with the temperature dependence of the photoconductivity, we conclude that the photocarriers exhibit hopping conductivity that is

limited by the availability of optically or thermally generated bosonic modes.

5.2 Background

A superconductor is a material with no resistance to the flow of electricity below a critical temperature T_c. The phenomenon was discovered by H. K. Onnes in mercury 100 years ago, soon after liquifying helium [59]. In the following decades, many elements and alloys were identified as superconductors. This new phenomenon was not understood until Bardeen, Cooper, and Schrieffer formulated the first microscopic theory of superconductivity (BCS) in 1957 [60]. Within this framework, superconductivity results from the condensation of electron pairs (Cooper pairs) into a coherent ground state. The pairing interaction is provided via electron-phonon coupling. The theory is successful in predicting many physical properties of the superconducting state, e.g. the Meissner effect, the isotope effect, the universal relationship between T_c and energy gap, and the exponential form of the low temperature specific heat. The theory was not challenged until the discovery of superconductivity in copper oxide ceramics (HTS or high-T_c or cuprates).

This new type of superconductor was discovered by Bednorz and Müller in 1986 after a systematic study of the electrical properties of ceramic compounds [61]. The first compound discovered was lanthanum copper oxide doped with barium, $La_{2-x}Ba_xCuO_{4+\delta}$ with a T_c of 29 K. Surprisingly, the undoped compound is an insulating ceramic and becomes a superconductor when doped. In the following year, Paul Chu and his colleagues synthesized $YBa_2Cu_3O_7$ with a critical temperature of around 93 K [62], exceeding the boiling point of liquid nitrogen. Tremendous advances were made in crystal chemistry and experimental techniques, and more high T_c compounds were found in quick succession. The current record belongs to the Tl-doped $HgBa_2Ca_2Cu_3O_{8+\delta}$ with $T_c \approx 138$ K at ambient pressure [63].

It was soon established that all these new compounds share two-dimensional CuO_2 planes. It is now believed that the strong correlation within these planes is responsible for many exotic properties of cuprate superconductors. After 25 years of intensive research, the superconductivity mechanism in cuprates is still controversial.

5.2.1 Phase diagram

High-T_c superconductors share a universal phase diagram. The undoped phase is antiferromagnetically ordered below the Néel temperature of about 250-500 K. $La_{2-x}Sr_xCuO_4$ is commonly considered as a prototype example of a hole-doped cuprate. As shown in the right side of Fig. 5.1,

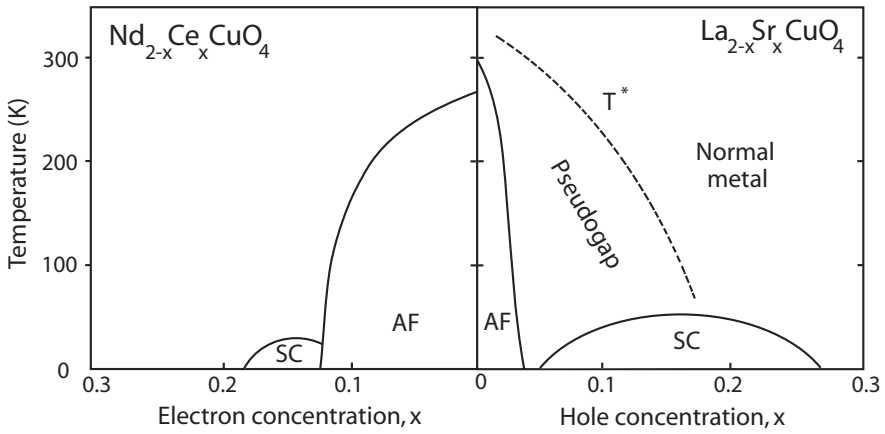

Figure 5.1: Schematic phase diagram of hole-doped (right) and electron-doped (left) cuprates; Adapted from Ref. [55].

introducing holes to the Cu-O plane rapidly suppresses the ordered state at 3-5% hole concentration. Almost immediately after the suppression of the ordered state, superconductivity emerges and persists up to 25% hole concentration. The generic dome-shaped phase of the superconducting state has a maximum T_c at an optimal doping of about 15% hole concentration. The region with doping x less than that of the maximum T_c is known as the underdoped region. In underdoped samples, the metallic state above T_c and below a temperature T^* exhibits many unusual properties and is referred to as the pseudogap. The nature of the pseudogap phase remains controversial, but it is common to associate it with the incomplete formation of the superconducting state well above T_c [64]. The region with doping x higher than that of the maximum T_c is called the overdoped region and exhibits normal metallic properties above T_c.

It is possible to dope these compounds with electrons rather than holes. A typical electron-doped system is $Nd_{2-x}Ce_xCuO_{4+\delta}$ (NCCO). As shown in the left side of Fig. 5.1, the phase diagram of electron-doped cuprates shows a more robust antiferromagnetism that persists to much higher doping, leaving a narrower superconductivity dome [65]. The pseudogap phase is not observed in the electron-doped cuprates.

5.2.2 Undoped cuprates

Undoped cuprates have an odd number of electrons in the conduction band and conventional band theory predicts them to be metals. The insulating character of the real materials arises from the

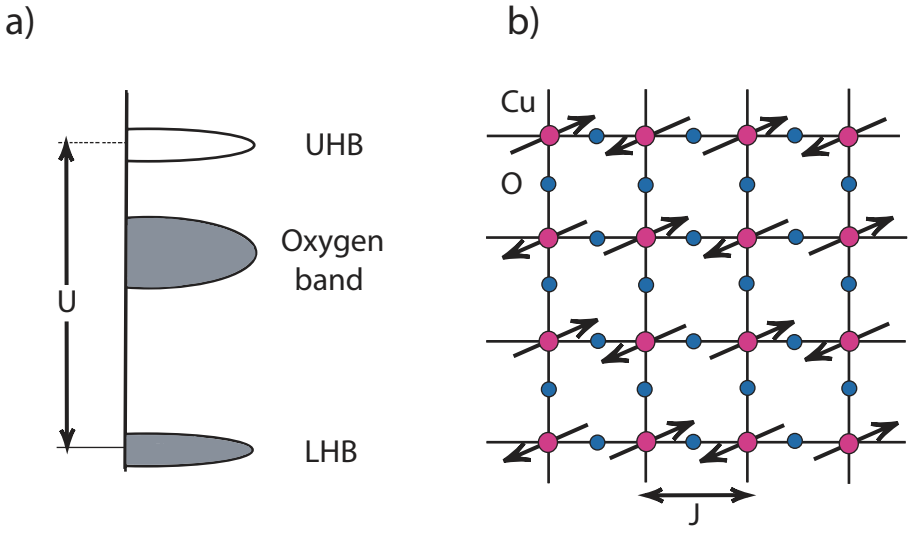

Figure 5.2: a) Schematic of the CuO_2 plane in undoped cuprates. The arrows indicate the spin alignment of the antiferromagnetic ground state. b) A schematic energy diagram of undoped cuprates. The copper electronic state is split into upper Hubbard band (UHB) and lower Hubbard band (LHB), separated by the gap energy U. The highest occupied band is about 1.5-2 eV below the UHB and is associated with oxygen $2p$ band.

anomalously strong electron-electron repulsion that imposes a high energy cost for double occupancy. The Coulomb energy, commonly denoted by U, dominates over the hopping energy t, and thus the ground state is insulating. Typical values of t and U are 300-500 meV and 8-10 eV, respectively [66, 67].

After double-ionization, the planar copper has a $3d^9$ configuration, so there is one unpaired electron per copper atom. For $U \gg t$, the copper state is split into the upper Hubbard band (UHB) and the lower Hubbard band (LHB), separated by the energy U as shown in Fig. 5.2(a). In this limit, superexchange produces an antiferromagnetic interaction between neighbouring sites with a typical exchange interaction J of 100-140 meV [67]. A schematic of the spin alignments in the CuO_2 plane is shown in Fig. 5.2(b). An anisotropic crystal field lifts the degeneracy of the copper d orbital so that the highest partially occupied orbital is $d_{x^2-y^2}$. As illustrated in Fig. 5.3(a), the $d_{x^2-y^2}$ orbital lobes point directly towards the p_σ orbitals of the four planar oxygens surrounding it and form strong covalent bonds with hopping integral t_{pd}. The oxygen valence orbitals $2p_{x,y}$ have a closed-shell configuration but the $d_{x^2-y^2}$ orbital has a single vacancy.

5.2.3 Charge-transfer excitation

The Cu-O charge transfer energy $\Delta = \varepsilon_p - \varepsilon_d$ is smaller than the on-site Hubbard U, so these compounds are called charge transfer (CT) insulators. The optical gap of a CT insulator corresponds to the transfer of an electron from an oxygen ion to a vacant state on a neighboring transition metal ion. When $\Delta > U$, the optical gap corresponds to the electron transfer directly between two neighboring transition metal ions, and the material is called a Mott insulator. The charge transfer character of the insulating gap in cuprates has been confirmed by electron energy loss spectroscopy (EELS) [69]. A schematic of the CT process is illustrated in Fig. 5.3(b). The CT gap manifests itself as a pronounced peak at 1.5-2 eV in the in-plane optical conductivity spectra of copper oxides [68]. The optical conductivity spectra of some 1D and 2D insulating cuprates are illustrated in Fig. 5.3(c).

In undoped cuprates, the optical conductivity spectrum above the gap edge is dominated by two peaks [70, 68]: the low energy peak corresponds to an electron transfer from an O-$2p_\sigma$ orbital to a Cu-$3d_{x^2-y^2}$ orbital, while the higher energy peak corresponds to an electron transfer from an O-$2p_\pi$ orbital to a Cu-$3d_{x^2-y^2}$ orbital. In the low energy peak, the hole created at the $2p_\sigma$ hybridizes with three other neighbour oxygen orbitals, as shown with a dashed circle in Fig. 5.3(a). The combined state of four oxygen hole states and the central $3d_{x^2-y^2}$ electron state form a spin singlet state, known as Zhang-Rice singlet (ZRS). It has been shown that this singlet state corresponds to the lowest energy excitation for an undoped cuprate [71] and can move with little disturbance to the antiferromagnetic background. In the higher energy peak, the hole in the O-$2p_\pi$ orbital also hybridizes with neigbouring O-$2p_\pi$ orbitals in a nonbonding state that has little hybridization with the central Cu-$3d_{x^2-y^2}$ orbital.

5.3 Bosonic excitations

One essential question concerning the physics of high temperature superconductors is the contribution of phonons in modulating electronic and magnetic interactions in these compounds. ARPES provides evidence for the importance of phonons in lightly doped cuprates. Lanzara *et al.* reported a ubiquitous anomaly (kink) in the dispersion relation around 50-80 meV along (0,0)-(π,π) direction in various copper-oxide superconductors. The kink corresponds to a sharp change in the velocity and scattering rate near the phonon energies. The feature appears to be more pronounced in the underdoped regions and persists to well above the transition temperature T_c [72]. In undoped cuprates,

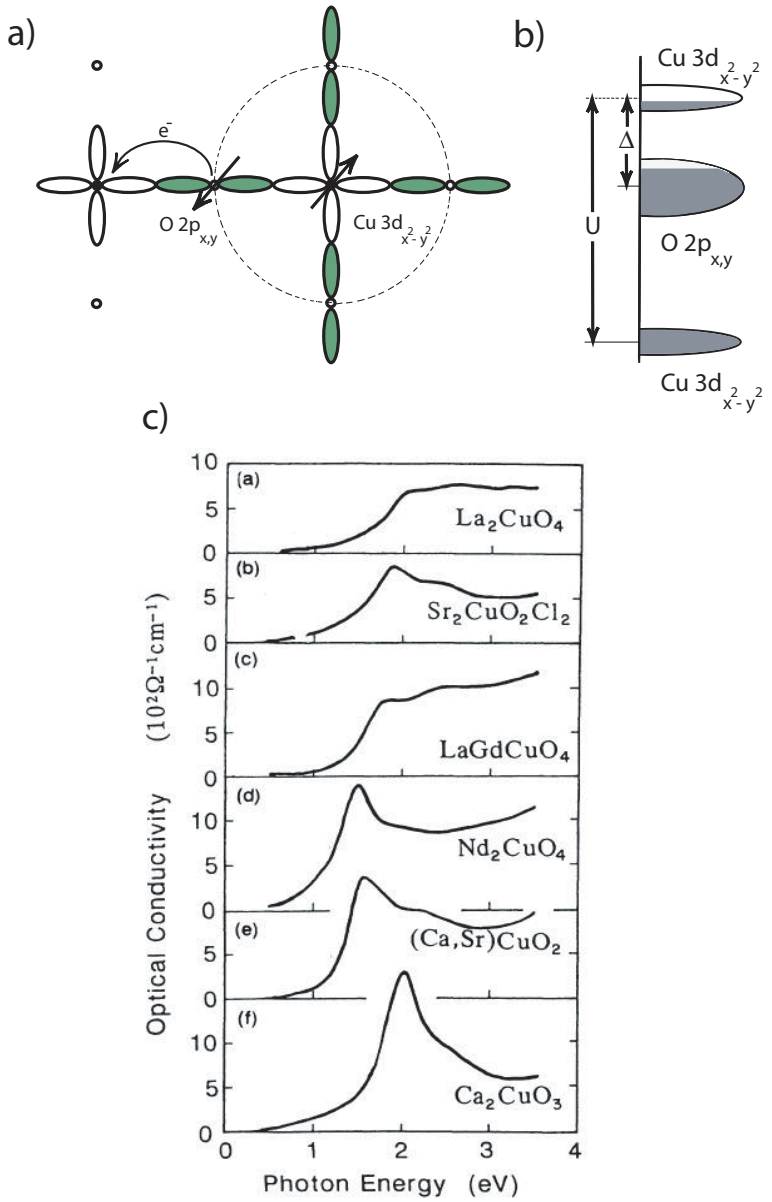

Figure 5.3: a) A sketch of the charge-transfer excitation in CuO_2 plane. The combined state of four oxygen hole state and the central $3d_{x^2-y^2}$ electron state forms a spin singlet state. The dashed circle denotes a Zhang-Rice singlet. b) A schematic energy diagram of charge-transfer bands in the hole picture. c) Optical conductivity spectra of parent 1D and 2D copper-oxide compounds. The electric field is parallel to the copper-oxide basal plane. From Tokura *et al* [68]; used by permission.

ARPES spectra reveals a considerable broadening of the lineshape that is interpreted as a Franck-Condon type process [73, 74]. Viewed in this way, the generated photoholes are strongly coupled to the bosonic modes that modulate the electronic interactions in the system.

Another indication of polaron formation arises from measurements of the dielectric constant in La_2CuO_4 [75, 76]. Chen *et al.* estimated a static dielectric constant of $\varepsilon_s = 31 \pm 2$ for the electric field perpendicular to the CuO_2 plane, considerably higher than the optical-frequency dielectric constant of $\varepsilon_\infty = 5$. The large difference between ε_s and ε_∞ indicates a large contribution from optical phonons in the static polarization and leads to a strong coupling between carriers and phonons, as expressed by the Fröhlich coupling constant [77, 78]

$$\alpha_F = \frac{e^2}{4\hbar\omega_0}\left(\frac{1}{\varepsilon_\infty} - \frac{1}{\varepsilon_s}\right)\left(\frac{2m^*\omega_0}{\hbar}\right)^{1/2}, \tag{5.1}$$

where ω_0 denotes the optical phonon frequency. Using $m^* = 4m_0$ [79] and $\hbar\omega_0 = 43$ meV [80], we find a coupling constant of $\alpha_F \sim 5.8$ which puts the polarons in La_2CuO_4 in the intermediate coupling region ($3 \leq \alpha_F \leq 6$).

The strong temperature dependence of the CT excitation also provides evidence for polaronic behaviour at near zero doping. Upon raising the temperature, the CT peak exhibits a broadening and a shift to lower energies [80, 70]. Falck *et al.* proposed a model based on short range electron-hole attraction and carrier-phonon interaction to explain the strong temperature dependence of the peak in the imaginary part of the dielectric function (ε_2) at 2.25 eV [80]. From the fits to the data, they estimated an average phonon energy of 43 ± 4 meV as the only adjustable parameter.

Dodge *et al.* [58] demonstrated the role of bosons in determining the optical pump-probe properties of the CT excitation. They used a visible-pump, visible-probe technique to measure the transient change in the optical transmission spectrum of $Sr_2CuO_2Cl_2$ after pumping with 2.1 and 3.1 eV photons. They observed a photoinduced softening and shift of CT gap to lower energies, shown in Fig. 5.4(a), that resembles the effect of raising temperature. The similarity in energy position and spectral shape between heating and photoexcitation suggests that they result from the same underlying mechanism. The temperature dependence of CT excitation corresponds to the change in Bose-Einstein occupation of a bosonic mode with an energy of 43 ± 4 meV [80]. Note that this bosonic mode could be related to the phonons or spin fluctuations or a combination of the two. Dodge *et al.* related the pump-induced signal to the differential linear absorption, $\alpha(15\text{ K}) - \alpha(250\text{ K})$, and estimated that each 3.1 eV photon creates from eleven to twenty bosons with energies ranging from 70 to 130 meV. They argued that these non-thermal bosons decay anharmonically into acoustic phonons on a picosecond timescale, and that this process governs the temporal decay of the pump-probe

signal.

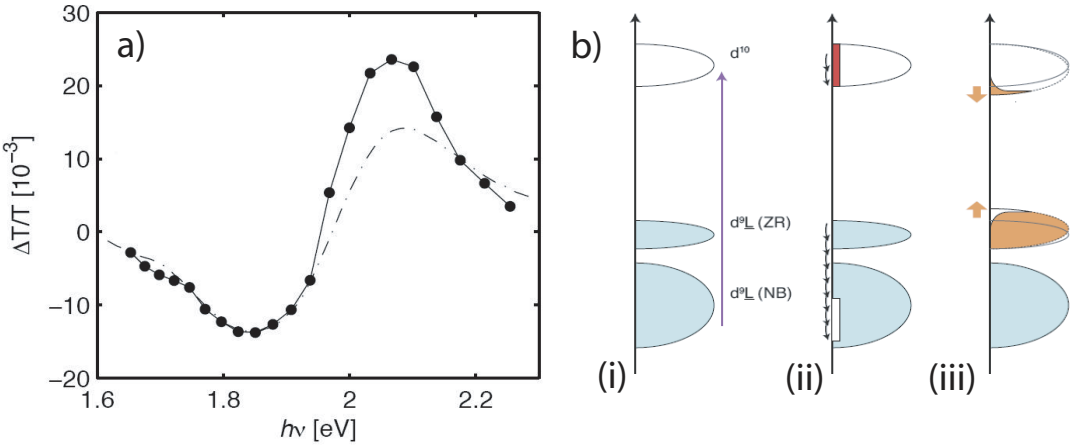

Figure 5.4: a) Comparison between the change in optical transmission spectrum due to photoexcitation and heating in $Sr_2CuO_2Cl_2$. The solid line represents the transient photoinduced change after pumping with 3.1 eV photons at 15 K and the dashed line represents the differential linear absorption from 15 to 250 K. b) An illustration of the photoexcitation event sequence: i) absorption of a 3.1 V photon. ii) hot carrier decay to the gap edge through a boson cascade. iii) hot bosons broaden and shift the CT gap to lower energies. From Dodge *et al.* [58]; used with permission.

The event sequence of this process is illustrated in Fig. 5.4(b). It begins with the absorption of a 3.1 eV photon followed by initial relaxation of the photoexcited state by successive emission of bosons in tens of femtoseconds. These hot bosons produce a softening of the CT gap that broadens the optical gap excitation and shifts it to lower energies. As time evolves, the photoinduced absorption signal decays as the nonequilibrium boson population thermalizes. This proposed model closely resembles the relaxation process in photoexcited polar semiconductors [77].

5.4 Mobility of dilute carriers

ARPES shows quasiparticle (QP) peaks in the superconducting state of optimally and underdoped cuprates, indicating the coherent motion of photoexcited carriers [81]. When the Mott transition is approached, the QP peak is replaced by a broad feature at the gap edge that has been attributed to a phonon sideband [73, 74], indicating strong coupling to bosonic shake-off modes. In this limit, one would consider these as polaronic excitations that are effectively localized.

Thio *et al.* [56] carried out the first DC photoconductivity measurement on insulating cuprate La_2CuO_4 and reported a very slow decay of ~ 10 s at room temperature. Using this slow decay,

they estimated a mobility of $\eta\mu \approx 10^{-7}$ cm^2/V$\cdot$s, where η is the quantum efficiency for producing free carriers per photon. This very small value of $\eta\mu$ could either arise from a small value of η or a very low average mobility. The first case is unlikely since the 2.2-eV pump energy is well above interband absorption threshold. The more likely case is that the low average mobility results from the localization of photocarriers. Considering the low mobility and very slow relaxation time, it was argued that the photocarriers are trapped at defect sites, so this measurement does not yield any useful information about the intrinsic charge transport of dilute carriers.

An in-plane transport measurement on very lightly doped $La_{2-x}Sr_xCuO_4$ was carried out by Ando *et al.* [57]. Upon doping, they observed a Hall mobility with a value of 3 cm^2/V$\cdot$s in $La_{1.99}Sr_{.01}CuO_4$. The magnitude of the mobility is relatively high for an oxide and comparable to those of typical metals at room temperature. It was argued that the surprisingly high value of mobility and its doping insensitivity could be an indication of phase segregation on a mesoscopic scale. In this picture, charge carriers tend to aggregate in self-organized regions of high density and relatively high mobility.

Given the high Hall mobility, low photoconducting drift mobility, and evidence for strong electron-boson effects in ARPES, there is ambiguity over the nature of the photoexcited state in very lightly doped cuprates. We attempt to understand the transport properties of photoexcitations in the undoped cuprates $Sr_2CuO_2Cl_2$ (SCOC), $YBa_2Cu_3O_6$ (YBCO), and La_2CuO_4 (LCO) using a visible pump, THz-probe technique. The technique provides the necessary time resolution to examine the intrinsic photoconductivity of the CT states. Moreover, the THz-frequency probe pulse is primarily sensitive to the movement of free charges. Using this technique, we estimate the mobility of photoexcited carriers in their initial state after photoexcitation. The technique has already proven successful in determining the mobility of photoexcited states in systems such as GaAs and TiO_2 [51, 82].

5.5 Samples

In our experiment, we photoexcite insulating single crystals of SCOC, YBCO, and a thin film of LCO. These compounds have the same electronic configuration in the CuO_2 plane and comparable interaction energies t, J and U [83, 67]. Here I provide a brief description of the crystal structure and growth technique of each sample.

LCO is the parent compound of prototypical $La_{2-x}Sr_xCuO_4$. The ground state is an antiferromagnetic insulator with a Néel temperature of 325 K [84]. The material exhibits superconductivity

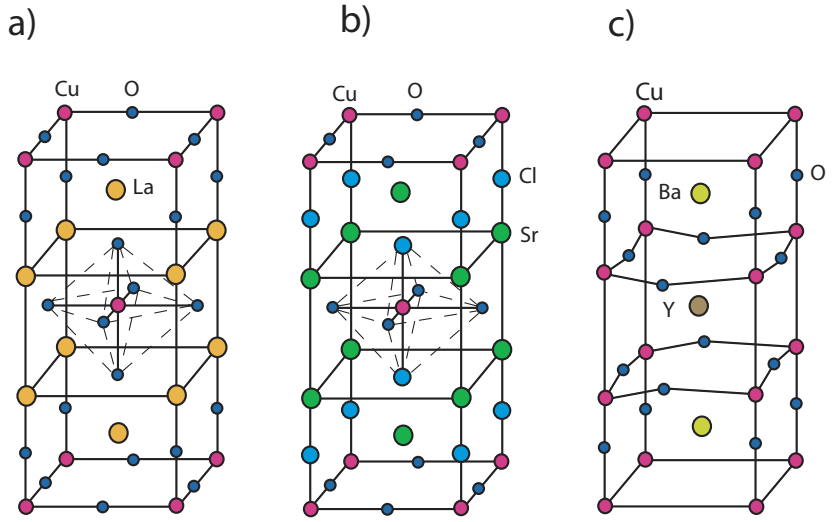

Figure 5.5: Crystal structure of a) La_2CuO_4, b) $Sr_2CuO_2Cl_2$ and c) $YBa_2Cu_3O_6$.

when doped with an alkaline earth element, typically by partial substitution of divalent Sr for trivalent La. The crystal structure is shown in Fig. 5.5(a). In LCO, corner sharing CuO_6 octahedra form a two-dimensional square lattice stacked along the c-axis with intervening La atoms [61].

We attempted to measure an LCO single crystal obtained from Graeme Luke's group at McMaster University. The sample was polished and thinned to a thickness of about 200 μm but it was not transparent in the THz region even at low temperatures. The lack of transmission could be related to a high impurity content. Subsequently, we were successful with measurements on an 80 nm LCO film. We note that the LCO skin depth for 3.1 eV photons is around 160 nm [85] and thus, the photoexcited region is fairly uniform throughout the entire 80 nm film thickness. The LCO film was deposited by molecular beam epitaxy on a 10×10 mm^2 MgO substrate and was synthesized by Ivan Bozovic at Brookhaven National Laboratory.

SCOC is an antiferromagnetic insulator with a Néel temperature of 256 K [86]. The crystal structure of SCOC is illustrated in Fig. 5.5(b). The material is isostructural to the high temperature phase of LCO, with the apical oxygens replaced by chlorine and lanthanum by strontium. SCOC is a nearly ideal two-dimensional antiferromagnetic system as it is stochiometrically stable and grows exactly at zero doping with minimum disorder [86]. Superconductivity is achieved by partial substitution of oxygens for apical chlorine under high pressure. $Sr_2CuO_{2+\delta}Cl_{2-y}$ yields a T_c of 30 K at $y = 0.8$ [87]. Alternatively, the analogous compound $Ca_2CuO_2Cl_2$ can be doped by partial substitution of Na for Ca and produces a T_c of 28 K at 18% hole concentration [88].

SCOC crystals were synthesized by Ruixing Liang at the University of British Columbia. They were grown by cooling the melt from 1110°C to 1075°C at a rate of 3°C/hr in an alumina crucible [89].

YBCO is the parent compound of superconducting $YBa_2Cu_3O_{6+x}$ ($x \approx 6.5-7.5$), the first material to exhibit superconductivity above the boiling point of nitrogen. It belongs to the class of bilayer materials, since there are two distinct CuO_2 layers per unit cell. The CuO_2 distortion appears as a shift of oxygen ions toward the interior of the bilayer as shown in Fig. 5.5(c). The undoped regime exhibits antiferromagnetic ordering below a Néel temperature of about 500 K. The parent compound can either be doped by partial substitution of Y^{3+} for Ca^{2+} [90] or by adjusting the oxygen content by proper heat treatment [91]. The optimally doped $YBa_2Cu_3O_{6.95}$ yields a maximum T_c of 93 K. The YBCO crystal used in this work was fabricated by a top-seeded melt growth technique [92]. An oxygen content of 6.00-6.01 was achieved by annealing at 700°C under 5×10^{-7} torr oxygen pressure for 10 days. The YBCO crystal was synthesized by Ruixing Liang at the University of British Columbia.

5.6 Results

5.6.1 Photoconductivity spectra

The room temperature photoconductivity spectra of SCOC, YBCO, and LCO are shown in Fig. 5.6. The measurements are performed at optical fluences equivalent to 0.015, 0.016, and 0.012 photoexcitations per unit cell, respectively. The photoexcitation density is different for each compound owing to differences in penetration depth, pump-beam area, and unit cell size. The procedure for determining the photoexcitation density is provided in Appendix E. Two key features of σ_1 are immediately apparent. First, the lines extrapolate to a nonzero σ_1 at DC, indicating the presence of free and mobile carriers. Second, we do not observe any dispersion within our experimental uncertainty, and this remains true as the photoconductivity decays with time. Fitting the SCOC data at 1.3 ps to an even polynomial expansion about $\omega = 0$ gives a curvature of $0.05 \pm 0.10\ \omega^{-1}\mathrm{cm}^{-1}/\mathrm{THz}^2$, so that within our experimental uncertainly, there is no dispersion. Clearly, significant spectral content must lie at higher frequencies. The expected increase in spectral weight can be calculated according to the f-sum rule [93],

$$\frac{n_c(\Omega)e^2}{m^*} = \frac{2}{\pi}\int_0^{\Omega} \sigma_1(\omega)d\omega. \tag{5.2}$$

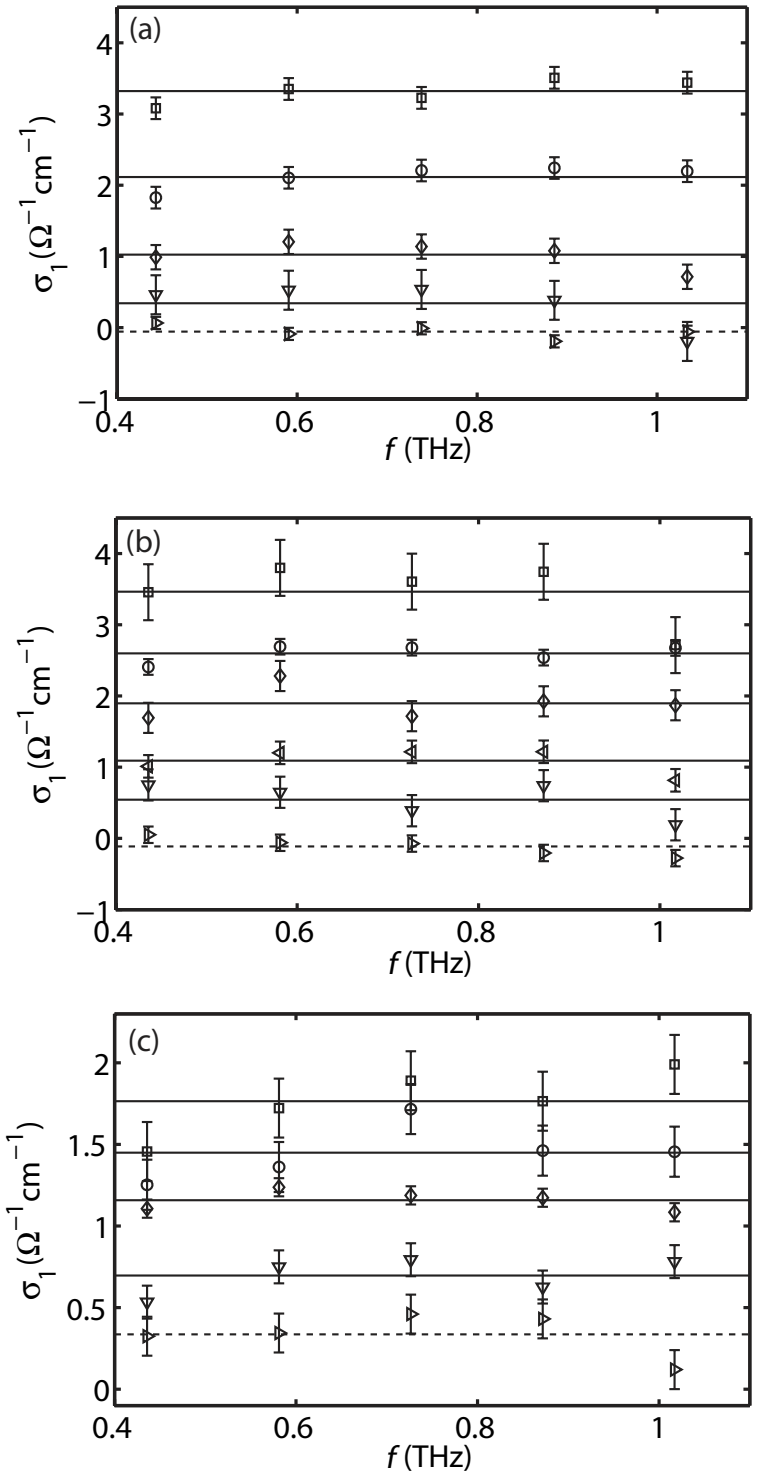

Figure 5.6: a) Room temperature photoconductivity of SCOC at 1.3 (□), 4 (○), 16 (◇), 75 (▽), and -15 (▷) ps after photoexcitation. b) Room temperature photoconductivity of YBCO at 0 (□), 0.7 (○), 3.3 (◇), 8.7 (◁), 79 (▽), and -15 (▷) ps after photoexcitation. c) Room temperature photoconductivity of LCO at 1.3(□), 4 (○), 15 (◇), 80 (▽), and -15 (▷) ps after photoexcitation.

In addition to hole transport, we consider an equal contribution from photoexcited electrons because of their similar mobility in the lightly electron-doped cuprates [94, 57]. In SCOC, using $n_c = 1.2 \times 10^{20}$ cm^{-3} and $m^* = 4m_0$ [79], only 0.2% of the expected increase in spectral weight after photoexcitation is accounted for by the conductivity seen within our experimental bandwidth. This means that even though mobile carriers are being created, they must be strongly renormalized by interaction with a characteristic energy scale that lies well above our measurement bandwidth. We also simultaneously measure the imaginary part of conductivity to be zero within ± 0.9 $(\Omega\,\mathrm{cm})^{-1}$. The imaginary parts of conductivity are shown in Appendix F.

As described in Appendix E, we can estimate the free-carrier mobility μ from $\sigma \backsimeq 2\eta n_{\mathrm{ex}} q_e \mu$, where η is the quantum efficiency for free carrier production, n_c is the excitation density, and q_e is the electric charge. The quantum efficiency for the creation of unbound excitations is unknown, so our measurements give the product of mobility and quantum efficiency $\eta\mu$. In SCOC, at +1.3 ps after photoexcitation, the extrapolated DC conductivity corresponds to charge transport with an $\eta\mu$ of 0.15 ± 0.05 cm^2/V$\cdot$s, where the dominant uncertainty is the variation from sample to sample. The estimated values of $\eta\mu$ at 1.3 ps after photoexcitation is listed in Table 5.1 for all compounds studied. We expect the quantum efficiency η to be close to unity since the 3.04 eV pump energy is well above the optical absorption threshold for these compounds. It should be noted that the photo-

Table 5.1: Room temperature $\eta\mu$ at 1.3 ps after photoexcitation.

	SCOC	YBCO	LCO
$x(\%)$	1.5	1.6	1.2
$\eta\mu$(cm^2/V$\cdot$s)	0.15	0.07	0.03

induced change in LCO is 4 times smaller than SCOC, resulting in lower SNR and data quality compared to SCOC and YBCO. This is partially due to the 80 nm film thickness, which is half of the 160 nm penetration depth in this compound [85]. The LCO photoconductivity spectrum is the result of averaging 200 2D scans, equivalent to two days of data collection.

5.6.2 Relaxation dynamics

Because $\sigma_1(\omega)$ is non-dispersive within our bandwidth, measuring the change in the peak THz amplitude with time is sufficient to characterize the decay dynamics. Figure 5.7(a) shows the time evolution of $-\Delta E/E$ as a function of pump-probe delay ($\Delta\tau$) in SCOC. We observe a rapid onset of photoconductivity followed by a non-exponential decay that we fit using a double-exponential

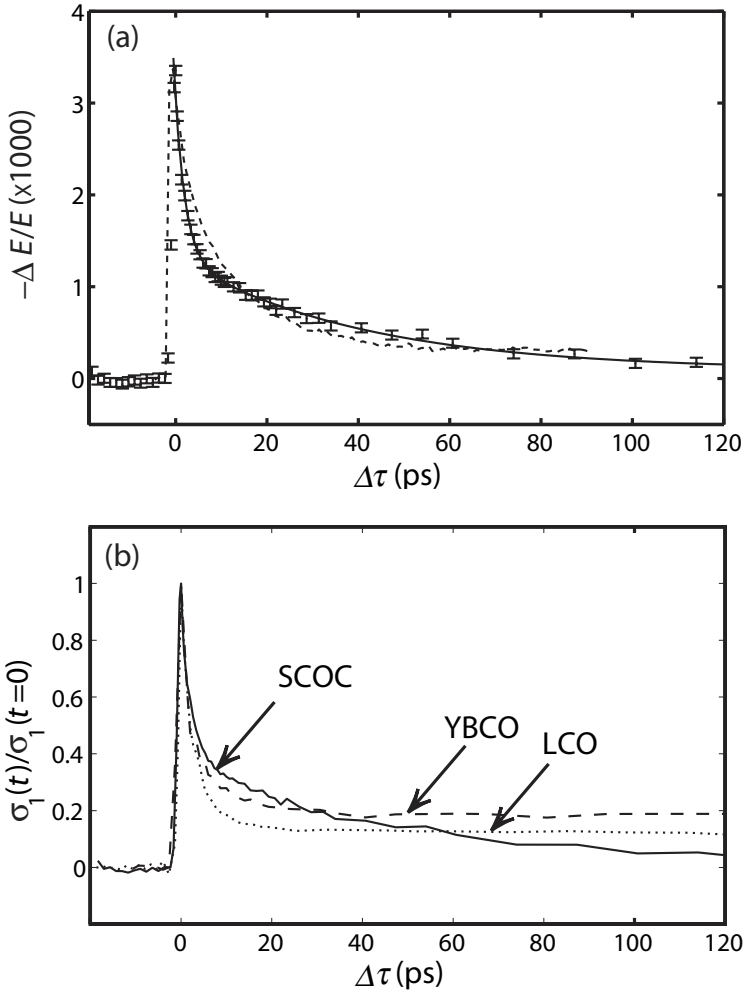

Figure 5.7: Room temperature fractional change -$\Delta E/E$ in the THz transmission amplitude through SCOC after photoexcitation, measured at the peak of the THz pulse. The solid line is a fit to a double exponential decay to a constant, as described in the text. Errorbars indicate the statistical variability in the measured value at each point. The dashed line is the experimental data of Dodge *et al*. [58] for the change in total optical transmission in a visible-pump, visible-probe experiment. b) Normalized decay dynamics in SCOC (solid line), YBCO (dashed line), and LCO (dotted line) at room temperature.

decay to a constant, with exponential time constants of 2 and 40 ps. From the change at the THz peak, we estimate a spectrally averaged $\eta\mu$ of 0.22 $cm^2/V \cdot s$ at peak fluence, corresponding to 1.5% photoexcitations per unit cell. Similarly, we obtain exponential time constants of 0.6 and 7 ps at a fluence of 1.6% in YBCO and exponential time constants of 0.9 and 4 ps at peak fluence of 1.2% in LCO.

We compare the change in THz conductivity and optical transmission seen in a visible-pump, visible-probe measurement in Fig. 5.7(a), and the agreement between the two is striking.[1] In the visible-pump, visible-probe measurements [58], the change in optical transmission was related to bosonic modes that couple strongly to the charge-transfer excitations. The agreement between the decay rates seen in the two techniques suggests that the non-thermal phonon population contributes to DC transport, and that the time dependence of the photoconductivity is dominated by changes in the mobility, not the carrier concentration.

The normalized decay dynamics of all studied compounds are shown in Fig. 5.7(b). At 1.3 ps after photoexcitation, we estimate a spectrally averaged $\eta\mu$ of 0.07 and 0.03 $cm^2/V \cdot s$ in YBCO and LCO, respectively. The qualitative agreement among the values for $\eta\mu$ and the similarity of the decay dynamics across three different compounds indicate that the observed picosecond photoconductivity is an intrinsic feature of the copper oxide plane.

The temperature dependence of the decay dynamics in SCOC and YBCO is shown in Fig. 5.8(a). The fitted exponential time constants are relatively temperature-independent, but the residual conductivity that remains after several picoseconds increases strongly with increasing temperature. As shown in the inset of Fig. 5.8(b), the peak conductivity is nearly temperature-independent. Fig. 5.8(c) show semilogarithmic plots of $T\sigma_r(T)$ versus $1/T$. The linearity of the data at high temperature is consistent with the form expected from Holstein's model of adiabatic polaron hopping, $\sigma = (\alpha/T)\exp(-E_a/k_BT)$ [95]. In SCOC and YBCO, the fits over the linear region give activation energies E_a of 17 and 25 meV, which compares favorably with the phonon energy range of 20-70 meV in these compounds [96, 97].

At this point, we are only certain that the residual conductivity increases with increasing temperature and this implies some form of hopping conduction, in contrast to coherent band transport. We should acknowledge that the conductivity model is not unique and there are other ways of fitting to the data. For example, the data can also be described by the conductivity of the variable-range hopping (VRH) form $\sigma \sim \exp[-(T_0/T)^{1/4}]$, which describes the the carrier transport in disordered

[1] Optical transmission measurements give the reduction in transmitted power or intensity I. But for small changes, $\Delta I/I \approx 2\Delta E/E$, so the time dependence of dynamical processes can be compared directly between the two techniques.

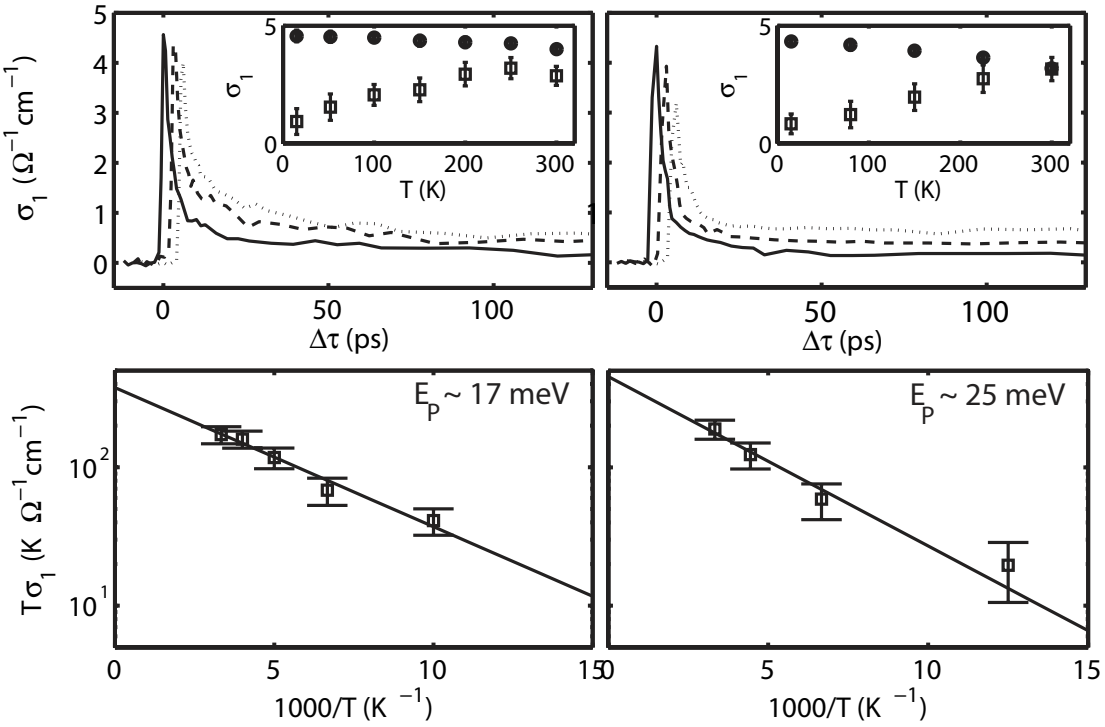

Figure 5.8: a) Decay dynamics at 15 K (solid lines), 150 K (dashed lines) and 300 K (dotted lines) in SCOC (left) and YBCO (right). The decay dynamics are shifted by 3 ps for clarity. SCOC and YBCO measurements are performed at hole densities of $6 \times 10^{19}\ cm^{-3}$ and $9 \times 10^{19}\ cm^{-3}$ equivalent to 0.015 and 0.016 holes per unit cell, respectively. Inset: Temperature dependence of the peak conductivity (•) along with the 5-times magnified residual conductivity (□) in SCOC (left) and YBCO (right). b) semilogarithmic plots of the temperature-dependent residual conductivity in SCOC (left) and YBCO (right). Residual conductivity is defined as averaged conductivity of the decay tail above 100 ps. Error bars indicate statistical variability at each point.

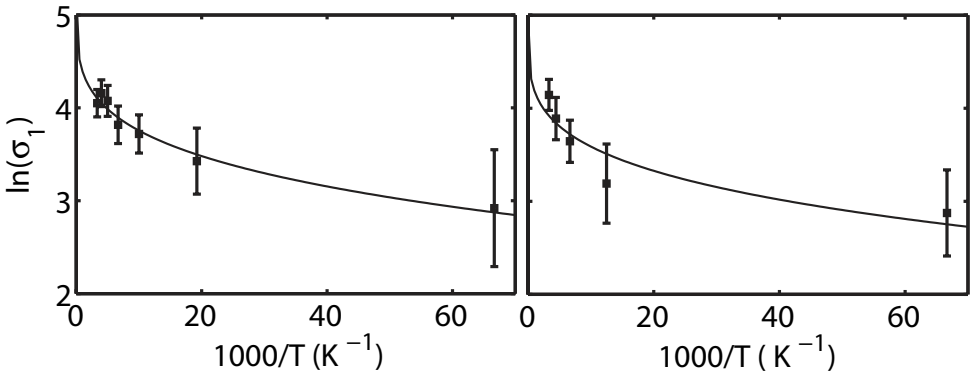

Figure 5.9: Arrhenius plots of the temperature-dependent residual conductivity and the VRH fits in SCOC (left) and YBCO (right).

systems [17]. In this model, the available sites are not equally spaced, so there is a trade off between the tunneling ($\propto \exp(-2R/\xi)$) and activation probability ($\propto \exp(-E_a/k_BT)$), where the R is the hopping length and ξ is the localization length. This model is also used to describes the low-temperature conduction in the insulating phase of cuprates [98]. In SCOC and YBCO, the fits yield a T_0 value of 580 and 1400 K, respectively. The is comparable to the value estimated by Ellman *et al*. [98]. From the low-temperature resistivity of $La_{2-x}Sr_xCuO_4$ at x=0.05, they estimated $T_0 = 645$ K. In the variable range hopping model, the T_0 parameter relates to the average energy spacing within a localization volume, and is usually much higher than what we obtain from our measurements. The Arrhenius plots of the temperature-dependent residual conductivity and the VRH fits to the data are shown in Fig. 5.9. In contrast to the Holstein's fit, the VRH fits captures both the low and high temperature points at the cost of some deviations at higher temperatures.

5.6.3 Doping dependence

Doping levels can be easily varied by adjusting the pump fluence from 20 to 250 $\mathrm{mW/cm^2}$, equivalent to hole concentration of 0.002 and 0.016 per unit cell in SCOC. At each fluence, we measure the fractional change in the peak THz amplitude $\Delta E/E$ as a function of pump-probe delay $\Delta\tau$. This enables us to study the doping dependence of the peak mobility and the decay dynamics. The decay dynamics in both SCOC and YBCO are independent of hole concentration over a range of 0.2 to 1.6%. The peak mobilities of photodoped carriers in SCOC and YBCO are shown in Fig. 5.10 together with Hall mobility of chemically doped $La_{2-x}Sr_xCuO_4$ [57]. In the photoexcited state, we observe that the inferred mobility decreases weakly with doping, and appears to stabilize at $\eta\mu$

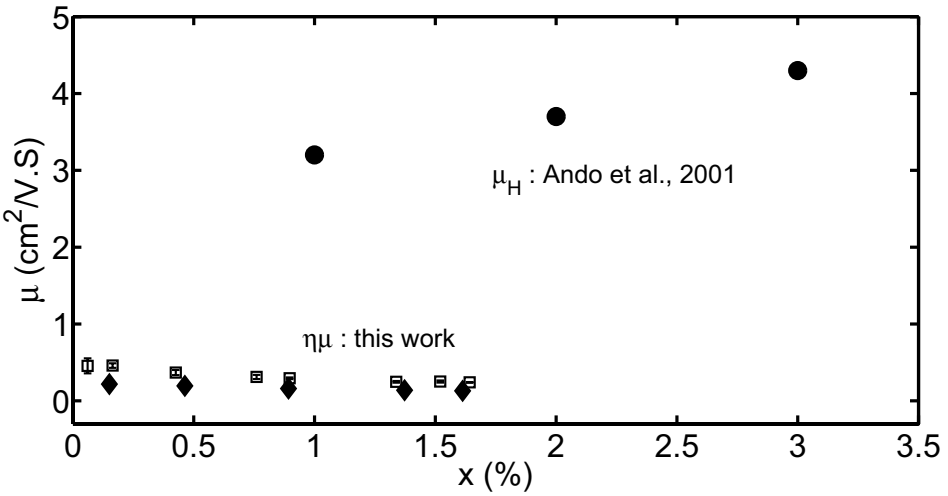

Figure 5.10: Evolution of mobility with carrier concentration. DC mobility of photocarriers in SCOC (□) and YBCO (⧫), inferred from $(\Delta E/E)_{\text{peak}}$. Hole mobility (•) in chemically-doped $La_{2-x}Sr_xCuO_4$, from Hall-effect data reported by Ando et al. [57]. These measurements are performed at the effective doping range before the superconductivity emerges at 5% doping.

values of 0.22 and 0.15 $\text{cm}^2/\text{V}\cdot\text{s}$ in SCOC and YBCO, respectively. We should emphasize that the inferred mobilities are lower than the Hall mobility in $La_{2-x}Sr_xCuO_4$ with similar carrier concentration. This is significant, especially because in other systems such as GaAs and TiO_2, similar measurements give a $\eta\mu$ value consistent with the Hall mobility [51, 82]. In Chapter 3, we showed that our spectrometer is capable of accurately measuring the electron mobility in GaAs . Even if we use the estimated quantum efficiency of $\eta = 0.55$ in GaAs, the mobilities in undoped cuprates are still lower than those of chemically doped systems.

5.7 Conclusion

The suppressed mobility compared to the Hall value, and the fact that most photocarrier spectral weight must lie at energies well above a few meV, indicate that the electrons and holes created by photoexcitation are inhibited against long-range transport. From the $Sr_2CuO_2Cl_2$ mobility at 1.3 ps after photoexcitation, we estimate a mean scattering time of $\tau \sim 0.3$ fs. Using the Fermi wave number $k_F \sim 0.62\ \text{Å}^{-1}$ [99], we estimate a mean free path of $l \sim 0.6\ \text{Å}$, smaller than the lattice constant in the Cu-O plane. The time scale for the mobility to decay is too short for the carriers to move very far, so they are unable to aggregate as Ando *et al.* have suggested occurs in doped

compounds. In this picture, the chemically doped compounds have higher mobility because of this screening effect.

Although excitons may be expected to form from photoexcitations near zero doping, the large exciton peak linewidth implies a short timescale for exciton decay and therefore cannot explain the conductivity decay dynamics that we observe [100, 101].

We conclude that the most natural explanation for all these effects is that the photocarriers immediately form small polarons. Immediately after photoexcitation, the excess bosons provide the necessary activation energy to yield the nonzero DC conductivity revealed by the THz spectra. As these bosons decay, the mobility is lost. Because the mobility is low and lasts only briefly, the photocarriers are unable to interact with one another and there is no enhancement of mobility with increased photodoping. In contrast, in chemically doped systems σ_1 is concentrated at low energies, the mobility is higher, and the mobility increases as a function of doping. The contrast between the two cases supports the view that lightly doped cuprates are characterized by a type of electronic phase separation that enhances the screening of the lattice polarization and consequently increases the mobility above the value it would have in a homogeneous system. [57].

Chapter 6

Future directions

In this thesis, I described the application of THz spectroscopy to two physical systems, metallic $Cr_{1-x}V_x$ alloys and insulating cuprates. In the first system, we use THz time-domain spectroscopy (THz-TDS) to determine the plasma frequency of $Cr_{1-x}V_x$ thin films, as the system undergoes a Fermi surface instability. In the second system, we use visible-pump, THz-probe spectroscopy to determine the drift mobility of photoexcited insulating cuprates. In the following, I discuss a selection of ideas that has emerged during the course of this work to improve the quality of measurements. Moreover, I outline further applications of our spectrometers to other physical systems.

6.1 THz time-domain spectrometer

The followings are steps that can be taken to improve the spectrometer.

• In Chapter 4, we presented the resistivity and relaxation time values for $Cr_{1-x}V_x$ thin films over the temperature range of 35-300 K. Below 30 K, the optical path length through the cryostat changes as α/T, where T is the temperature inside the cryostat and $\alpha = 2570$ fs. This results in a systematic uncertainty in our optical thickness measurements that results from small temperature fluctuations. We initially suspected that the $1/T$ behavior may either arise from oxygen in the cryostat vacuum jacket or THz window material (mylar). Despite a systematic investigation by Graham Lea, a former member of our group, the source of this issue is not resolved [102].

• To reduce contributions to the time-domain jitter from low-frequency temperature fluctuations, we can implement a faster THz scan rate. This requires a faster delay stage and a faster acquisition lock-in amplifier.

• We currently use silicon-on-sapphire photoconductive antennas to generate and detect THz pulses.

Our group is planning to fabricate LT-GaAs antennas which can extend the bandwidth up to 3 THz.

6.2 Chromium vanadium project

We observe a series of disagreements at low temperatures in the plasma frequency estimates between the THz-TDS and Hall technique. A theoretical framework is required to explain these disagreements. We plan to perform similar measurements on less disordered alloys that undergo a quantum phase transition. This should further clarify the role of Fermi surface and disorder in the low-temperature disagreements in $Cr_{1-x}V_x$ alloys. Our group is planning to study thin film samples of palladium-nickel (PdNi) alloys across the paramagnetic-ferromagnetic transition at 2.32% nickel concentration [103].

6.3 Visible-pump, THz-probe spectrometer

We laid a foundation for the use of THz pulses in the study of photoexcited state of insulating cuprates. In the future, the technique can be applied to a wide range of correlated electron systems. The followings are steps which can be taken to improve the spectrometer.

- The SNR of the system can be further improved by replacing the compressor gratings in the regenerative amplifier, which have become less reflective with age. Newer gratings also employ optical coatings that have improved since the manufacture of the current gratings. Overall, replacing this grating could increase the overall power by 50%.
- We can improve the temporal resolution of the spectrometer by focusing the pump and THz beams collinearly onto samples. This can be achieved by guiding the pump beam through a hole drilled in the center of the second parabolic mirror.

6.4 Undoped cuprates

We use the agreement between the visible and THz probe experiments to establish the polaronic nature of photoexcited state in $Sr_2CuO_2Cl_2$ and extend the argument to other studied compounds. Ideally, we should perform the visible-pump, visible-probe experiments on the same samples of $Sr_2CuO_2Cl_2$, $YBa_2Cu_3O_6$ and La_2CuO_4 that we used in visible-pump, THz-probe experiments. It is also valuable to measure the evolution of mobility as a function of photoexcitation wavelength using

an optical parametric amplifier (OPA), which allows us to control the photon excitation energy. This will allow us the vary the hot boson density that results from photoexcitation.

Appendix A

Derivation of Tinkham formula

Here I present a detailed derivation of the Tinkham formula for fields at normal incidence in transmission mode. We assume a thin conducting film with a thickness d_f and refractive index n_f on an insulating substrate with a refractive index n_s. The incident beam and multiple reflections from the film-substrate interface is shown in Fig. A.1. The drawing depicts an incident beam with a non-zero angle. The substrate and air are indicated by indices s and a, respectively. The total transmission

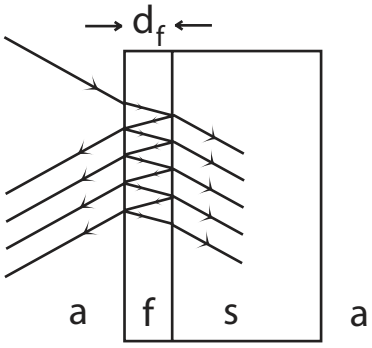

Figure A.1: Wave propagation through a thin film (f) with a thickness d_f on a substrate (s).

amplitude $\tilde{t}_f$ is an infinite summation of waves produced by multiple reflections in the thin film layer. We apply the Fresnel conditions every time the wave meets the interface. In addition, the wave picks up a phase difference $\phi = \frac{\omega}{c} d_f \tilde{n}_f$ every time it transverses the thin film medium. The total transmission amplitude is given by:

$$\tilde{t}_f = \tilde{E}_0 \, [\tilde{t}_{af}\tilde{t}_{fs}e^{i\phi} + \tilde{t}_{af}\tilde{r}_{fs}\tilde{r}_{fa}e^{2i\phi}\tilde{t}_{fs}e^{i\phi} + \tilde{t}_{af}(\tilde{r}_{fs}\tilde{r}_{fa}e^{2i\phi})^2\tilde{t}_{fs}e^{i\phi} + \tilde{t}_{af}(\tilde{r}_{fs}\tilde{r}_{fa}e^{2i\phi})^4\tilde{t}_{fs}e^{i\phi} + ...], \quad \text{(A.1)}$$

where $\tilde{t}_{ij} = (2\tilde{n}_i)/(\tilde{n}_i + \tilde{n}_j)$ is the Fresnel coefficient for transmission, $\tilde{r}_{ij} = (\tilde{n}_i - \tilde{n}_j)/(\tilde{n}_i + \tilde{n}_j)$ is the Fresnel coefficient for reflection, and $\tilde{E}_0$ is the incident electric field amplitude. Taking the limit of the geometrical series, the total transmission is written as:

$$\frac{\tilde{E}_0\, \tilde{t}_{af}\tilde{t}_{fs}e^{i\phi}}{1-\tilde{r}_{fs}\tilde{r}_{fa}e^{2i\phi}}. \tag{A.2}$$

Similarly, the transmission through a bare substrate is written as:

$$\tilde{t}_s = \tilde{E}_0\, [\tilde{t}_{as}e^{i\frac{\omega}{c}d_f\tilde{n}_s}]. \tag{A.3}$$

Assuming $\tilde{n_s} = n_s$, the complex transmittance ratio $\tilde{t}_f/\tilde{t}_s$ is given by:

$$\frac{\tilde{t}_f}{\tilde{t}_s} = \frac{\tilde{t}_{af}\tilde{t}_{fs}}{\tilde{t}_{as}}\frac{e^{i\phi}e^{i\frac{\omega}{c}d_f n_s}}{1-\tilde{r}_{fs}\tilde{r}_{fa}e^{2i\phi}}. \tag{A.4}$$

After inserting the Fresnel coefficients and some manipulation, the complex transmittance has the following form:

$$\frac{\tilde{t}_f}{\tilde{t}_s} = \frac{2\tilde{n}_f(n_a+n_s)e^{i\frac{\omega}{c}d_f n_s}}{(n_a+\tilde{n}_f)(\tilde{n}_f+n_s)e^{-i\phi}-(\tilde{n}_f-n_s)(\tilde{n}_f-n_a)e^{i\phi}}. \tag{A.5}$$

Within the long-wavelength thin film limit of $\frac{\omega}{c}d_f\tilde{n}_f \ll 1$ and $\frac{\omega}{c}d_f n_s \ll 1$,

$$\frac{\tilde{t}_f}{\tilde{t}_s} = \frac{(n_a+n_s)(1-i\frac{\omega}{c}d_f n_s)}{(n_a+n_s)-i\frac{\omega}{c}d_f(\tilde{n}_f^2+n_a n_s)}. \tag{A.6}$$

The complex index of $\tilde{n}_f$ of the film is related to the conductivity via $\tilde{n}_f^2 = \tilde{\varepsilon}_f = 1 + i\frac{\tilde{\sigma}_f}{\omega\varepsilon_0}$. Setting $n_a = 1$, the complex transmittance ratio has the following form:

$$\frac{\tilde{t}_f}{\tilde{t}_s} = \frac{(1+n_s)(1-i\frac{\omega}{c}d_f n_s)}{(1+n_s)(1-i\frac{\omega}{c}d_f)+\frac{\omega}{c}d_f\frac{\tilde{\sigma}_f}{\omega\varepsilon_0}}. \tag{A.7}$$

Assuming $1 - i\frac{\omega}{c}d_f n_s \approx 1$,

$$\frac{\tilde{t}_f}{\tilde{t}_s} = \frac{(1+n_s)}{1+n_s+Z_0 d_f\tilde{\sigma}_f}, \tag{A.8}$$

where $Z_0 = \sqrt{\frac{\varepsilon_0}{\mu_0}} = 377\Omega$ is the impedance of free space. Equation A.8 is known as the Tinkham formula.

The derivation of the Tinkham formula remains valid for a photoexcited layer induced by optical pumping on an insulating substrate. We define an effective film thickness to be the optical penetration depth or $1/e$ intensity decay length, assuming a simple exponential absorption. For transmission

through the photoexcited layer on a bare substrate, the calculation remains identical up to Eq. A.6 and I continue further by assuming a small photoinduced conductivity, $\tilde{\sigma}_f = \tilde{\sigma}_s + \Delta\tilde{\sigma}$,

$$\tilde{n}_f^2 = 1 + i\frac{\tilde{\sigma}_s}{\omega\varepsilon_0} + i\frac{\Delta\tilde{\sigma}}{\omega\varepsilon_0}. \tag{A.9}$$

After inserting Eq. A.9 into Eq. A.6 and taking the reference substrate to be the sample with no photoexcitation, the complex transmittance ratio $\tilde{t}_f/\tilde{t}_s$ will have the following form:

$$\frac{\tilde{t}_f}{\tilde{t}_s} = \frac{(1+n_s)(1-i\frac{\omega}{c}d_f n_s)}{(1+n_s)(1-i\frac{\omega}{c}d_f n_s) + \frac{\omega}{c}d_f\frac{\Delta\tilde{\sigma}}{\omega\varepsilon_0}}. \tag{A.10}$$

Assuming $1 - i\frac{\omega}{c}d_f ns \approx 1$,

$$\frac{\tilde{t}_f}{\tilde{t}_s} = \frac{(1+n_s)}{1+n_s+Z_0 d_f\Delta\tilde{\sigma}}. \tag{A.11}$$

In case of insulating compounds, there is no conduction prior to photoexcitation, and so $\Delta\tilde{\sigma} = \tilde{\sigma}_f$. For small changes in the transmission amplitude, $\Delta\tilde{t} = \tilde{t}_f - \tilde{t}_s \ll \tilde{t}_s$,

$$\tilde{\sigma}_f = -\frac{1+n_s}{Z_0 d_f}\frac{\Delta\tilde{t}}{\tilde{t}_s}. \tag{A.12}$$

From $\sigma_1(\omega = 0)$, we can calculate the free-carrier mobility μ from $\sigma = \eta n_c e\mu$, where η is the quantum efficiency for free carrier production, n_c is the excitation density, and e is the electric charge,

$$\eta\mu = -\frac{1+n_s}{Z_0 d_f n_c e}\frac{\Delta\tilde{t}}{\tilde{t}_s}. \tag{A.13}$$

Appendix B

Resistivity measurements on CrV alloys

We have applied the standard four-point technique and THz-TDS to $Cr_{1-x}V_x$ thin film samples and measured the resistivity as a function of temperature. In Chapter 3, I presented the data on the samples that we found a good agreement between the two techniques. Fig. G.1 shows the resistivity as a function of temperature for 6 more samples. In 0.9%, 1.25%, and 1.6% vanadium concentrations, THz-TDS produces the knee in the resistivity at the Néel temperature as expected, but the four-point technique do not show the feature. In 2% doped sample, we observe a good agreement between the two techniques. In 2.35% and 2.9% vanadium concentrations, there is an offset between the resistivities. The sign of the offset appears to be arbitrary and consequently, we discarded the measurements on those samples.

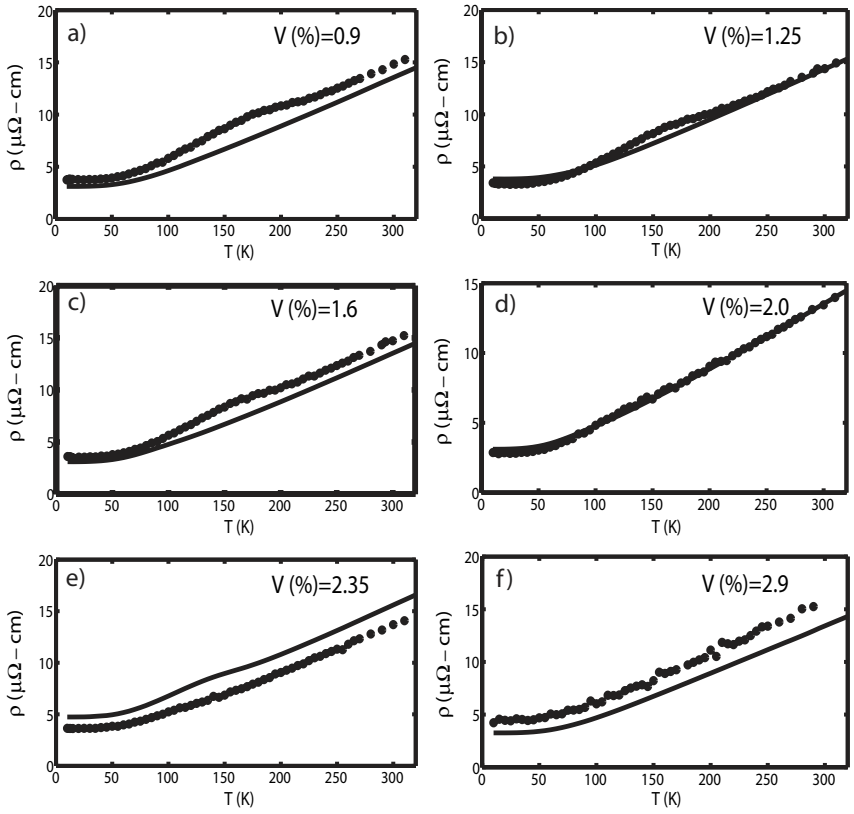

Figure B.1: Resistivity as a function of temperature for samples with a) 0.9%, b) 1.25%, c) 1.6%, d) 2.0%, e) 2.35%, and f) 2.9% vanadium concentration. Filled circles and solid curves denote the THz-TDS and standard four-point measurements, respectively.

Appendix C

Hall coefficient and anisotropic scattering lifetime

Here I use Boltzmann transport equation to evaluate the Hall coefficient for spherical Fermi surface with anisotropic scattering. In the relaxation time approximation,

$$\frac{\partial f}{\partial t} + F.\frac{\partial f}{\partial p} = -\frac{f - f^{\circ}}{\tau(p)}, \tag{C.1}$$

where $F = -e(E + v \times B)$ is the Lorentz force, $f = f(r,p)$ is the electron distribution function, and f° is the equilibrium Fermi-Dirac distribution. We assume that the applied field causes a small deviation from equilibrium distribution so as $f = f^{\circ} + \delta f$. For simplicity, we assume that $B \| p_z$ and define $\varepsilon = p^2/2m$, $\vec{v} = \vec{p}/m$, $p = \sqrt{p_x^2 + p_y^2 + p_z^2}$, $\theta = \cos^{-1}(p_z/p)$, and $\phi = \tan^{-1}(p_y/p_x)$. After performing the partial derivatives, a Fourier transform and some algebra, the linear Boltzmann equation will have the following form:

$$\left[1 - i\omega\tau(\theta,\phi) + \omega_0\tau(\theta,\phi)\frac{\partial}{\partial\phi}\right]\ \delta f = -e\vec{E}.\vec{v}\,\tau(\theta,\phi)\frac{\partial f^{\circ}}{\partial\varepsilon}, \tag{C.2}$$

where $\omega_0 = eB/m$. We study the low energy excitations and hence we drop the energy dependence of scattering lifetime. In the DC limit and zero magnetic field,

$$\delta f = -e\vec{E}.\vec{v}\,\tau(\theta,\phi)\frac{\partial f^{\circ}}{\partial\varepsilon}. \tag{C.3}$$

The electrical current density $j_x = \sigma_{xx}E_x$ is defined as:

$$j_x = -2e\int \frac{d^3p}{(2\pi\hbar)^3}\ v_x\ \delta f(p). \tag{C.4}$$

After changing the integral variable from momentum p to energy ($\varepsilon = p^2/m$),

$$\sigma_{xx} = \frac{e^2}{4\pi^3\hbar^3}\int_0^{2\pi} d\phi \int_0^{\pi} d\theta sin(\theta) \int_0^{\infty} m\sqrt{2m\varepsilon}\; v_x^2\; \tau(\theta,\phi)\left(\frac{\partial f^\circ}{\partial \varepsilon}\right). \tag{C.5}$$

At zero temperature, $\partial f^\circ/\partial\varepsilon$ peaks sharply near the Fermi level as $-\delta(\varepsilon-\varepsilon_F)$,

$$\sigma_{xx} = \frac{e^2 m\sqrt{2m\varepsilon_F}\; v_F^2}{4\pi^3\hbar^3}\int_0^{2\pi} d\phi \int_0^{\pi} d\theta \cos^2(\phi)\sin^3(\theta)\; \tau(\theta,\phi) = \alpha < \tau > . \tag{C.6}$$

In this notation, $< \tau >$ represents a weighted average over τ. Alternatively, we can write $\alpha^{-1} = \rho < \tau >= m/ne^2$, where ρ is the DC resistivity and n is the mean (unbiased) carrier density. Now we evaluate σ_{xy}, defined through the relationship $j_x = \sigma_{xy}E_y$. In the DC limit and with a weak magnetic field,

$$\partial f \simeq \left(1 - \omega_0\tau(\theta,\phi)\frac{\partial}{\partial\phi}\right)(-eE_y v_y \tau(\theta,\phi))\,(\frac{\partial f^\circ}{\partial\varepsilon}). \tag{C.7}$$

Using the definition of the current density j_x, we write σ_{xy} as:

$$\sigma_{xy} = \frac{e^2}{4\pi^3\hbar^3}\int_0^{2\pi} d\phi \int_0^{\pi} d(\theta) sin(\theta) \int_0^{\infty} d\varepsilon\; m\sqrt{2m\varepsilon}\;\delta(\varepsilon-\varepsilon_F)\; v_x\; \left(1 - \omega_0\tau(\theta,\phi)\frac{\partial}{\partial\phi}(v_y\tau(\theta,\phi)\right). \tag{C.8}$$

Using polar coordinates $v_x = v_F\sin(\theta)\cos(\phi)$ and $v_y = v_F\sin(\theta)\sin(\phi)$,

$$\sigma_{xy} = -\alpha\omega_0\left[\int_0^{2\pi} d\phi\cos(\phi)\int_0^{\pi} d\theta\sin^3(\theta)\;\tau(\theta,\phi)\frac{\partial}{\partial\phi}(\sin(\phi)\tau(\theta,\phi))\right]. \tag{C.9}$$

After performing the partial derivative, we end up with two terms,

$$\sigma_{xy} = -\alpha\omega_0[\int_0^{2\pi} d\phi\int_0^{\pi} d\theta\sin^3(\theta)\;\left[\cos(\phi)\sin(\phi)\tau(\theta,\phi)\frac{\partial}{\partial\phi}(\tau(\theta,\phi)) + \cos^2(\phi)\tau(\theta,\phi)\right]. \tag{C.10}$$

For the first symmetry allowed in a cubic crystal, $\tau(\phi) = \tau_0(1+\alpha\cos(2\phi))$, the first term is zero,

$$\sigma_{xy} = -\alpha\omega_0\left[\int_0^{2\pi} d\phi\int_0^{\pi} d\theta\sin^3(\theta)\;\cos^2(\phi)\tau(\theta,\phi)\right] = -\alpha\omega_0 < \tau^2 > . \tag{C.11}$$

The Hall coefficient R_H is defined as:

$$R_H = \frac{\sigma_{xy}}{B\;\sigma_{xx}^2} = -\frac{\omega_0}{B\alpha}\frac{< \tau^2 >}{< \tau >^2} = -\frac{1}{ne}\frac{< \tau^2 >}{< \tau >^2}. \tag{C.12}$$

The effective density of carriers n^* determined from $R_H = -(1/n^*e)$ is then given by:

$$\frac{n^*}{n} = \frac{< \tau >^2}{< \tau^2 >}. \tag{C.13}$$

Appendix D

Knife-edge technique

Here I briefly discuss the the knife-edge method used to measure the pump beam radius. The photoexcited area on the sample plays an important role in determining the photoexcitation density and photoconductivity. Moreover, the pump beam radius should be larger than that of THz probe beam, to ensure a uniformly photoexcited area for the THz probe beam.

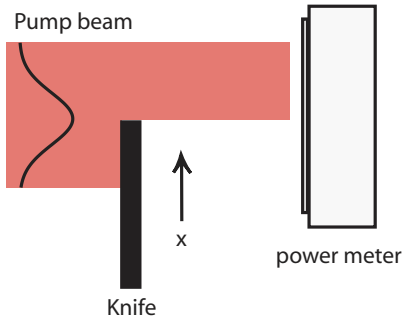

Figure D.1: Illustration of the knife-edge method.

We record the total power of the pump beam as a knife edge is translated through the beam, as shown schematically in Fig. D.1. A power meter records the integral of the Gaussian beam between $\pm\infty$ and the position of the knife edge. The radius (R) of the Gaussian beam is determined from:

$$P(R,P_0,x_0;x) = \frac{P_0}{2}\left[1 \pm \mathrm{erf}\left(\frac{\sqrt{2}(x-x_0)}{R}\right)\right], \tag{D.1}$$

where R, P_0, x_0 are free parameters determined from the fit, and the $\pm$ signs are chosen from the direction of the translated knife edge. The result of a typical horizontal knife-edge measurement is

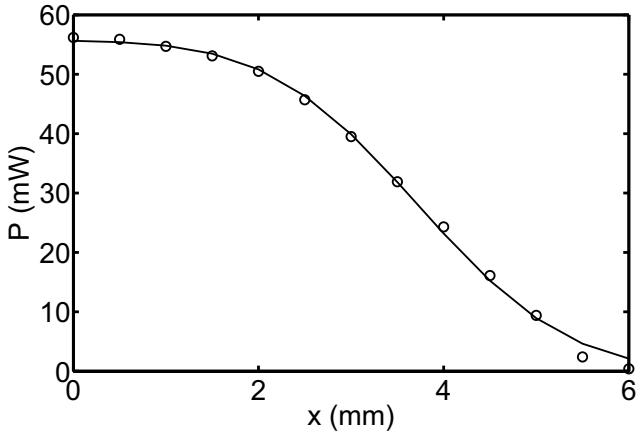

Figure D.2: Horizontal knife-edge measurement yielding a radius of 2.55 ± 0.32 mm

shown in Fig. D.2. This measurement was performed prior to the photoconductivity measurement on $Sr_2CuO_2Cl_2$. Given a constant 0.5 mW uncertainty on each point, we estimate a pump beam radius of 2.55 ± 0.32 mm.

In this particular measurement, knife edge measurements along two orthogonal directions in the focal plane confirmed the symmetric shape of the pump beam. The uncertainty in the pump beam radius implies a 12% uncertainty in the photoexcitation density.

Appendix E

Derivation of mobility from experimental quantities

Here I present the detailed derivation of mobility from the experimentally measured values. We measure the average pump power with a power meter. The pump beam radius is measured using a knife edge technique as described in Appendix D. From the central wavelength of amplifier laser, we estimate the photon energy. We define an effective film thickness to be the optical penetration depth or $1/e$ intensity decay length, assuming a simple exponential absorption. The photoexcitation density is given by:

$$n_{\text{ex}} = \frac{P_p}{\varepsilon_\gamma \pi r^2 d_f} \tag{E.1}$$

where P_p is the pump power per pulse, ε_γ is the photon energy, r is the pump beam radius, and d_f is the penetration depth. In SCOC, we measured a pump power of 50 mW and pump beam radius of 2.55 mm. For our 1 kHz amplifier laser, we estimate a flux of 2.5 W/m^2 per pulse. For 3.1 eV photons, we use an effective thickness of $d_f = 80$ nm [96]. Using Eqn. E.1, we estimate a photoexcitation density of $n_{\text{ex}} = 6.2 \times 10^{19}$ cm^{-3}. For lattice constants of $a = 3.97$ $\mathring{A}$, $b = 3.97$ $\mathring{A}$, and $c = 15.61$ $\mathring{A}$ in SCOC, this is equivalent to 1.5%, or 0.015 photoexcitations per unit cell.

For small pump-induced change in the transmitted THz amplitude ($\Delta\tilde{E}/\tilde{E} \ll 1$) , the conductivity can be calculated from:

$$\tilde{\sigma} = -\frac{1+n_s}{Z_0 d_f}\frac{\Delta\tilde{E}}{\tilde{E}}. \tag{E.2}$$

where Z_0 the impedance of free space, and n_s the refractive index of the unexcited samples in THz region and . In SCOC, we estimate a DC conductivity of 3.3 $(\Omega - \mathrm{cm})^{-1}$ at 1.3 ps after photoexcitation. From $\sigma_1(0)$ we can calculate the free-carrier mobility μ implied by $\sigma = \eta q_e(n_e\mu_e + n_h\mu_h)$, where η is the quantum efficiency for producing free carriers per photon, and q_e is the electron charge. Note that each incident photon creates an electron-hole pair and thus, $n_{\mathrm{ex}} = n_e = n_h$. We assume that $\mu_e \approx \mu_h \equiv \mu$ for photoexcited electrons because of their similar mobility in the lightly electron-doped cuprates [94, 57]. Therefore,

$$\sigma \backsimeq 2\eta\mu q_e n_{\mathrm{ex}}. \tag{E.3}$$

Since the quantum efficiency for the creation of unbound excitations is not known, our measurement gives the product of mobility and quantum efficiency $\eta\mu$. In SCOC, 1.3 ps after photoexcitation, the extrapolated DC conductivity corresponds to charge transport with a mobility of 0.15 ± 0.05 cm^2/V.s, where the dominant uncertainty is the variation from sample to sample.

Appendix F

Imaginary part of photoconductivity

The visibile-pump, THz-probe technique provides a simultaneous measurement of real and imaginary part of conductivity. Fig. F.1 shows the comparison between the real and imaginary part of the

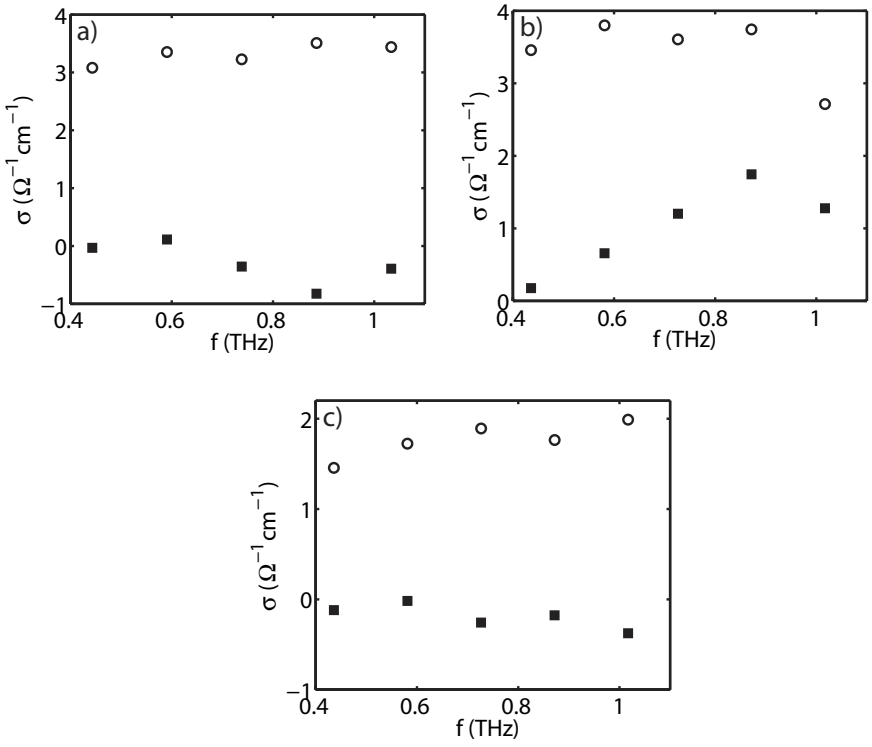

Figure F.1: Real (○) and imaginary (□) part of conductivity at 1.3 ps after photoexcitation in a) SCOC b) YBCo c) LCO.

conductivity at 1.3 ps after photoexcitation in the undoped cuprates SCOC, YBCO, and LCO. The imaginary part in SCOC and LCO do not show any significant dispersion and the values are zero within ± 0.9 $(\Omega\,\mathrm{cm})^{-1}$. In YBCO at 1.3 ps after photoexcitation, the imaginary part increases with increasing frequency that we attribute to the experimental artifacts. At later times after photoexcitation, the imaginary part shows less frequency dependence.

Appendix G

Resistivity measurements on CrV alloys

We have applied the Standard four-point technique and THz-TDS to $Cr_{1-x}V_x$ thin film samples and measured the resistivity as a function of temperature. In Chapter 4, I chose the samples that we found a good agreement between the two techniques. Fig. G.1shows the resistivity as a fubction of temperature for 6 more samples. For 0.9%, 1.25%, and 1.6% vanadium concentrations, THz-TDS produces the knee in the resistivity at the Neel temperature as expected, but the four-point technique do not show the feature. In 2% doped sample, we observe a good agreement between the two techniques. For 2.35% and 2.9% vanadium concentrations, there is an offset between the resistivities. The sign of the offset appears to be arbitrary and we discarded the measurements on those samples.

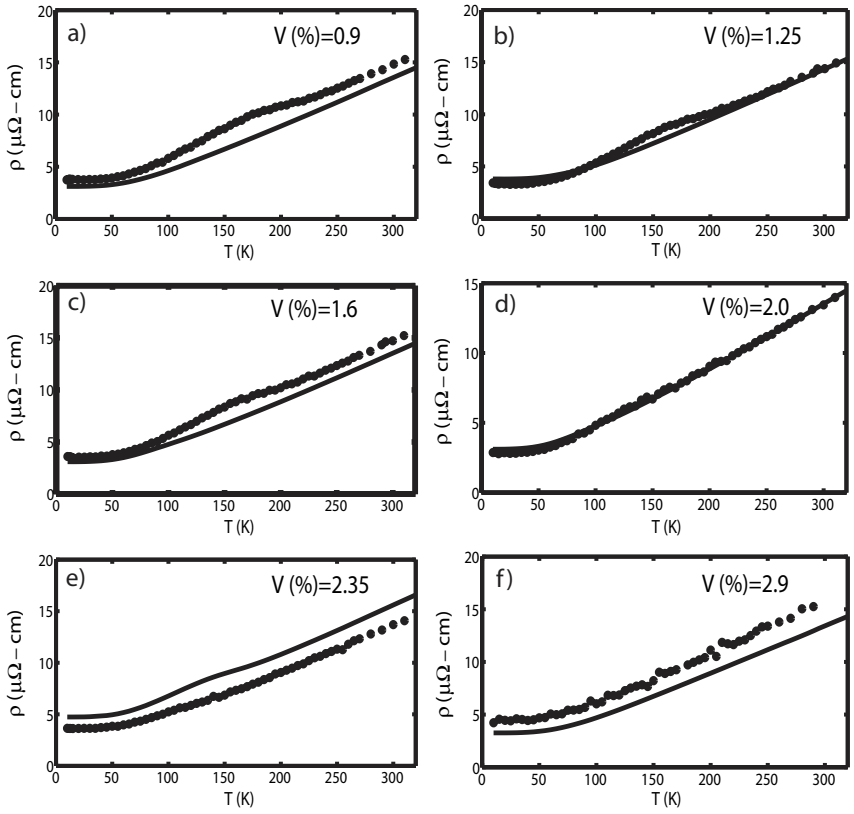

Figure G.1: Resistivity as a function of temperature for samples with a) 0.9%, b) 1.25%, c) 1.6%, d) 2.0%, e)2.35%, and f) 2.9% vanadium concentration. Filled circles and solid curves denote the THz-TDS and standard four-point measurements, respectively.

Bibliography

[1] D. H. Auston, K. P. Cheung, and P. R. Smith. Picosecond photoconductive Hertzian dipoles. *Appl. Phys. Lett.*, 45:284, 1984.

[2] Q. Wu and X.-C. Zhang. Ultrafast electro-optic field sensors. *Appl. Phys. Lett.*, 68:1604, 1996.

[3] M. van Exter and D. Grischkowsky. Carrier dynamics of electrons and holes in moderately doped silicon. *Phys. Rev. B*, 41:12140, 1990.

[4] M. C. Nuss, P. M. Mankiewich, M. L. O'Malley, E. H. Westerwick, and P. B. Littlewood. Dynamic conductivity and coherence peak in $YBa_2Cu_3O_7$ superconductors. *Phys. Rev. Lett.*, 66:3305, 1991.

[5] W. Greiner. *Classical Electrodynamics*. Springer, 1st edition, 1998.

[6] Lionel Duvillaret, Frédéric Garet, Jean-Franois Roux, and Jean-Louis Coutaz. Analytical modeling and optimization of terahertz time-domain spectroscopy experiments using photoswitches as antennas. *IEEE, J. Sel. Top. Quantum Electron*, 7:615, 2001.

[7] F. E. Doany, D. Grischkowsky, and C.-C. Chi. Carrier lifetime versus ion-implantation dose in silicon on sapphire. *Appl. Phys. Lett.*, 50:460, 1986.

[8] K. P . H. Lui and F.A. Hegmann. Ultrafast carrier relaxation in radiation-damaged silicon on sapphire studied by optical-pump–terahertz-probe experiments. *Appl. Phys. Lett.*, 78:3478, 2001.

[9] D. Grischkowsky, S. Keiding, M. Exter, and Ch. Fattinger. Far-infrared time-domain spectroscopy with terahertz beams of dielectrics and semiconductors. *J. Opt. Soc. Am. B*, 7:2006, 1990.

[10] X. Xin, H. Altan, A. Saint, D. Matten, and R. R. Alfano. Terahertz absorption spectrum of *para* and *ortho* water vapors at different humidities at room temperature. *J. Appl. Phys.*, 100:094905, 2006.

[11] Carl-Philippe Kübler. Creation and characterization of a terahertz time-domain spectrometer. Master's thesis, Simon Fraser University, 2002.

[12] A. E. Siegman. *Lasers*. University Science Books, 1986.

[13] M. Tinkham. Energy gap interpretation of experiments on infrared transmission through superconducting films. *Phys. Rev.*, 104:845, 1956.

[14] M. A. Gilmore, S. Kamal, D. M. Broun, and J. S. Dodge. Determination of electron-phonon interaction parameters from time-domain terahetz spectroscopy. *Appl. Phys. Lett.*, 88:141910, 2006.

[15] J. Schoukens, R. Pintelon, and J. Renneboog. A maximum likelihood estimator for linear and nonlinear systems — a practical application of estimation techniques in measurement problems. *IEEE Trans. Instrum. Meas.*, 37:10, 1988.

[16] R. J. Barlow. *A Guide to the use of statistical methods in the physical sciences*. Wiley, Chichester, 1989.

[17] N.W. Ashcroft and N.D. Mermin. *Solid State Physics*. Holt, Rinehart and Winston, New York, 1976.

[18] G. E. P. Box, G. M. Jenkins, and G. C. Reinsel. *Time Series Analysis: Forecasting and Control*. Prentice Hall, Englewood Cliffs,, 3rd edition, 1994.

[19] E. Fawcett, H. V. Alberts, V. Yu. Galkin, D. R. Noakes, and J. V. Yakhmi. Spin-density wave antiferromagnetism in chromium alloys. *Rev. Mod. Phys.*, 66:25, 1994.

[20] Clarina de la Cruz *et al.* Magnetic order close to superconductivity in the iron-based layered $LaO_{1-x}F_xFeAs$ systems. *Nature (London)*, 453:899, 2008.

[21] M. Rotter, M. Tegel, D. Johrendt, I. Schellenberg, W. Hermes, and R. Pöttgen. Spin-density-wave anomaly at 140 K in the ternary iron arsenide $BaFe_2As_2$. *Phys. Rev. B*, 78:020503, 2008.

[22] A. S. Sefat, R. Jin, M. A. McGuire, B. C. Sales, D. J. Singh, and David Mandrus. Superconductivity at 22 K in Co-doped $BaFe_2As_2$ crystals. *Phys. Rev. Lett.*, 101:117004, 2008.

[23] A. Yeh, Yeong-Ah Soh, J. Brooke, G. Aeppli, T. F. Rosenbaum, and S. M. Hayden. Quantum phase transition in a common metal. *Nature*, 419:459, 2002.

[24] M. Lee, A. Husmann, T. F. Rosenbaum, and G. Aeppli. High resolution study of magnetic ordering at absolute zero. *Phys. Rev. Lett.*, 92:187201, 2004.

[25] M. R. Norman, Qimiao Si, Ya. B. Bazaliy, and R. Ramazashvili. Hall effect in nested antiferromagnets near the quantum critical point. *Phys. Rev. Lett.*, 90:116601, 2003.

[26] Ravi K. Kummamuru and Yeong-Ah Soh. Electrical effects of spin density wave quantization and magnetic domain walls in chromium. *Nature*, 452:859, 2008.

[27] C. G. Shull and M. K. Wilkinson. Neutron diffraction studies of various transition elements. *Rev. Mod. Phys.*, 25:100, 1953.

[28] Chih Lu and Alvin A. Milgram. Effect of stress on the Hall coefficient of chromium films. *J. Appl. Phys.*, 38:2038, 1967.

[29] Bykov, V. N., V. S. Golovkin, N. V. Ageev, V. A. Levdik, and S. I. Vinogradov. Neutron diffraction study in CrV dilute alloys. *Dokl. Akad. Nauk SSSR.*, 128:1153, 1959.

[30] L. Corliss, N. Elliott, and J. Hastings. Magnetic structures of the polymorphic forms of manganous sulfide. *Phys. Rev.*, 104:924, 1959.

[31] G. Shirane and W. J. Takei. Neutron diffraction study on chromium alloy with small amounts of vanadium. *J. Phys. Soc. Jpn.*, 111:35, 1962.

[32] W. M. Lomer. Electronic structure of chromium group metals. *Proc. Phys. Soc. London*, 80:489, 1962.

[33] J. E. Graebner and J. A. Marcus. de Haas-van Alphen effect in antiferromagnetic chromium. *Phys. Rev.*, 175:659, 1968.

[34] A. W. Overhauser. Spin density waves in an electron gas. *Phys. Rev.*, 128:1437, 1962.

[35] A. S. Barker, B. I. Halperin, and T. M. Rice. Antiferromagnetic energy gap in chromium. *Phys. Rev. Lett.*, 20:384, 1968.

[36] J. Schäfer, Eli Rotenberg, G. Meigs, and S. D. Kevan. Direct spectroscopic observation of the energy gap formation in the spin density wave phase transition at the Cr(110) surface. *Phys. Rev. Lett.*, 83:2069, 1999.

[37] S. Kagoshima, H. Nagasawa, and T. Sambogi. *One-dimensional conductors*. Springer-Verlag, New York, 4th edition, 1988.

[38] Y. Furuya. Temperature dependance and magnetic dependance of the Hall coefficient on the antiferromagnetic chromium. *J. Phys. Soc. Jpn.*, 40:490, 1976.

[39] W. C. Koehler, R. M. Moon, A. L. Trego, and A. R. Mackintosh. Antiferromagnetism in chromium alloys (neutron diffraction). *Phys. Rev.*, 151, 1966.

[40] J. Takeuchi, H. Sasakura, and Y. Masuda. Spin fluctuation in itinerant electron antiferromagnetic CrV system. *J. Phys. Soc. Jpn.*, 49:508, 1980.

[41] J. M. Ziman. *Electrons and phonons*. Oxford Univ. Press, Oxford, England, 1st edition, 1960.

[42] Ravi K. Soh Kummamuru and Yeong-Ah. Electrical effects of spin density wave quantization and magnetic domain walls in chromium. *Nature*, 452:859, 2008.

[43] J. F. DiTusa, R. G. Goodrich, N. Harrison, and E. S. Choi. Fermi surface of $Cr_{1-x}V_x$ across the quantum critical point. *Phys. Rev. B*, 82:075114, 2010.

[44] J. M. Ziman. Approximate calculation of the anisotropy of the relaxation time of the conduction electrons in the noble metals. *Phys. Rev.*, 121:1320, 1961.

[45] P. N. Trofimenkoff. Anisotropy of electron-phonon Umklapp scattering and the Hall coefficient. *J. Low-Temp. Phys.*, 16:455, 1974.

[46] S. M. Hayden, R. Doubble, G. Aeppli, T. G. Perring, and E. Fawcett. The strongly enhanced magnetic excitations near the quantum critical point of $Cr_{1-x}V_x$ and why strong exchange enhancement need not imply heavy fermion behavior. *Phys. Rev. Lett.*, 84:999, 2000.

[47] G. Vaillancourt, T. B. Norris, J. S. Coe, P. Bado, and G. A. Mourou. Operation of a 1-kHz pulse-pumped Ti:sapphire regenerative amplifier. *Optics Letters*, 15:317, 1990.

[48] R. Boyd. *Nonlinear Optics*. Academic Press, San Diego, 2nd edition, 2003.

[49] I. Wilke and S. Sengupta. Nonlinear optical techniques for terahertz pulse generation and detection—optical rectification and electrooptic sampling. In S. L. Dexheimer, editor, *Terahertz Spectroscopy: Principles and Applications*. CRC Press, Boca Raton, FL, 2008.

[50] A. Nahata, A. S. Weling, and T. F. Heinz. A wideband coherent terahertz spectroscopy system using optical rectification and electro-optic sampling. *Appl. Phys. Lett.*, 69:2321, 1996.

[51] M. C. Beard, G. M. Turner, and C. A. Schmuttenmaer. Transient photoconductivity in GaAs as measured by time-resolved terahertz spectroscopy. *Phys. Rev. B*, 62:15674, 2000.

[52] J. I. Pankove. *Optical Processes in Semiconductors*. Prentice-Hall, Englewood, NJ, New York, 1971.

[53] H. C. Casey, D. D. Sell, and K. W. Wecht. Concentration dependence of the absorption coefficient for n- and p-type gaas between 1.3 and 1.6 eV. *J. Appl. Phys.*, 46:250, 2009.

[54] D. L. Rode. Electron mobility in direct gap polar semiconductors. In R. K. Willardson and A. C. Beer., editors, *Semiconductors and Semimetals*, volume 10, Transport phenomena. Academic Press, NY, New York, 1975.

[55] P. A. Lee, N. Nagaosa, and Xiao-Gang Wen. Doping a Mott insulator: Physics of high temperature superconductivity. *Rev. Mod. Phys.*, 78:17, 2006.

[56] T. Thio, R. J. Birgeneau, A. Cassanho, and M. A. Kastner. Determination of the energy gap for charged excitations in insulating La_2CuO_4. *Phys. Rev. B*, 42:10800, 1990.

[57] Y. Ando, A. N. Lavrov, S. Komiya, K. Segawa, and X. F. Sun. Mobility of the doped holes and the antiferromagnetic correlations in underdoped high-T_c cuprates. *Phys. Rev. Lett.*, 87:017001, 2001.

[58] J. S. Dodge *et al.* Optically induced softening of the charge-transfer gap in $Sr_2CuO_2Cl_2$. *ArXiv., 0910.5048*, 2009.

[59] H. K. Onnes. Further experiments with liquid helium G. On the electrical resistance of pure metals etc. VI. On the sudden change in the rate at which the resistance of mercury disappears. *Comm. Phys. Lab. Univ. Leiden*, 124c, 1911.

[60] J. Bardeen, L. N. Cooper, and J. R. Schrieffer. Theory of superconductivity. *Phys. Rev.*, 108:1175, 1957.

[61] J. G. Bednorz and K. A. Müller. Possible high-T_c superconductivity in the Ba-La-Cu-O system. *Z. Physik. B*, 64:189, 1986.

[62] M. K. Wu, J. R. Ashburn, C. J. Torng, P. H. Hor, R. L. Meng, L. Gao, Z. J. Huang, Y. Q. Wang, and C. W. Chu. Superconductivity at 93 K in a new mixed-phase Y-Ba-Cu-O compound system at ambient pressure. *Phys. Rev. Lett.*, 58:908, 1987.

[63] G. F. Sun, K. W. Wong, B. R. Xu, Y. Xin, and D. F. Lu. T_c enhancement of $HgBa_2Ca_2Cu_3O_{8+\delta}$ by Tl substitution. *Phys. Rev. B*, 192:122, 1994.

[64] T. Timusk and B. Statt. The pseudogap in high-temperature superconductors: an experimental survey. *Rep. Prog. Phys.*, 62:61, 1999.

[65] A. Alff. A hidden pseudogap under the dome of superconductivity in electron-doped high-temperature superconductors. *Nature*, 422:698, 2003.

[66] Mark S. Hybertsen, Michael Schlüter, and Niels E. Christensen. Calculation of coulomb-interaction parameters for La_2CuO_4 using a constrained-density-functional approach. *Phys. Rev. B.*, 39:9028, 1989.

[67] G. Blumberg, P. Abbamonte, M. V. Klein, W. C. Lee, D. M. Ginsberg, L. L. Miller, and A. Zibold. Resonant two-magnon Raman scattering in cuprate antiferromagnetic insulators. *Phys. Rev. B*, 53:R11930, 1996.

[68] Y. Tokura, S. Koshihara, T. Arima, H. Takagi, S. Ishibashi, T. Ido, and S. Uchida. Cu-O network dependence of optical charge-tranfer gaps and spin pair excitations in single-CuO_2-layer compunds. *Phys. Rev. B*, 41:11657, 1990.

[69] N. Nücker, J. Fink, J. C. Fuggle, P. J. Durham, and W. M. Temmerman. Evidence for holes on oxygen sites in the high-T_c superconductors $La_{2-x}Sr_xCuO_4$ and $YBa_2Cu_3O_{7-y}$. *Phys. Rev. B*, 37:5158, 1988.

[70] H. S. Choi, Y. S. Lee, T. W. Noh, E. J. Choi, Y. Bang, and Y. J. Kim. Anomalous temperature dependence of charge-transfer excitation in the undoped cuprate $Sr_2CuO_2Cl_2$. *Phys. Rev. B*, 60:4646, 1999.

[71] F. C. Zhang and T. M. Rice. Effective Hamiltonian for the superconducting copper oxides. *Phys. Rev. B*, 37:3759, 1988.

[72] A. Lanzara *et al.* Evidence for ubiquitous strong electron-phonon coupling in high-temperature superconductors. *Nature*, 412:510, 2001.

[73] B. O. Wells, Z. X. Shen, A. Matsuura, D. M. King, M. A. Kastner, M. Greven, and R. J. Birgeneau. E versus k relations and many body effects in the model insulating copper oxide $Sr_2CuO_2Cl_2$. *Phys. Rev. Lett.*, 74:964, 1995.

[74] K. M. Shen *et al.* Angle-resolved photoemission studies of lattice polaron formation in the cuprate $Ca_2CuO_2Cl_2$. *Phys. Rev. B*, 75:075115, 2007.

[75] C. Y. Chen, R. J. Birgeneau, M. A. Kastner, N. W. Preyer, and T. Thio. Frequency and magnetic-field dependence of the dielectric constant and conductivity of La_2CuO_{4+y}. *Phys. Rev. B*, 43:392, 1991.

[76] C. Y. Chen, N. W. Preyer, P. J. Picone, M. A. Kastner, H. P. Jenssen, D. R. Gabbe, A. Cassanho, and R. J. Birgeneau. Frequency dependence of the conductivity and dielectric constant of La_2CuO_{4+y} near the insulator-metal transition. *Phys. Rev. Lett.*, 63:2307, 1989.

[77] J. Shah. *Ultrafast spectroscopy of semiconductors and semiconductor nanostructures*, volume 115 of *Springer Series in Solid State Sciences*. Springer, New York, 2nd edition, 1999.

[78] M. A. Kastner *et al.* Resistivity of nonmetallic $La_{2-y}Sr_yCu_{1-x}Li_xO_{4-\delta}$ single crystals and ceramics. *Phys. Rev. B*, 37:111, 1988.

[79] W. J. Padilla, Y. S. Lee, , M. Dumm, S. Ono, K. Segawa, S. Komiya, Y. Ando, and D. N. Basov. Constant effective mass across the phase diagram of high-T_c cuprates. *Phys. Rev. B*, 72:060511, 2005.

[80] J. P. Falck, A. Levy, M. A. Kastner, and R. J. Birgeneau. Charge-transfer spectrum and its temperature dependence in La_2CuO_4. *Phys. Rev. Lett.*, 69:1109, 1992.

[81] J. Orenstein and A. J. Millis. Advances in the physics of high-temperature superconductivity. *Science*, 288:468, 2000.

[82] E. Hendry, F. Wang, J. Shan, T. F. Heinz, and M. Bonn. Electron transport in TiO_2 probed by THz time-domain spectroscopy. *Phys. Rev. B*, 69:081101, 2004.

[83] K. B. Lyons, P. A. Fleury, J. P. Remeika, A. S. Cooper, and T. J. Negran. Dynamics of spin fluctuations in lanthanum cuprate. *Phys. Rev. B*, 37:2353, 1988.

[84] R. J. Birgeneau, M. Greven, M. A. Kastner, Y. S. Lee, B. O. Wells, Y. Endoh, K. Yamada, and G. Shirane. Instantaneous spin correlations in La_2CuO_4. *Phys. Rev. B*, 59:13788, 1999.

[85] M. Suzuki. Hall coefficients and optical properties of La_2CuO_4 single-crystal thin films. *Phys. Rev. B*, 39:2312, 1989.

[86] L. L. Miller, X. L. Wang, S. X. Wang, C. Stassis, D. C. Johnston, J. Faber, and C.-K. Loong. Synthesis, structure and properties of $Sr_2CuO_2Cl_2$. *Phys. Rev. B*, 41:1921, 1990.

[87] H. Yang, Q. Q. Liu, R. C. Yu, F. Y. Li, and C. Q. Jin. New superconducting phase of $Sr_2CuO_{2+\delta}Cl_{2-y}$ with 0201-type structure synthesized under high pressure. *Supercond. Sci. Technol.*, 18:813, 2005.

[88] Z. Hiroi, N. Kobayashi, and M. Takano. Probable hole-doped superconductivity without apical oxygens in $(Ca, Na)_2CuO_2Cl_2$. *Nature*, 371:139, 1994.

[89] Hk. Müller-Buschbaum. On the crystal chemistry of oxomercurates (II). *Angew. Chem.*, 89:704, 1977.

[90] Ch. Niedermayer, C. Bernhard, T. Blasius, A. Golnik, A. Moodenbaugh, and J. I. Budnick. Common phase diagram for antiferromagnetism in $La_{2-x}Sr_xCuO_4$ and $Y_{1-x}Ca_xBa_2Cu_3O_6$ as seen by muon spin rotation. *Phys. Rev. Lett.*, 80:3483, 1998.

[91] J. Zaanen, A. T. Paxton, O. Jepsen, and O. K. Andersen. Chain-fragment doping and the phase diagram of $YBa_2Cu_3O_{7-x}$. *Phys. Rev. Lett.*, 60:2685, 1988.

[92] D. C. Peets, Ruixing Liang, C. Stock, W. J. L. Buyers, Z. Tun, L. Taillefer, R. J. Birgeneau, D. A. Bonn, and W. N. Hardy. Top-seeded melt-growth of $YBa_2Cu_3O_x$ crystals for neutron diffraction studies. *J. Superconductivity*, 531:2312, 2002.

[93] A. J. Millis. Optical conductivity and correlated electron physics. In D. Baeriswyl and L. Degiorgi, editors, *Strong interactions in low dimensions*. Kluwer, Netherlands, 2004.

[94] X. F. Sun, Y. Kurita, T. Suzuki, Seiki Komiya, and Yoichi Ando. Thermal conductivity of $Pe_{1.3-x}La_{0.7}Ce_xCuO_4$ single crystals and signitures of stripes in an electron-doped cuprates. *Phys. Rev. Lett.*, 92:047001, 2004.

[95] T. Holstein. Studies of polaron motion. *Ann. Phys. (N.Y)*, 8:325, 1959.

[96] A. Zibold, H. L. Liu, S. W. Moore, J. M. Graybeal, and D. B. Tanner. Optical properties of single-crystal $Sr_2CuO_2Cl_2$. *Phys. Rev. B*, 53:11734, 1996.

[97] H. J. Ye, R. P. McCall, W. E. Farneth, E. M. McCarron, and A. J. Epstein. Infrared-absorption and photoinduced-absorption spectroscopy of semiconducting $YBa_2Cu_3O_{6+x}$ (A=16 and 18; $0 \leq x \leq 0.3$). *Phys. Rev. B*, 43:10574, 1991.

[98] B. Ellman, H. M. Jaeger, D. P. Katz, T. F. Rosenbaum, A. S. Cooper, and G. P. Espinosa. Transport studies of $La_{2-x}Sr_xCuO_4$ near the insulator-metal-superconductor transition. *Phys. Rev. B*, 39:9012, 1988.

[99] T. Yoshida *et al.* Metallic behavior of lightly doped $La_{2-x}Sr_xCuO_4$ with a Fermi surface forming an arc. *Phys. Rev. Lett.*, 91:027001, 2003.

[100] D. S. Ellis, J. P. Hill, S. Wakimoto, R. J. Birgeneau, D. Casa, T. Gog, and Young-June Kim. Charge-transfer exciton in La_2CuO_4 probed with resonant inelastic x-ray scattering. *Phys. Rev. B*, 77:060501, 2008.

[101] Y. Y. Wang, F. C. Zhang, V. P. Dravid, K. K. Ng, M. V. Klein, S. E. Schnatterly, and L. L. Miller. Momentum-dependent charge transfer excitations in $Sr_2CuO_2Cl_2$ angle-resolved electron energy loss spectroscopy. *Phys. Rev. Lett.*, 77:1809, 1996.

[102] Graham Lea. Metallic scattering lifetime measurement with terahertz time-domain spectroscopy. Master's thesis, Simon Fraser University, 2010.

[103] A. Tari and B. R. Coles. Electrical resistivity and the transition to ferromagnetism in the palladium-nickel alloys. *J. Phys. F: Met. Phys.*, 1:69, 1971.